

Economical Concrete Mix Design Utilizing Blended Cements, Performance-Based Specifications, and Pay Factors

Final Report 633
May 2013



Arizona Department of Transportation
Research Center

Economical Concrete Mix Design Utilizing Blended Cements, Performance-Based Specifications, and Pay Factors

**Final Report 633
May 2013**

Prepared by:

Mehdi Bakhshi, Graduate Research Associate
Busaba Laungrungrong, Graduate Research Associate
Aboozar Bonakdar, Postdoctoral Research Associate
Barzin Mobasher, Professor
Connie M. Borrer, Professor, Math & Natural Sciences Division
Douglas C. Montgomery, Professor
Ira A. Fulton Schools of Engineering
Arizona State University
Tempe, AZ 85287-5306

Prepared for:

Arizona Department of Transportation
206 South 17th Avenue
Phoenix, AZ 85007
in cooperation with
U.S. Department of Transportation
Federal Highway Administration

This report was funded in part through grants from the Federal Highway Administration, U.S. Department of Transportation. The contents of this report reflect the views of the authors, who are responsible for the facts and the accuracy of the data, and for the use or adaptation of previously published material, presented herein. The contents do not necessarily reflect the official views or policies of the Arizona Department of Transportation or the Federal Highway Administration, U.S. Department of Transportation. This report does not constitute a standard, specification, or regulation. Trade or manufacturers' names that may appear herein are cited only because they are considered essential to the objectives of the report. The U.S. government and the State of Arizona do not endorse products or manufacturers.

Technical Report Documentation Page

1. Report No. FHWA-AZ-13-633		2. Government Accession No.		3. Recipient's Catalog No.	
4. Title and Subtitle Economical Concrete Mix Design Utilizing Blended Cements, Performance-Based Specifications, and Pay Factors				5. Report Date May 2013	
7. Author(s) M. Bakhshi, B. Laungrungrong, A. Bonakdar, B. Mobasher, C.M. Borrer, and D.C. Montgomery				6. Performing Organization Code	
9. Performing Organization Name and Address Ira A. Fulton Schools of Engineering Arizona State University Tempe, AZ 85287-5306				8. Performing Organization Report No.	
12. Sponsoring Agency Name and Address Research Center Arizona Department of Transportation 206 S. 17th Ave. MD075R Phoenix, AZ 85007				10. Work Unit No. (TRAVIS)	
				11. Contract or Grant No. SPR-PL1 (181) 633	
13. Type of Report and Period Covered Final Report				14. Sponsoring Agency Code	
15. Supplementary Notes Prepared in cooperation with the U.S. Department of Transportation, Federal Highway Administration					
16. Abstract <p>This report showcases several new approaches of using materials science and structural mechanics to accomplish sustainable design of concrete materials. The topics addressed include blended cements, fiber-reinforced concrete (FRC), internal curing with lightweight aggregate, and statistical process control (SPC). Materials, methodologies, and test methods to enhance the performance and durability of concrete are addressed. Properties of pozzolans, blended cements, fly ashes, and other materials, along with proposed categories of high-performance concrete (HPC) mixtures using high-volume fly ash are briefly described. Early-age cracking and drying shrinkage are addressed in detail, as they both reduce load-carrying capacity and accelerate deterioration, resulting in increased maintenance costs and reduced service life. New developments in HPC materials using FRC are proposed, and it is shown that considerable cost savings can be realized by using fiber concrete mixtures.</p> <p>Internal curing techniques as a means of improving the quality of concrete using pre-soaked lightweight aggregate as an internal water supply were studied. The superior results of internally cured samples with lightweight aggregates, especially sintered bottom ash, indicate a great potential for using them in hot-weather concreting or when external curing is not possible.</p> <p>A new method for statistical data processing of concrete strength data also is presented. Technical tools were developed to improve performance-based specifications and statistical process control methods using cumulative sum (CUSUM) and exponentially weighted moving average (EWMA). Both of these approaches allow for process control and quality control (QC) monitoring of the materials. This report concludes with specifications for quality assurance (QA) and introduces quality measures as criteria for reducing the costs.</p>					
17. Key Words Fiber-reinforced concrete, FRC, performance-based specifications			18. Distribution Statement No restrictions. This document is available to the public through the National Technical Information Service, Springfield, VA 22161.		
19. Security Classification (of this report) Unclassified		20. Security Classification (of this page) Unclassified		21. No. of Pages 123	22. Price

SI* (MODERN METRIC) CONVERSION FACTORS

APPROXIMATE CONVERSIONS TO SI UNITS

Symbol	When You Know	Multiply By	To Find	Symbol
LENGTH				
in	inches	25.4	millimeters	mm
ft	feet	0.305	meters	m
yd	yards	0.914	meters	m
mi	miles	1.61	kilometers	km
AREA				
in ²	square inches	645.2	square millimeters	mm ²
ft ²	square feet	0.093	square meters	m ²
yd ²	square yard	0.836	square meters	m ²
ac	acres	0.405	hectares	ha
mi ²	square miles	2.59	square kilometers	km ²
VOLUME				
fl oz	fluid ounces	29.57	milliliters	mL
gal	gallons	3.785	liters	L
ft ³	cubic feet	0.028	cubic meters	m ³
yd ³	cubic yards	0.765	cubic meters	m ³
NOTE: volumes greater than 1000 L shall be shown in m ³				
MASS				
oz	ounces	28.35	grams	g
lb	pounds	0.454	kilograms	kg
T	short tons (2000 lb)	0.907	megagrams (or "metric ton")	Mg (or "t")
TEMPERATURE (exact degrees)				
°F	Fahrenheit	5 (F-32)/9 or (F-32)/1.8	Celsius	°C
ILLUMINATION				
fc	foot-candles	10.76	lux	lx
fl	foot-Lamberts	3.426	candela/m ²	cd/m ²
FORCE and PRESSURE or STRESS				
lbf	poundforce	4.45	newtons	N
lbf/in ²	poundforce per square inch	6.89	kilopascals	kPa

APPROXIMATE CONVERSIONS FROM SI UNITS

Symbol	When You Know	Multiply By	To Find	Symbol
LENGTH				
mm	millimeters	0.039	inches	in
m	meters	3.28	feet	ft
m	meters	1.09	yards	yd
km	kilometers	0.621	miles	mi
AREA				
mm ²	square millimeters	0.0016	square inches	in ²
m ²	square meters	10.764	square feet	ft ²
m ²	square meters	1.195	square yards	yd ²
ha	hectares	2.47	acres	ac
km ²	square kilometers	0.386	square miles	mi ²
VOLUME				
mL	milliliters	0.034	fluid ounces	fl oz
L	liters	0.264	gallons	gal
m ³	cubic meters	35.314	cubic feet	ft ³
m ³	cubic meters	1.307	cubic yards	yd ³
MASS				
g	grams	0.035	ounces	oz
kg	kilograms	2.202	pounds	lb
Mg (or "t")	megagrams (or "metric ton")	1.103	short tons (2000 lb)	T
TEMPERATURE (exact degrees)				
°C	Celsius	1.8C+32	Fahrenheit	°F
ILLUMINATION				
lx	lux	0.0929	foot-candles	fc
cd/m ²	candela/m ²	0.2919	foot-Lamberts	fl
FORCE and PRESSURE or STRESS				
N	newtons	0.225	poundforce	lbf
kPa	kilopascals	0.145	poundforce per square inch	lbf/in ²

*SI is the symbol for the International System of Units. Appropriate rounding should be made to comply with Section 4 of ASTM E380.
(Revised March 2003)

TABLE OF CONTENTS

Chapter 1. Introduction	1
Chapter 2. Concrete Materials for a Sustainable Infrastructure.....	3
A Case for Sustainable Infrastructure Systems	3
Blended Cements.....	3
High-performance Concrete	7
Chapter 3. Fiber-reinforced Concrete	15
Introduction	15
Fiber Types.....	17
Three-Point Bending Tests.....	17
Experimental Results of Three-point Bending Test.....	21
Inverse Analysis of Load-deflection Response.....	28
Data Reduction by Average Residual Strength Method (ARS).....	37
Comparison between Post-peak Residual Strength and ARS Method.....	37
Development of Design Equations for Flexural Response	39
Minimum Flexural Post-crack Tensile Strength Requirements	39
Minimum Post-crack Tensile Strength for Shrinkage and Temperature.....	40
Design Example for Slab on Grade.....	41
Conclusion.....	43
Chapter 4. Internal Curing	45
Introduction	45
Curing Aspects of HPC	45
Early-Age Shrinkage	47
Experimental Program.....	48
Results and Discussion of Compressive Tests	52
Conclusion.....	60
Chapter 5. High-Volume Fly Ash Concrete	61
Introduction	61
Mechanical Properties.....	61
Cracking Tendency of HVFA Concrete Due to Restrained Shrinkage.....	65
Conclusions	67
Chapter 6. Enhancing Durability Characteristics of Concrete	69
Introduction	69

Sulfate Attack and ASR	69
Guidelines for Material Design	72
Chapter 7. Procedures for Statistical Quality Control	81
Introduction	81
Statistical Analysis for Quality Assurance	83
Preliminary Study of Historical Data	91
Control Chart Design	95
Performance of the Combined Control Charts	96
Experimental Results and Further Discussion	97
Further Comparisons of the CUSUM-Run and EWMA-Run Charts.....	100
Pay Factor Criteria	101
Conclusions	102
References	103

LIST OF TABLES

Table 1. Sample Oxide Analysis for Fly Ash and Cement (Portland Cement Association, 2009).....	5
Table 2. Proposed HPC Classes Based on Specifications, Materials, Admixtures, and Testing Methods.....	10
Table 3. Specifications for Type A HPC.....	11
Table 4. Specifications for Type B HPC.....	11
Table 5. Specifications for Type C HPC.....	12
Table 6. Sample Specifications for Type C HPC.....	13
Table 7. Specifications for Type J HPC.....	14
Table 8. Physical Properties of Fibers Used.....	18
Table 9. Mixture Proportions and Compressive Strength of all Mixes.....	20
Table 10. Summary of Flexural Tests of Plain and Glass Fiber Reinforced Concrete.....	22
Table 11. Summary of Experimental Analysis on Flexural Data of Polymeric Fibers.....	24
Table 12. Summary of Experimental Analysis on Flexural Data of Polymeric Fibers.....	26
Table 13. Summary of Experimental Analysis of Polymeric Fibers (Types 2, 3, 4 and 5).....	28
Table 14. Back-calculated Tensile Parameters of Flexural Samples Using a Plasticity Model...	34
Table 15. Back-calculated Tensile Parameters of Flexural Samples Using the Strain-softening Model.....	36
Table 16. The Scope of the Test Program.....	49
Table 17. Mix Design of All Mixes.....	49
Table 18. Particle Size Distribution of the Lightweight Aggregates Used in This Study.....	51
Table 19. Specific Gravities, Absorption, and Void Content of LWAs Used in This Study.....	51
Table 20. Compression Data Summary (Low-strength Level).....	55
Table 21. Compression Data Summary (Mid-strength Level).....	59
Table 22. Compression Data Summary (High-strength Level).....	60
Table 23. Mixture Proportions of HVFA Concrete.....	61
Table 24. Compression Test Results for the HVFA Concrete Samples at 7 and 28 Days.....	63
Table 25. Three-point Bending Test Results for HVFA Concrete Samples at 7 and 28 Days.....	64
Table 26. Chemical and Physical Properties of Raw Cementitious Materials.....	69
Table 27. Requirements to Protect against Damage to Concrete by Sulfate Attack (Takada et al., 1998).....	72

Table 28. Minimum Levels of Pozzolanic Replacement and Alkalinity that Will Provide Various Levels of ASR Prevention (Thomas, Fournier & Folliard, 2008).	73
Table 29. Allowed Alkali Contents to Provide Various Levels of ASR Prevention (Collins & Sanjayan, 1999).....	73
Table 30. Protective Quality Based on Autoclam Air Permeability Index (Basheer, 1993).	73
Table 31. Mixture Proportions of the AR Glass and Control Samples (lb/ft ³).	74
Table 32. Mean Crack Width and Standard Deviation of Samples after 14, 21, and 28 Days.	79
Table 33. Sample Calculations of CUSUM with and without Resetting after an Out-of-control Signal Is Detected.	86
Table 34. Sample Calculations of EWMA Chart (All Values Are in psi).	88
Table 35. ARL Performance of the Two-sided EWMA Control Chart with Varying L , λ , and Shift Size.	90
Table 36. ARL Performance of the One-sided CUSUM with Various Values of k and h and with No Mean Shift.	91
Table 37. Test Case Data Sets.....	93
Table 38. Statistics Summary for Samples A11, A12, A13, A21, A22, and A23.	95
Table 39. Test Case Summaries When Monitoring the Process Mean.....	97
Table 40. Test Case Summary Classification.	100

LIST OF FIGURES

Figure 1. Scanning Electron Microscope (SEM) Image and X-ray Diffraction Pattern for a Typical Class F Fly Ash.....	5
Figure 2. Effect of Metakaolin in a) Increasing Compressive Strength, b) Reducing Water Penetration (W.P.), Water Absorption (W.A), Gas Permeability (G.P.), and Electrical Resistivity (E.R.) (Shekarchi et al., 2009).	7
Figure 3. Effect of Metakaolin Replacement Level on ASR Expansion (Shekarchi et al., 2009).	7
Figure 4. HPC Use in the United States Transportation Sector as of 2006-07 (Triandafilou et al., 2007).	8
Figure 5. Cleanup Operation for a Canal during Construction When an Occasional Rainfall Results in Debris Accumulation and Grade Changes of the Prepared Base. Photo Courtesy of Rich Shelly, Pulice Construction Co.	16
Figure 6. a) Closed-loop Flexural Test Setup, b) Measuring CMOD at the Notch by Extensometer and Displacement at Mid-span by the LVDT.	18
Figure 7. Crack Growth in FRC Samples under a Three-point Bending Test.....	19
Figure 8. Effect of AR Glass Fibers on Flexural Response after a) 1 Day and b) 7 Days of Curing.	21
Figure 9. Effect of Polymeric Fibers on Flexural Responses at a) 14 Days and b) 28 Days.....	23
Figure 10. Casting of Shotcrete FRC Samples for Flexural and Compressive Strength Testing.	25
Figure 11. Effect of Polymeric Fibers on Flexural Responses at 8, 16, and 36 Hours.	25
Figure 12. Effect of Different Polymeric Fibers on the Flexural Response at 16 Hours.....	27
Figure 13. Stress-strain Material Model for FRC Strain Softening Materials:.....	29
Figure 14. Rectangular FRC Section and the Simplified Strain and Stress Variations in Bending (Soranakom & Mobasher, 2007b).....	29
Figure 15. Closed-form Moment Curvature Relationship (for Tensile Strain-softening and Hardening Response) and Applied for Calculation of Load Deflection of the Flexural Beam (Mobasher, 2011).....	31
Figure 16. a) Experimental Results and Simulated Flexural Load-deflection Response of Concrete with Glass Fibers b) Back-calculated Stress-Strain Relationship for a Control Sample at 7 Days.	33
Figure 17. a) Experimental Results and Simulated Flexural Load-deflection Response and b) Back-calculated Stress-Strain Relationship for a Control Sample at 7 Days.	33
Figure 18. Experimental and Simulated Load-deflection Response and Back-calculated Stress-Strain Relationship of Three Samples with Different Fiber Types and Contents Tested at 28 Days.....	35

Figure 19. Comparison of Stress Distribution Determined Using the Present Approach and the ARS Method.	38
Figure 20. Comparison of Post-peak Strength with ARS for Various Types of Fibers.....	38
Figure 21. Grain Size Distribution of Fine Aggregate.....	50
Figure 22. The Aggregates Used in This Study: a) Normal Weight Aggregate, b) Bottom Ash Aggregate, and c) Sintered Bottom Ash Aggregate.....	50
Figure 23. Submerged Lightweight Aggregates in Water: a) Bottom Ash, b) Sintered Bottom Ash, and c) Saturated Surface-dry Condition of Aggregates Prior to Use.	52
Figure 24. Casting Concrete with Lightweight Aggregate: a) Materials before Pouring into Mixer and b) Materials after Mixing.	52
Figure 25. Comparative Results of Compression Tests at 7 Days (Low-strength Level).	53
Figure 26. Comparative Results of Compression Tests at 28 Days (Low-strength Level).	54
Figure 27. Effect of Internal Curing on the Compressive Test Results (Low-strength Level).....	54
Figure 28. Comparative Results of Compression Tests at 7 Days (Mid-strength Level).	56
Figure 29. Comparative Results of Compression Tests at 28 Days (Mid-strength Level).	56
Figure 30. Effect of Internal Curing on the Compressive Test Results (Mid-strength Level).	57
Figure 31. Comparative Results of Compression Tests at 7 Days (High-strength Level).....	57
Figure 32. Comparative Results of Compression Tests at 28 Days (High-strength Level).....	58
Figure 33. Effect of Internal Curing on the Compressive Test Results (High-strength Level).	58
Figure 34. Curing of Specimens in the Water Tank at a Constant Temperature of 70° F.....	62
Figure 35. Closed-loop Compression Test Setup.	62
Figure 36. Compressive Stress vs. Axial Strain of HVFA Concrete at a) 7 Days and b) 28 Days.	63
Figure 37. a) Closed-loop Flexural Test Setup; b) Measuring CMOD at the Notch by Extensometer and Displacement at the Mid-span by LVDT.	64
Figure 38. Flexural Response of Load vs. CMOD of HVFA Concrete at 7 and 28 Days.....	65
Figure 39. Configuration and Geometry of the Ring Test Specimen.	65
Figure 40. Shrinkage Chamber (with Cover Door Removed) Designed to Subject Restrained Concrete Ring Samples to Low Humidity Conditions.	66
Figure 41. Strain Gauge Readings vs. Time for HVFA Concrete Specimen.	66
Figure 42. Examination of HVFA Concrete Specimens after Exposure to the Shrinkage Chamber.	67
Figure 43. Expansion Curves for Standard Size Paste Specimens with 30 Percent Fly Ash.	70
Figure 44. SEM Images and EDS Spectra for Ettringite Formation in Sulfate Attack.	70
Figure 45. Effect of 30 Percent Fly Ash Replacement on ASR Expansion (ASTM 1567).....	71

Figure 46. SEM for a Typical ASR Gel Formed in Control Specimen.	71
Figure 47. Typical Results Obtained Using a Strain Gauge Attached to a Steel Ring in a Plain Concrete Sample.	75
Figure 48. Effect of an AR Glass Fiber Addition on Results Obtained Using Strain Gauges Attached to Steel Rings.	75
Figure 49. Digital Camera Used for Crack Investigations and Crack Width Measurement.	76
Figure 50. Transverse Cracks Caused by Restrained Drying Shrinkage on a) Control Sample and b) ARG5.0 Sample after Being Kept for 14 days in a Shrinkage Chamber.	76
Figure 51. Reconstructed Shrinkage Crack Images of Control Group and ARG5.0 Samples.	77
Figure 52. Steps in the Analysis of 1 of 8 Images Taken along the Bottom Side of a Crack.	78
Figure 53. Mean and Standard Deviations of Shrinkage Crack Width of All Mixtures.	80
Figure 54. Comparison of the CUSUM Chart for Table 33 with Resetting ($C_i^+ w/reset$ and $C_i^- w/reset$) and without Resetting (C_i^+ and C_i^-) When an Out-of-control Signal Is Detected	86
Figure 55. EWMA Chart for the Data (CL = Control Limit, UCL =Upper Control Limit, and LCL = Lower Control Limit) in Table 34.	89
Figure 56. Correlation of Data Representing the Specified Strength of Concrete Delivered to a Job Site for a Single Ready-mix Producer. The Solid Line Represents a 1-to-1 Correlation.	92
Figure 57. Probability Plot for Samples A11, A13, A21, A22, and A23	94
Figure 58. Plot of the Combined Control Charts for Project C21 (Subgroup Size=2) When $f'_c = 3,000$ psi (N =16).	97
Figure 59. Plot of the Combined Chart for Project D12 (Subgroup Size=2) When $f'_c = 4,000$ psi (N=6).	98
Figure 60. Plot of the Combined Chart for Project D13 (Subgroup Size=2) When $f'_c = 3,500$ psi (N=20).	99
Figure 61. Plot of the Combined Chart for Project F4 (Subgroup Size=2) When $f'_c = 4,500$ psi (N=19).	99

LIST OF ABBREVIATIONS AND ACRONYMS

AASHTO	American Association of State Highway and Transportation Officials
ACI	American Concrete Institute
AD	Anderson-Darling
ADOT	Arizona Department of Transportation
AEA	Air-entraining agent
Al ₂ O ₃	Aluminum oxide
Al ₂ Si ₂ O ₇	Metakaolin
AR	Alkali-resistant
ARL	Average run length
ARPA	Arizona Rock Products Association
ARS	Average residual strength
ASR	Alkali-silica reactivity
Caltrans	California Department of Transportation
Ca(OH) ₂	Calcium hydroxide
CaO	Free lime
CMOD	Crack mouth opening deformation
CO ₂	Carbon dioxide
C-S-H	Calcium silicate hydrate
CUSUM	Cumulative sum
DOE	Design of experiments
DTA	Differential thermal analysis
E.R.	Electrical resistivity
EDS	Energy dispersive spectography
EWMA	Exponentially weighted moving average
FAST	Field office automation system
Fe ₂ O ₃	Iron oxide
FHWA	Federal Highway Administration
FRC	Fiber-reinforced concrete
G.P.	Gas permeability
HPC	High-performance concrete
HVFA	High-volume fly ash
K ₂ O	Potassium oxide
keV	Kilo electron volts
KGA	Alkalinity of cement, in kilograms
LBA	Alkalinity of cement, in pounds
LOI	Loss on ignition
LRFD	Load and resistance factor design
LVDT	Linear variable differential transformer
MgO	Magnesium oxide
MK15	Metakaolin, 15 percent replacement level
MOR	Modulus of rupture
Na ₂ O	Sodium oxide
NaOH	Sodium hydroxide

NCHRP	National Cooperative Highway Research Program
-O-	Ether
-OH	Hydroxyl
QA	Quality assurance
QC	Quality control
RCPT	Rapid chloride permeability test
s/cm	Sand/cement (ratio)
SCM	Supplementary cementitious materials
SEM	Scanning electron microscope
SFRC	Steel fiber-reinforced concrete
SiO ₂	Silicon dioxide
SO ₃	Sulfur trioxide
SP	Superplasticizer
SPC	Statistical process control
SRA	Shrinkage-reducing admixture
TBD	To be determined
TGA	Thermogravimetric analysis
W.A.	Water absorption
W.P.	Water penetration
w/b	Water/binder (ratio)
w/c	Water/cement (ratio)
w/cm	Water/cementitious materials (ratio)
WWF	Welded wire fabric

CHAPTER 1. INTRODUCTION

The “Economical Concrete” project, sponsored by the Arizona Department of Transportation (ADOT) and carried out by researchers at Arizona State University, showcases several new aspects of using materials science and structural mechanics to conduct a sustainable design of concrete materials for use in the transportation sector. Many of the aspects discussed and developed in this report also may be more broadly applicable to all structural concrete materials.

To consider both aspects of sustainability and economics, the transportation community must first address material choices from technically feasible production and construction methods. Furthermore, as the structures are put into service, life cycle maintenance costs of structural systems become important. Traditional methods to design and construct reinforced concrete structures based on simplified specifications and empirical design tools needs to be re-evaluated as well. These methodologies ignore the tensile capacity of concrete, treat the cracking and associated durability problems as an afterthought, and are inherently inefficient, wasteful, and expensive. Using innovative materials and blended cement systems designed according to fundamental aspects of materials science would allow for the design of more efficient structural systems.

The topics addressed in this report include blended cements, fiber-reinforced concrete (FRC), internal curing with lightweight aggregate, and statistical process control (SPC). The objective was to address new specifications, analysis, and design guidelines so that material models can be directly integrated into structural analysis software. Emphasis is placed on developing alternative solutions that allow for sustainable development of infrastructure systems using blended cements, mechanics of materials, SPC, and design for durability.

This report discusses materials, methodologies, and test methods to enhance the performance and durability of concrete. Properties of pozzolans, blended cements, fly ashes, and other materials, along with proposed categories of high-performance concrete (HPC) mixtures are briefly described. The report also addresses early-age cracking and drying shrinkage, both of which reduce load-carrying capacity and accelerate deterioration, resulting in increased maintenance costs and reduced service life. The use of admixtures and supplementary cementitious materials for quality improvement and cost reduction are addressed using formulations containing up to 35 percent class F fly ash as cement replacement. The effectiveness of different pozzolans in making concrete a high-performance material was investigated by mechanical and durability experiments (such as long-term sulfate attacks and alkali-silica reactivity [ASR] tests). The current directives on the reduction of the maximum cement requirements, and increases in the limits of the use of class F fly ash, can be used to specify mixtures that meet the sustainability criteria and reduce the carbon footprint of cement use considerably.

The second aspect of this report addressed new developments in HPC materials using FRC. Using a series of experimental and theoretical derivations, it is shown that considerable cost savings can be realized by using high-volume fraction fiber mixtures, which can provide load-carrying capacity and ductility. These mixtures can be used for canal lining, shotcrete applications, elevated slabs, bridge decks, retaining wall sections, and many other applications

where heavy reinforcement and high flexural and shear loading cases are applied. As new software tools for analyzing and designing FRC materials are developed, cost-effective alternatives are identified that can reduce labor and mobilization expenses. This report presents an evaluation of various fiber systems that can be used to design and analyze beams, slabs, retaining walls, and buried structures. The authors present simple examples that are related directly to the design of slabs with FRC.

This report also addresses internal curing techniques as a means of improving the quality of normal- and high-strength concrete mixtures containing blended cements. As pozzolanic materials such as fly ashes participate in slow acting reactions in a blended cement system, the demand for curing water can be much greater than that of ordinary portland cement concrete. When this water is not readily available (e.g., because of the emptying of the capillary porosity), significant autogenous deformation and early-age cracking may result. On the other hand, most high-performance concretes having a low water-to-binder (w/b) ratio contain insufficient mixing water to maintain the water-filled coarse capillaries needed to sustain cement hydration and pozzolanic reactions. Therefore, a method of curing based on internal water supply would be very effective for this type of concrete. The researchers studied applications of pre-soaked lightweight aggregate as an internal water supply for curing of concrete. The superior results of internally cured samples with lightweight aggregates, especially sintered bottom ash, indicate a great potential for them to be used in hot-weather concreting or when external curing is not possible, practical, or economical.

New methods for statistical data processing of concrete strength data are proposed. Current contract specifications prescribe concrete based on minimum acceptable strength measures and force producers to supply excessively high-strength concrete mixtures to address the statistical variations of the test results. In recent years, sustainability of infrastructure systems has been the main cost driver for new materials and design methods. Furthermore, life cycle cost modeling has shown the superiority of various construction alternatives simply because the total cost of the project is reduced by choosing an alternative that may be more expensive than the traditional reinforced concrete system while the cost of labor, mobilization, and placement is reduced. Several technical tools were developed to improve the design, handling, and production process. Performance-based specifications that address the serviceability, workability, and long-term durability of test methods and procedures are presented using two new techniques—cumulative sum (CUSUM) and exponentially weighted moving average (EWMA)—which allow for process control and help in quality control (QC) monitoring of the data. This report emphasizes specifications for quality assurance (QA) and introduces quality measures as criteria for reducing the cost of concrete.

CHAPTER 2. CONCRETE MATERIALS FOR A SUSTAINABLE INFRASTRUCTURE

A CASE FOR SUSTAINABLE INFRASTRUCTURE SYSTEMS

Continuous maintenance and operation of civil infrastructure systems in support of prosperity, safety, and economic productivity is a challenge faced by both state and federal governments. In terms of building materials, concrete is the most commonly used throughout the world, and there is a staggering demand for its production and utilization. The exponential growth of infrastructure, especially in developing regions, further increases the demand for concrete materials such that the worldwide production and use of concrete has surpassed 10 billion tons per year (CEMBUREAU 2013). In the United States, concrete production almost doubled from 220 million cubic yards per year in the early 1990s to more than 430 million cubic yards in 2004. Arizona utilized more than 15 million cubic yards of concrete products per year in 2004, and at a cost ranging from of \$100 to \$400 per cubic yard, this number translates into an economic impact of up to \$6 billion (Damtoft et al., 2008).

Cement production generates one ton of carbon dioxide (CO₂) per ton of cement and contributes as much as 7 percent to the total production of greenhouse gases. The environmental requirements applied to coal-burning power plants also have increased challenges for the use or disposal of coal-burning by-products. Any optimization in the use of concrete products or long-term increase in the durability of existing infrastructure systems will be beneficial in helping to meet sustainability goals, reduce global CO₂ emission, and improve quality of life (Yunovich, Thompson & Virmani, 2004; Roy, 1999). The U.S. cement industry, led by the Portland Cement Association, has adopted a year 2020 voluntary target of reducing CO₂ emissions by 10 percent (from a 1990 baseline) per ton of cementitious product produced or sold. Implementing methods and recommendations for quality monitoring and control will have a direct impact on the sustainability efforts of the cement production industry (Portland Cement Association, 2009).

The main topics addressed in this project may be categorized into four major groups: blended cements, HPC, FRC, and the use of SPC procedures to monitor QC/QA of concrete construction. Within these groups, the researchers considered mechanical properties, shrinkage cracking tendency, high-volume fly ash (HVFA) concrete, and the effect of fly ash on enhancing the performance of concrete against sulfate attack and ASR mitigation. These issues are addressed in detail throughout this report and serve to integrate the need to better address materials used for the next generation of transportation infrastructures.

BLENDED CEMENTS

Blended cement concretes, which are obtained by the partial replacement of portland cement with pozzolanic materials, have improved mechanical properties and durability characteristics compared to ordinary concrete formulations (Nikam, Rane & Deshmukh, 2005; American Coal Ash Association, 2003; Mehta, 2004; Shekarchi et al., 2009). Blended cements have been used for decades to improve the mechanical properties and durability characteristics of cement-based materials. Using pozzolanic materials such as fly ash, silica fume, slag, and metakaolin

($\text{Al}_2\text{Si}_2\text{O}_7$) has resulted in economical and environmental benefits in the concrete industry (Nikam, Rane & Deshmukh, 2005; American Coal Ash Association, 2003). To reduce dependence on portland cement, the transportation industry needs to provide guidance and promote the use of various blended cement formulations in accordance with the guidelines and specifications of organizations such as the American Association of State Highway and Transportation Officials (AASHTO), Federal Highway Administration (FHWA), American Concrete Institute (ACI), and ASTM. This study investigated the potential benefits of using blended cements in terms of both sustainability and durability, and this report addresses aspects of using blended cements including sulfate attack, ASR mitigation, and internal curing.

Pozzolans

Pozzolanic materials improve the microstructure of concrete due to their particle size, and they may alter chemical compositions and hydration reactions in blended cements. The pozzolanic reactivity controls how much portlandite is consumed and converted to calcium silicate hydrate (C-S-H) (Bentz & Garboczi, 1991). Over the past several decades, researchers have studied the effectiveness of blended cement materials in reducing the level of damage from sulfate attack, but the role of chemical composition of pozzolanic materials needs to be studied more precisely (Tuthill, 1936; Kalousek, Porter & Benton, 1972; Monteiro & Kurtis, 2003). This report addresses recent developments in the areas of use of blended cements and procedures to use pozzolanic materials for ASR and sulfate attack mitigation.

Fly Ash

Coal-fired electric and steam-generating plants produce fly ash as a by-product. Typically, coal is pulverized and blown with air into the boiler's combustion chamber where it ignites, generating heat and producing a molten mineral residue. Boiler tubes extract heat from the boiler, cooling the flue gas and causing the molten mineral residue to harden and form ash. Coarse ash particles, referred to as bottom ash or slag, fall to the bottom of the combustion chamber, while the lighter fine ash particles, termed fly ash, remain suspended in the flue gas. Prior to exhausting the flue gas, particulate emission control devices, such as electrostatic precipitators or filter fabric bag-houses, remove the fly ash (American Coal Ash Association, 2003). According to a Portland Cement Association report on fly ash, about 100 million tons of fly ash is produced each year, of which only 20 percent is used in engineering applications such as blended cements, road base stabilization, and land filling (Portland Cement Association, 2009). In addition to the economic and environmental benefits of using fly ash in concrete, there is a technical advantage in increasing strength and improving mechanical properties (Nikam, Rane & Deshmukh, 2005). Using fly ash reduces greenhouse gases, decreases life cycle costs, and increases the concrete's durability.

Class F fly ashes have a lower calcium oxide (CaO) content than class C fly ashes, as shown in Table 1. This is a key factor in mitigating sulfate attack and ASR. Changes in the sources of coal used in power generation plants result in changes in the quality of fly ash by-product. Figure 1 shows scanning electron microscope (SEM) micrographs of the small and characteristically round fly ash particles. The figure also shows the X-ray diffraction pattern of class F fly ash,

illustrating the general amorphous nature of flyash containing quartz and mullite as the few crystalline phases present.

Table 1. Sample Oxide Analysis for Fly Ash and Cement (Portland Cement Association, 2009).

Component Compounds	Class F Fly Ash, %	Class C Fly Ash, %	Portland Cement, %
SiO ₂	55	40	23
Al ₂ O ₃	26	17	4
Fe ₂ O ₃	7	6	2
CaO	9	24	64
MgO	2	5	2
SO ₃	1	3	2

SiO₂ = silicon dioxide; Al₂O₃ = aluminum oxide; Fe₂O₃ = iron oxide; MgO = magnesium oxide; SO₃ = sulfur trioxide

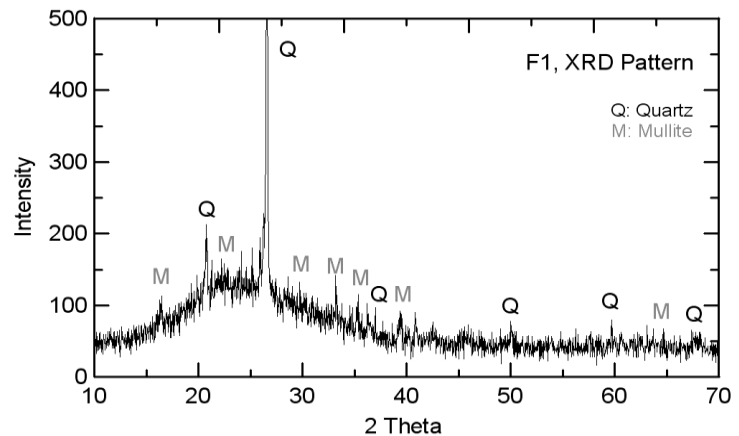
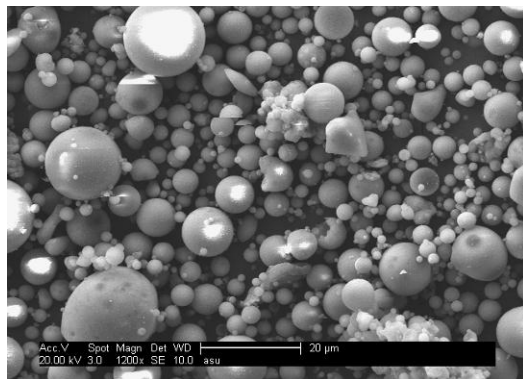


Figure 1. Scanning Electron Microscope (SEM) Image and X-ray Diffraction Pattern for a Typical Class F Fly Ash.

Class C ashes generally are derived from sub-bituminous coals and consist mostly of calcium alumino-sulfate glass, such as quartz (SiO₂) and free lime (CaO). Class C ash sometimes is referred to as high-calcium fly ash because it contains as much as 20 percent CaO. Typical oxides of fly ash and their quantities are shown in Table 1.

High-Volume Fly Ash

In commercial practice, the dosage of fly ash is limited to 15 to 20 percent by mass of the total cementitious material. Usually, this amount has a beneficial effect on the workability and economy of concrete, but it may not be enough to improve durability sufficiently to address sulfate attack, ASR, or shrinkage and thermal cracking. For this purpose, larger amounts of fly

ash, on the order of 25 to 35 percent, may be used. The dosage of fly ash in HVFA concrete can exceed 50 percent and may change the chemistry and reactivity of the cementitious phase in concrete (Malhotra & Mehta, 2005). Additional specifications are therefore required for its implementation. Adoption of concrete mixtures with HVFA would enable the concrete construction industry to become more sustainable, since incorporation of HVFA reduces water demand, improves workability, minimizes cracking caused by thermal and drying shrinkage, and enhances durability to reinforcement corrosion, sulfate attack, and ASR (Mehta, 2004). This report addresses a limited study conducted to address HVFA with a cement replacement level in the range of 35 percent.

Metakaolin

Commercially available since the mid-1990s, metakaolin ($\text{Al}_2\text{Si}_2\text{O}_7$) has been used as a high-reactivity pozzolan for HPC applications. Metakaolin is a thermally activated alumino-silicate material that is manufactured primarily by calcination of kaolin clay in a temperature range of 1,300 to 1,560° F (700 to 850 °C) (Sabir, Wild & Khatib, 1996). It typically contains 50 to 55 percent SiO_2 and 40 to 45 percent Al_2O_3 (Poon et al., 2001). A recent experimental program evaluated the mechanical and durability properties of concrete with metakaolin (Shekarchi et al., 2009). The researchers prepared concrete samples with 0, 5, 10 and 15 percent metakaolin (by weight) replacement of portland cement. Results of samples with 15 percent replacement (MK15) are shown in Figure 2a. The compressive strength of the control and metakaolin mixtures ranged from 7,200 psi to 8,700 psi (50.0 MPa to 59.8 MPa), representing as much as a 20 percent increase for MK15. Water penetration decreased by as much as 50 percent for MK15, and gas permeability decreased up to 40 percent. Also, in the MK15 mixture, the water absorption potential decreased by 30 percent; the lowest absorption measured was 1.32 ± 0.10 percent, as shown in Figure 2b. The ASR expansion decreased by 80 percent, as shown in Figure 3.

Copper Slag

Copper slag, which contains 50 to 75 percent Fe_2O_3 and 15 to 35 percent SiO_2 , can be used in concrete as a cement or aggregate replacement. Since Arizona is the major producer of copper in the United States (Leaming, 1998), mining operations in this state generate significant quantities of copper slag. Replacing cement with slag lowers the cost of concrete and improves its durability properties (Mobasher & Devaguptapu, 1993). Researchers at Arizona State University have conducted significant research in this area (Tixier, Devaguptapu & Mobasher, 1997; Ariño & Mobasher, 1999).

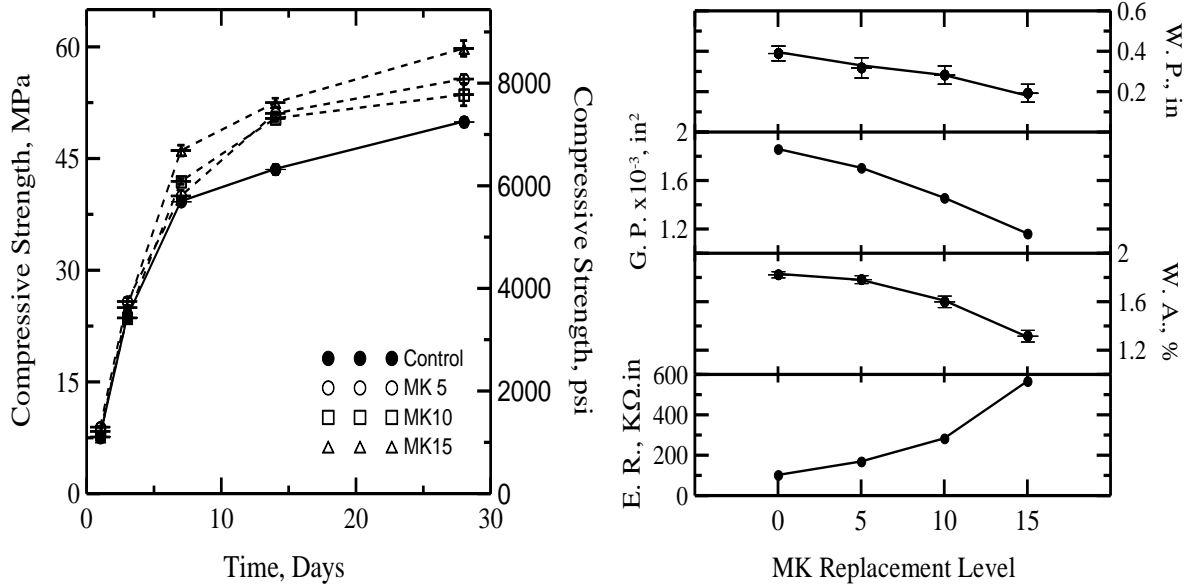


Figure 2. Effect of Metakaolin in a) Increasing Compressive Strength, b) Reducing Water Penetration (W.P.), Water Absorption (W.A), Gas Permeability (G.P.), and Electrical Resistivity (E.R.) (Shekarchi et al., 2009).

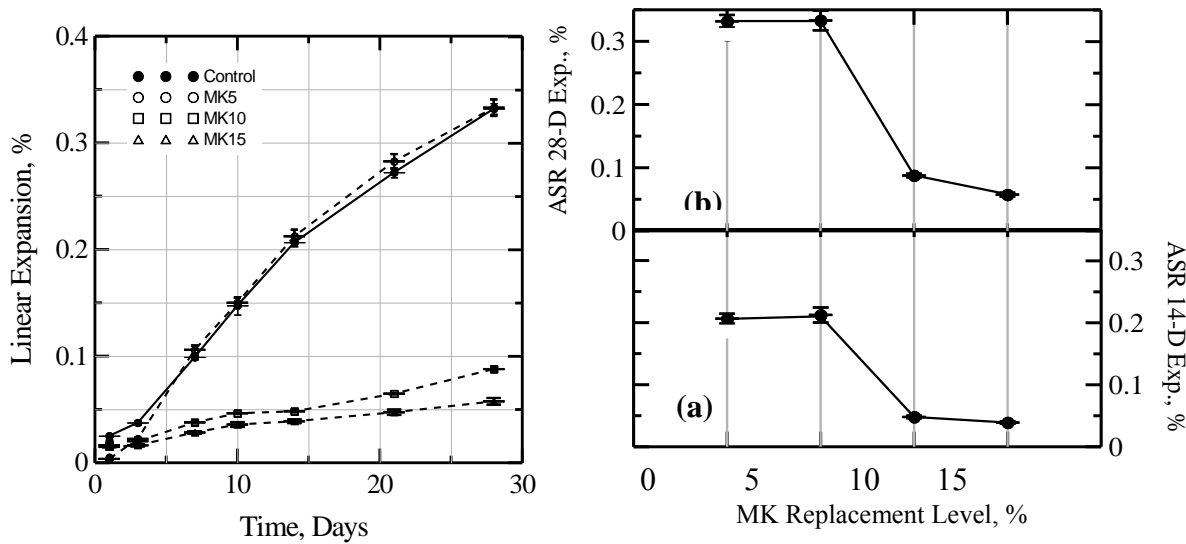


Figure 3. Effect of Metakaolin Replacement Level on ASR Expansion (Shekarchi et al., 2009).

HIGH-PERFORMANCE CONCRETE

HPC is a high-strength concrete with characteristics that improve workability, strength, and durability. The workability of HPC is such that the concrete can be mixed, transported, cast, and finished easily and properly with minimum possible energy and labor. The strength characteristics of HPC include high compressive strength (more than 6,000 psi) and high ductility (energy absorption). The durability of HPC should cover a wide area of physical and

chemical causes for degradation, such as freeze/thaw, abrasion, fatigue, fire resistance, sulfate attack, chloride ingress, carbonation, and ASR.

Use of HPC in transportation infrastructure systems leads to structures with longer spans, smaller columns, thinner slabs, longer service life, and improved appearance. Several reports have been published showing outstanding results from using HPC in high-rise buildings, bridges, and pavements (Malhotra & Mehta, 2005). FHWA has played a key role in the HPC technology transfer from research and development to routine practice for bridge and pavement design and construction. The success has been largely due to a long-term continuing partnership between the FHWA, state departments of transportation, AASHTO, local agencies, the private sector, and academic organizations (Vanikar & Triandafilou, 2005). According to Vanikar and Triandafilou, by 2005 HPC had been used in all states except Arizona, Idaho, North Dakota, Arkansas, and Mississippi, as illustrated in Figure 4.

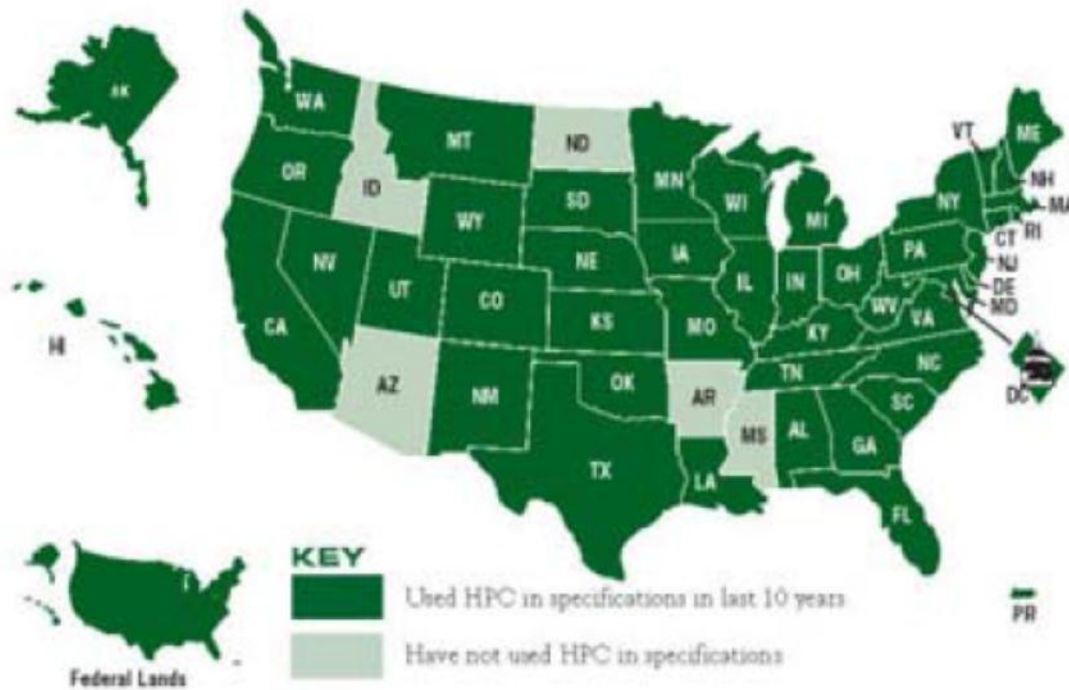


Figure 4. HPC Use in the United States Transportation Sector as of 2006-07 (Triandafilou et al., 2007).

According to Aïtcin, there are five classes of HPC based on the compressive strength, starting from a strength range of 7,200 to 11,800 psi (class I) and ending at a strength level of 21,800 psi or above (class V) (Aïtcin, 1998). While HPC can be made using portland cement alone as a cementitious material, a partial substitution of portland cement with one or more supplementary cementitious materials can be advantageous. HPC usually has a water to cementitious materials (w/cm) ratio of 0.42 or lower (down to 0.25), and high-range water reducers (superplasticizers) often are used for enhancing workability. Short chopped fibers (natural, synthetic, or steel) can be used for improving the tensile and flexural strengths (ductility) of HPC.

This study did not evaluate HPC directly through a systematic experimental program. However, since it is segmented into various aspects of materials science, different aspects of HPC are addressed based on the intended application. For example, Chapter 3 addresses high-early-strength FRC for application to shotcrete applications, and Chapter 4 presents an internal curing method as it relates to HPC, where the demand for curing water can be much greater than that in a conventional portland cement concrete (Bentz, 2007). Most HPC have a low water-to-cement (w/c) ratio and contain insufficient mixing water to maintain water-filled coarse capillaries needed to sustain cement hydration and pozzolanic reactions; therefore, they require water curing (Kovler & Jensen, 2007). However, the water-tightness and impermeability of the HPC mixtures has a deleterious effect on the efficiency of traditional external curing, which depends primarily on the moisture transport process. As the internal curing agent is dispersed finely and part of the system, it can delineate the low permeability of cementitious systems with a low water to binder (w/b) ratio. Internal water supply can therefore be considered as an efficient method of curing HPC (Bentz, 2007).

According to a pending proposal to the joint task group by ADOT and Arizona Rock Products Association (ARPA), HPC formulations could be classified as several different categories. Table 2 presents different classes of HPC based on the specifications, materials, use of admixtures, and testing methods pertaining to each class.

Type A HPC

Type A HPC is specified for high early strength. The main specifications include a specific strength at a certain age. Materials variables include cement type, cement content, and use of specific proprietary admixtures such as superplasticizers, accelerator, and retarders. Within the applicable ASTM standards, maturity testing is the primary method in asserting strength development. Various sub-classes may be defined as shown in Table 3.

National Cooperative Highway Research Program (NCHRP) Report 540 addresses cases that are designed to open early to traffic, joint repair, and selected slab replacement (Van Dam et al., 2005). In the design of early-age strength, if a cement type other than specified is used, the long-term durability of the mixture should be at the same level of a standard specified cement-based system. Specimen conditioning is important for field-cured cylinders when tested in accordance with ASTM C39. The best way to test this is to duplicate a field cure condition by means of temperature matching (active, Sure cure, or passive, blanket, insulated box, etc.).

Typically, maturity testing in accordance with ASTM C1074 is specified. For example, representative compressive strength specifications include 1,200 psi specified in Pennsylvania, 1,450 psi in 7 hours or 2,500 psi in 24 hours in Georgia, and 2,500 psi in 12 hours in Maryland (Van Dam et al., 2005).

Table 2. Proposed HPC Classes Based on Specifications, Materials, Admixtures, and Testing Methods.

Type	Category	Main Specifications	Materials	Admixtures	Testing
A	High early strength	f'_c at specific age	Cement type, content	SP, accelerator, retarders	Maturity, f'_c
B	Freeze/thaw	f'_c + air content	Max aggregate size	Air entrainment	ASTM C666, ACI 211
C	Low permeability	w/c, air content, curing	Type II cement	SP, SRA, pozzolans, AEA	RCPT
D	$f'_c > 5,000$ pci	f'_c , curing	Cement, fly ash, SF, special aggregates, gradation	SP, retarders	f'_c
E	ASR + sulfate attack	Cement II/V + pozzolans, geographic locations	Aggregates, cements	SP, pozzolans, lithium salts	Modified C1260, C227, C1012
F	FRC, low fiber content	Plastic shrinkage cracking, impact, durability	Fibers	SP, water reducers	C1399, C1018, C1550
G	FRC, high fiber content	WWF, rebar replacement impact, durability	Fibers	SP, water reducers	C1399, C1018, C1550
H	Low shrinkage	w/c, cement content, air content, curing	Cement type, shrinkage compensating cement admixtures	SRA, fibers, SP, air	Mortar bars, C157, shrinkage
I	Self-consolidating concrete	Modified flow/ >8000 psi	Combined aggregate grading	Viscosity modifiers	Modified slump, rheometer
J	Low cement factor	f'_c at specific age	Cement type	SP, water reducers, pozzolans,	f'_c
K	High fly ash	f'_c at specific age	Fly ash to cement replacement >25%	SP, water reducers, blends of pozzolans,	f'_c
L	Internal curing	f'_c under adverse curing conditions	Lightweight aggregate, sintered bottom ash	SP, water reducers	TGA/DTA X-ray, SEM

f'_c = compressive strength; SP = superplasticizer; SRA = shrinkage reducing admixtures; AEA = air-entraining admixture, TGA = thermogravimetric analysis, DTA = differential thermal analysis, WWF = welded wire fabric, RCPT = rapid chloride permeability test

Table 3. Specifications for Type A HPC.

Class	Specifications*	Cement Type and amount	Admixtures Type, Supplier	Ready Mix	Test Methods
A1	$f'_c = 3,000$ psi in 8 hrs.**	minimum type II 740-900 lb/yd ³ type III 660-825 lb/yd ³	Non-chloride admixtures: Accelerator, Superplasticizer, hydration control, AEA	Membrane cure, blankets	NCHRP 540 [25]
A2	$f'_c = 3,000$ psi in 12 hrs.	minimum type II 740-900 lb/yd ³ type III 660-825 lb/yd ³ possibly fly ash	Non-chloride admixtures: Accelerator, Superplasticizer, hydration control, AEA, fly ash, metakaolin	Membrane cure, blankets	NCHRP 540
A3	$f'_c = 3,000$ psi in 24 hrs.	minimum type II 740-900 lb/yd ³ type III 660-825 lb/yd ³	Non-chloride admixtures: Accelerator, Superplasticizer, hydration control, AEA, mineral admixture, fly ash, metakaolin	Membrane cure, blankets	NCHRP 540
A4	Case by case				

* Specifications include compressive strength, flexural strength, or maturity

** Sampled and cured by field conditions

Type B HPC

Type B HPC is specified for freeze/thaw resistance of concrete. The main specifications involve a stated f'_c and a minimum air content with various air spacing factors. Materials specifications include minimum cement content, specific curing cycle, and a maximum aggregate size. The primary admixture is an air entrainment agent (AEA). Testing is in accordance with ASTM C666 and the recently developed ACI 211 specifications for freeze/thaw resistance. Various subclasses may be defined, as shown in Table 4.

Table 4. Specifications for Type B HPC.

Class	Specifications	Cement	Admixtures	Test Methods
B1	Up to 3% air	TBD	TBD	ACI 211
B2	3-7% air	TBD	TBD	ACI 211
B3	Freeze/thaw durability (χ =relative dynamic modulus after 300 cycles)	TBD	TBD	AASHTO T161 Procedure A
B4	% air selected by contractor, i.e. min 3%, max 9%	TBD	TBD	AASHTO T152

*Compressive strength, flexural strength or maturity, TBD = to be determined

Type C HPC

Type C HPC is specified for low permeability. The main specifications are w/c, air content, and curing. The materials include type I/II cement and admixtures including SP, SRA, silica fume, slag, fly ash, and AEA. The primary test method for characterization of permeability is the rapid chloride permeability test. Various sub-classes may be defined, as shown in Table 5.

Table 5. Specifications for Type C HPC.

Class	Specifications	Cement	Admixtures	Test Methods
C1	w/c, curing duration	TBD	TBD	TBD
C2	Chloride permeability	TBD	TBD	ASTM C1202 AASHTO T277
C3	Bridge deck applications	TBD	TBD	TBD
C4	Chloride penetration depth	TBD	TBD	See AASHTO T259 modified, Note A: Penetration 0.025% at 25mm

A sample set of specifications could be stated as shown in Table 6 (Stanish, Hooton & Thomas, 2000; Sprinkel, 2004).

The amount of electrical charge in amp-sec that pass through a 2-inch-long, 4-inch-diameter saturated cylindrical sample when a DC voltage of 60 volts is applied across it is reported as an indicator of concrete's permeability. Concrete mixtures are required to undergo specific pre-conditioning, including the following:

- For each subplot, the engineer will cast two 4- by 8-inch cylinder specimens. Samples 2 inches thick will be cut from the center of each cylinder for testing. The average of the results for the two test specimens for each subplot will be considered the subplot test value for permeability.
- Latex-modified concrete samples shall be moist cured 2 days in the molds (1 day at job site and 1 day in the lab), air cured 5 days in the molds in the laboratory, and 21 days out of the molds at 100° F air temperature.
- Silica fume and other non-latex samples shall be moist cured 7 days in the molds (1 day at job site and 6 days in the lab) and moist cured 21 days out of the molds in the laboratory at 100° F water temperature.

Table 6. Sample Specifications for Type C HPC.

Test Method		Considers Chloride Ion Movement	Constant Temperature	Unaffected by Conductors in the Concrete	Approximate Duration of Test Procedure
Long Term	AASHTO T259 (Salt Ponding)	Yes	Yes	Yes	90 days after curing and conditioning
	Bulk Diffusion (Nordtest)	Yes	Yes	Yes	40-120 days after curing and conditioning
Short Term	RCPT (T277)	No	No	No	6 hours
	Electrical Migration	Yes	Yes	No	Depends on the voltage and concrete
	Rapid Migration (CTH)	Yes	Yes	No	8 hours
	Resistivity	No	Yes	No	30 minutes
	Pressure Penetration	Yes	Yes	Yes	Depends on pressure (but potentially long)
Other	Sorptivity-Lab	No	Yes	Yes	1 week, including conditioning
	Sorptivity-Field	No	Yes	Yes	30 minutes
	Propan-2-ol Counter-diffusion	No	Yes	Yes	14 days with thin paste samples
	Gas Diffusion	No	Yes	Yes	2-3 hours

Type F and G HPC FRC with Low and High Fiber Content

Type F and G HPC represents concrete containing various levels and types of fibers, with their experimental compressive and flexural properties, and methods to characterize the ductility. These topics are addressed in detail in Chapter 3. Chapter 3 also presents other beneficial effects of fiber addition in enhancing the durability characteristics of concrete, especially by controlling early-age shrinkage cracking.

Type J HPC

Type J is a catch-all category addressing low cement factor mixtures. The main specifications include variations in the cement type, content, fly ash to cement ratio, w/c, and curing. Testing can be specified using a certain compressive strength at a specific age. Various sub-classes may be defined, as shown in Table 7.

Table 7. Specifications for Type J HPC.

Class	Specifications	Cement Type, Supplier	Admixtures Type, Supplier	Test Methods
J1	w/c, curing duration	Type II	TBD	TBD
J2	Ultra high Flyash Concrete	High fly ash cement ratio	TBD	TBD
J3	Bridge substructure applications		TBD	TBD
J4	Tertiary mixtures	Class C fly ash	TBD	TBD

Low minimum cement content is being considered for different classes of concrete materials. For example, the Maricopa Association of Government specifies a minimum of 420, 470, 520, and 600 lb/yd³ of cement for 2,000, 2,500, 3,000 and 4,000 psi concrete, respectively (Maricopa Association of Government Standards, 2012). ADOT specifications for class S and class B require a minimum of 564 lb/yd³ and 470 lb/yd³, respectively. For class K, a higher fly ash content (>25 percent) must be used. Age at acceptance is another alternative by specifying strength at 42 days or more from 28 days.

Recommendation for cement content may include terms that depend on the strength class. For example, for classes of 4,000 psi and above, the total content of cementitious materials (including fly ash) shall be 564 lb/yd³. For 3,000 to 4,000 psi, 517 lb/yd³ should be used, and for 2,500 psi, 470 lb/yd³ should be used. The minimum w/c recommended must be determined based on durability, shrinkage potential, freeze/thaw, and sulfate attack potential. Acceptance of concrete based on statistical mix design procedures and required strength based on ACI 318 will lead to economical use of HPC materials (Laungrungrong, Mobasher & Montgomery, 2008; American Concrete Institute, 2008).

Type K HPC

Type K HPC represents high fly ash concrete and specified as fly ash to cement replacement levels above the current 25 percent level. This type is discussed in detail in Chapter 5.

Type L HPC

Type L HPC represents the concrete specified using criteria for internal curing. Preliminary test data for these materials that may use lightweight aggregate, or sintered bottom ash under adverse curing conditions, are discussed in Chapter 4.

CHAPTER 3. FIBER-REINFORCED CONCRETE

INTRODUCTION

Plain concrete has a low tensile strength and a low strain capacity at failure. Designers of reinforced concrete overcome these shortcomings by adding reinforcing bars, welded wire meshes, and prestressing steel. Reinforcing steel is continuous and is located in the structure specifically to optimize performance. As an alternative to conventional reinforcement, fibers have been used as reinforcement as well. Concrete materials produced with short, randomly distributed fibers may be superior to forms of reinforcing concrete using welded wire mesh or rebars. Both the tensile strength and toughness, especially the post-crack strength, are improved (Bentur & Mindess, 1990). It has been shown that due to the reduced specific spacing, fibers strengthen the composite at the micro level by bridging the microcracks before they reach the critical flaw size (Mobasher & Li, 1996). The small diameter of the individual fibers ensures a better and more uniform distribution of reinforcement. In addition, the high surface area offers significant bond capability. Since the bond strength of glass, steel, or even polymeric fibers is far superior to reinforcing bars, this increases the efficiency of reinforcement so that there is limited crack opening due to the debonding and pullout of reinforcement. The fibers are distributed randomly, offering efficiency in load transfer by the fiber phase. Finally, because the fibers that bridge the matrix cracks are resilient and highly compliant, they can orient to carry the load across the crack faces. This factor is expected to increase the durability of concrete substantially, since the crack width control affects long-term durability.

Because of the flexibility in methods of fabrication, FRC can be an economic and useful construction material. In architectural cladding panels, slabs on grade, mining, tunneling, and excavation support applications, steel and synthetic FRC and shotcrete have been used in lieu of welded wire fabric reinforcement (American Concrete Institute Committee 544, 1996). There are numerous fiber types available for commercial and experimental use. It has been shown that hybrid reinforcement systems utilizing two or more fiber lengths can also be used to optimize composite performance for strength and ductility as a function of age (Mobasher, 2011). The basic fiber categories are steel, glass, synthetic, and natural materials. The studies in this report focused primarily on glass and polymeric FRC.

In addition to the general overview of FRC provided here, this chapter addresses mechanical properties of FRC with different types of polymeric and glass fiber. Specifically, the response under flexural bending tests is used to measure material properties that are needed in the design of various sections. The three-point bending test methodology is described, and the results of performing this test on different types of FRC are investigated. Due to the experimental and analytical limitations of available test methods, the researchers present an inverse analysis of the load-deflection response of these materials and for back-calculation of the stress-strain response for various fiber reinforced concrete samples (Gopalaratnam & Gettu, 1995; Gopalaratnam et al., 1991; Soranakom & Mobasher, 2007a). The chapter also presents a procedure that introduces a guideline for designing flexural FRC members based on calculated residual strength. This chapter also provides an examination of data reduction by the average residual strength (ARS) method and compares ARS strength and back-calculated residual strength. A comparison of

back-calculated post-crack tensile strength with available ASTM test methods is provided. It is shown that ASTM test methods may overestimate the residual strength (Soranakom & Mobasher, 2010). Finally, design equations for flexural response are presented along with a design example of slab on grade.

Economics of FRC

Use of FRC is associated with reduced labor costs, reduced potential for error at the job site, and efficiency in placement and compaction. Therefore, fibers are more economical than steel reinforcement and provide excellent strengthening mechanisms. Figure 5 shows the clean-up of operation for a canal project during construction. Clean-up is required due to sudden rainfall and its flow in the channel, resulting in debris accumulation and grade changes of the prepared base. Application of FRC in a canal lining project significantly reduces labor requirements in the construction phase since the rebar or mesh layout phase is eliminated. Instead of using a longitudinal and transverse rebar layout or a welded wire mesh, an FRC mix can be specified to meet system requirements at a much lower cost.



Figure 5. Cleanup Operation for a Canal during Construction When an Occasional Rainfall Results in Debris Accumulation and Grade Changes of the Prepared Base. Photo Courtesy of Rich Shelly, Pulice Construction Co.

Aerated FRC

Aerated concrete is a lightweight, noncombustible cement-based material manufactured from a mixture of fly ash or other sources of silica, portland cement, quick lime, gypsum, water, and aluminum powder or paste. These raw materials are mixed together and cast into large steel molds where a chemical reaction takes place. Hydrogen gas is generated in the wet slurry mixture, causing it to expand and form independent air cells. The chemical reaction caused by the addition of aluminum makes the mixture expand to about twice its volume, resulting in a highly porous structure. Approximately 80 percent of the volume of the hardened material is made up of pores, 50 percent being macro-pores and 30 percent being micro-pores characterized

by their ability in capillary moisture transport. Due to the special cellular structure of this material and its physical and mechanical properties, it is applicable in a variety of civil engineering applications. Aerated FRC precast blocks and panels can be used as sound wall systems along highways such as Arizona State Route 51 and Piestewa Peak, as well as in one- and two-story buildings as structural components with thermal insulation properties.

High Early-Strength FRC

High early-strength FRC is made by adding fibers and accelerator admixtures. As the name suggests, it has high early-age strength and high energy absorption capacity. This type of FRC is suitable for shotcrete applications, which must achieve high early strength and ductility within 24 hours. Using a shotcrete lining system as a means of initial shaft support instead of the traditional mesh and bolts increases the development speed (Vandewalle, 1993; Franzén, 1992). Several elements must be considered, including alternative techniques to achieve adhesion, strength, and ductility for the newly placed shotcrete materials.

FIBER TYPES

This study evaluated different types of non-metallic fibers. Table 8 lists the properties of a single type of glass fiber and five different types of polymeric fibers. As shown in the table, the base, specific gravity, modulus of elasticity, tensile strength, and length of fibers used cover a broad range. In the labeling system used, G refers to alkali-resistant (AR) glass and P represents polymeric. For example, FRC with AR glass fiber is a portland cement-based product that is made by using a mortar matrix and low dosages of chopped AR glass fibers, referred to as G-Type1. The various types of fibers used are identified as the base and refer to different manufacturers.

THREE-POINT BENDING TESTS

To better monitor the flexural response of concrete samples using closed loop testing, samples were pre-notched and loaded along the notch. The behavior of the specimen under flexure is dominated by the cracking that initiates at the notch and grows along the depth of the specimen. As the test progresses, the deformation localizes at the notch and is followed by crack propagation. Since the critical deformations are the opening of the crack tip that may be measured at the base of the notch, the best-controlled variable in flexure tests is the crack mouth opening or a similar displacement.

Table 8. Physical Properties of Fibers Used.

Fiber Type	G-Type 1	P-Type 1	P-Type 2	P-Type 3	P-Type 4	P-Type 5
Base	Alkali Resistance Glass	Fibrillated Polypropylene	Monofilament Polypropylene/ Polyethylene blend	Modified Olefin	Modified Polypropylene Blend	Fibrillated Polypropylene Fiber
Specific Gravity	2.68	0.91	0.92	0.9-0.92	0.91	0.91
Modulus of Elasticity	10,000 ksi	493 ksi	725 ksi	1450 ksi	950 ksi	800 ksi
Tensile Strength	250 ksi	87 ksi	87-94 ksi	80 ksi	95 ksi	60 ksi
Length of Fiber	1 in	0.75 in	2 in	2 in	1.5 in	2 in

Flexural tests may be conducted under several loading configurations. In this study, beams were loaded at a single point in the mid-span, which is known as the three-point bending test. The test is performed under closed loop control with crack mouth opening deformation (CMOD) as the controlled variable. Figure 6 represents the flexural test setup. In this test method, the CMOD was measured across the face of notch using an extensometer and a linear variable differential transformer (LVDT) with a 0.1-inch range measuring the deflection of the beam at the mid-span.



Figure 6. a) Closed-Loop Flexural Test Setup, b) Measuring CMOD at the Notch by Extensometer and Displacement at Mid-span by the LVDT.

Three-point bending flexural tests were performed on 21- by 6- by 6-inch or 18- by 4- by 4-inch beam specimens with an initial notch length of 0.5 or 1 inch and test span of 18 or 16 inches. Figure 7 shows the typical concrete beam under a closed-loop three-point bending test. The researchers observed that cracks initiate from the notch and extend up to the upper side of the

beam. However, the crack is bridged by the fibers, which are being pulled under this loading. The presence of fiber significantly increases the ductility of the material and makes the crack opening and deflection exceed 0.05 inches.



Figure 7. Crack Growth in FRC Samples under a Three-point Bending Test.

Mix Design and Compression Results

The researchers prepared and tested 14 mixtures under three-point bending tests, as shown in Table 9. The results of compression tests also are shown in the table. The w/cm ratios are in the range of 0.4 to 0.55, and cement content is 800 lb/yd³ except in two test series, in which the cement content was 1,100 lb/yd³. The fly ash and silica fume were added to some of mixtures as supplementary cementitious materials with dosages of 100 lb/yd³ and 25 lb/yd³, respectively. The sand-to-cement (s/cm) ratio is 2 or 1.9 for all mixtures. Accelerator admixtures were added to some of the mixtures, which led to gaining high early strength.

Table 9. Mixture Proportions and Compressive Strength of all Mixes.

Application	Mix ID	PC	Fly Ash	SF	S	CA	W	FB	FB Type	AC, %	w/cm	s/cm	f'_{c_s} psi
Shrinkage Control	Plain	1,100	0	0	2,200	0	605	0	N/A	0	0.55	2	4,811 _a
	GlassF5	1,100	0	0	2,200	0	605	5	AR glass Type1	0	0.55	2	4,670 _a
Slabs on Grade	PolyF9.5_Type1	800	0	0	1,600	1,200	400	9.5	P-Type1	0	0.50	2	4,000 _*
	PolyF5_Type2	800	0	0	1,600	1,200	400	5	P-Type2	0	0.50	2	4,000 _*
	PolyF5_Type1	800	0	0	1,600	1,200	400	5	P-Type1	0	0.50	2	4,000 _*
Shotcrete	B-CSA	800	100	25	1,850	800	390	10	P-Type3	4	0.42	2	4,860 _b
	B-CSB	800	100	25	1,850	800	390	12	P-Type3	4	0.42	2	4,680 _b
	B-HAS	800	100	25	1,850	800	390	10	P-Type3	8	0.42	2	6,170 _b
	B-HSB	800	100	25	1,850	800	390	15	P-Type3	8	0.42	2	5,840 _b
	1	800	100	25	1,750	670	375	10	P-Type 3	4	0.40	1.9	3,927 _b
	2	800	100	25	1,750	670	375	10	P-Type 2	4	0.40	1.9	4,208 _b
	3	800	100	25	1,750	670	375	10	P-Type 4	4	0.40	1.9	4,180 _b
	4	800	100	25	1,750	670	375	8.5 1.5	P-Type 3 P-Type 5	4	0.40	1.9	4,161 _b
	5	800	100	25	1,750	670	375	8.5 1.5	P-Type 4 P-Type 5	4	0.40	1.9	3,738 _b

PC = portland cement; SF = silica fume; S = sand as fine aggregate; CA = coarse aggregate; W = water; FB = fiber—all expressed as lb/yd³. AC = accelerator

*= not measured

^a At 28 days

^b At 24 hours

Specified 28 day strength

EXPERIMENTAL RESULTS OF THREE-POINT BENDING TEST

Results for AR Glass Fibers

General results indicate that AR glass fibers slightly delay the time of cracking but drastically reduce the crack widths. Flexural responses of these mixtures were examined in this study, and representative results of the three-point bending test for AR glass fibers are shown in Figure 8. Results of the experimental analysis on flexural data of glass fiber are also summarized in Table 10. The addition of fibers increases the post-peak response because as the fibers bridge the crack and pull out, additional energy is dissipated. Other studies have also examined the role of AR glass fibers in extending the cracking resistance of concrete subjected to drying shrinkage utilizing a ring-type restrained shrinkage test (Soranakom, Bakhshi & Mobasher, 2008). The area under the load deflection diagram was integrated numerically and the results were presented as flexural toughness.

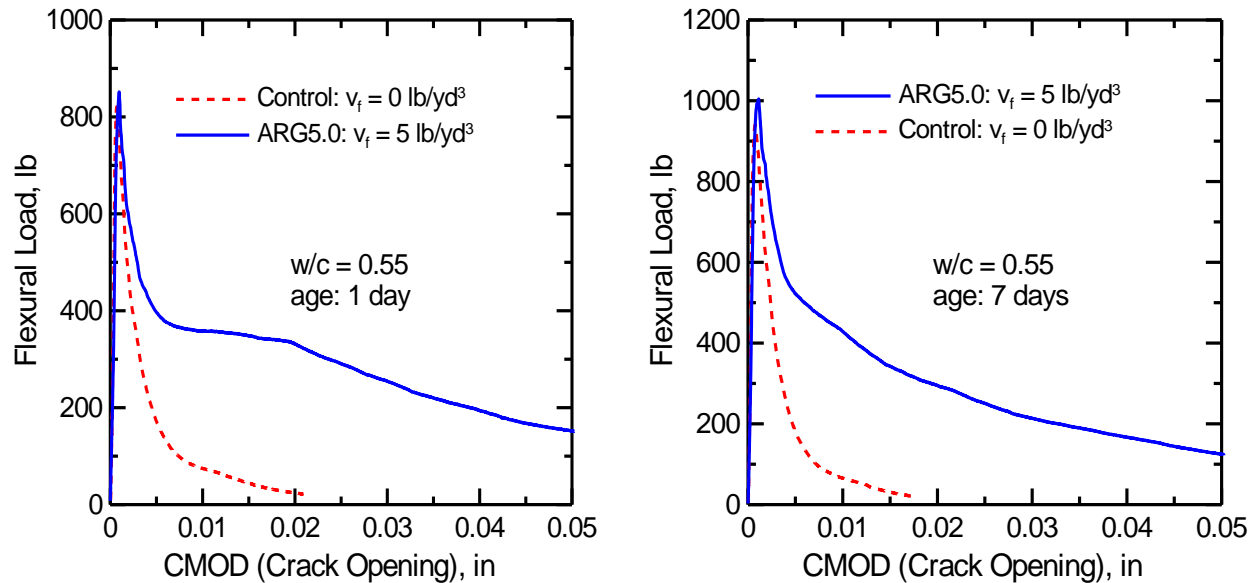


Figure 8. Effect of AR Glass Fibers on Flexural Response after a) 1 Day and b) 7 Days of Curing.

The results indicate that the elastic flexural stiffness of samples is as much as 11, 17, and 5 percent more than that of control samples (plain) after 1, 3, and 7 days of curing, respectively. While fiber addition does not affect the deflections at maximum flexural load, maximum flexural load and modulus of rupture (MOR) increase slightly at both 3 and 7 days. Finally, the flexural toughness increases significantly with the addition of 5 lb/yd³ AR glass fibers. Results show that average flexural toughness is 4.8, 4.9, and 4.2 times the flexural toughness of plain samples at 1, 3, and 7 days, respectively. The post cracking response in the strain softening region is the single most important aspect of fiber reinforcement at these loading rates. This parameter can be estimated for the closed loop testing using deflection or crack mouth opening displacement. The added level of ductility can be used in the design of the composites using fibers, but appropriate tools are needed to design based on ductility.

Table 10. Summary of Flexural Tests of Plain and Glass Fiber Reinforced Concrete.

Mix ID	Age, days	Statistical Measure	Elastic Flexural Stiffness, kips/in	Deflection at Max Flexural Load, in	Max Flex. Load, lbf	Modulus of Rupture, psi	Flexural Toughness, lbf-in
Plain	1	Average	565	0.0016	834	409	2.64
		Std. dev.	65	0.0001	21	10	0.10
	3	Average	639	0.0016	918	450	2.60
		Std. dev.	41	0.0001	4	2	0.15
	7	Average	708	0.0016	952	467	3.02
		Std. dev.	69	0.0001	16	8	0.28
GlassF5	1	Average	627	0.0016	829	406	12.73
		Std. dev.	65	0.0002	25	12	1.22
	3	Average	745	0.0016	979	480	12.80
		Std. dev.	48	0.0000	21	11	3.04
	7	Average	745	0.0018	1,014	497	12.46
		Std. dev.	40	0.0002	13	6	0.52

Results for Polymeric Fibers (Type 1 and 2)

Results of three-point bending testing for polymeric fibers are shown in Figure 9. These results are representative for each mixture; Results of experimental analysis on flexural data of polymeric fibers are summarized in Table 11.

Results show that the average elastic flexural stiffness of PolyF9.5_Type1, PolyF5_Type2, and PolyF5_Type1 samples increases by 70, 34, and 27 percent by extending the curing duration from 14 days to 28 days. The maximum flexural load and MOR parameters show similar increases when the curing time is extended. An analysis of the results indicates that average MOR values for PolyF9.5_Type1, PolyF5_Type2, and PolyF5_Type1 samples increase by 13, 24, and 20 percent, respectively. The flexural toughness at 28 days was about double the corresponding value at 14 days for all samples.

Comparing the results for the PolyF5_Type2 and PolyF5_Type1 mixtures at 14 and 28 days indicates that both fiber types have similar effects on flexural toughness, maximum flexural load, and MOR. However, the average flexural stiffness of samples with P-Type1 fiber is 46 and 40 percent higher than corresponding values of samples reinforced with P-Type2 fibers at 14 and 28 days, respectively.

Increasing the dosage of P-Type1 fibers from 5 lb/yd³ to 9.5 lb/yd³ had an inverse effect on all parameters and resulted in a 30 to 50 percent reduction in stiffness, a 30 to 35 percent reduction in maximum flexural load/MOR, and a 10 percent reduction in flexural toughness. The addition of a high volume of fibers can decrease workability, compaction, and flowability of the concrete, resulting in the creation of large pores in the microstructure and lowering the strength of FRC.

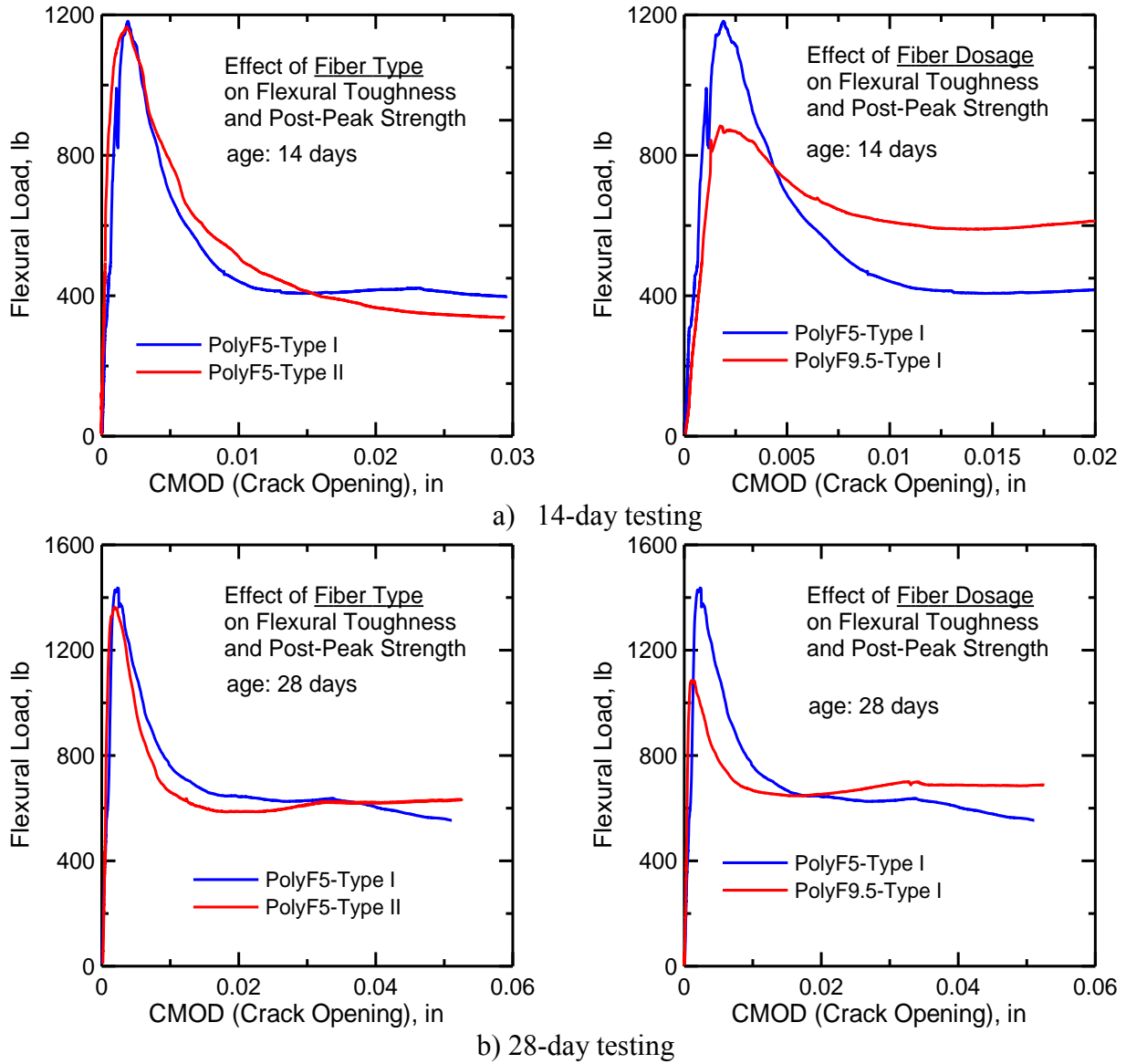


Figure 9. Effect of Polymeric Fibers on Flexural Responses at a) 14 Days and b) 28 Days.

Table 11. Summary of Experimental Analysis on Flexural Data of Polymeric Fibers.

Mix ID	Age, days	Statistical Measure	Elastic Flexural Stiffness, kips/in	Deflection at Max Flexural Load, in	Max Flex. Load, lbf	Modulus of Rupture psi	Flexural Toughness, Lbf-in*
PolyF9.5_Type1	14	Average	351	0.0034	872	427	15.40
		Std. dev.	13	0.0006	17	8	2.49
	28	Average	597	0.0023	983	481	32.86
		Std. dev.	88	0.0004	145	71	0.60
PolyF5_Type2	14	Average	473	0.0036	1,166	571	18.38
		Std. dev.	18	0.0003	62	36	1.86
	28	Average	631	0.0028	1,451	711	31.92
		Std. dev.	197	0.0005	122	60	7.11
PolyF5_Type1	14	Average	690	0.0022	1,247	611	17.47
		Std. dev.	79	0.0005	92	45	0.47
	28	Average	880	0.00255	1,500	734.5	35.95
		Std. dev.	45	0.0002	89	43	1.13

*Toughness measured as the area under the load deflection curve up until a deflection level of 0.1 in

Applications for Shotcrete with using Polymeric Fibers (Type 3) For Early-Age Strength and Ductility

In areas where high early strength and ductility are important, one can develop mixtures that have a rapid rate of strength gain. Examples include pavement repair or shotcrete applications, in which the product must reach its full strength within 7 days of application. In areas of shotcrete application, it is possible to use mixtures with a high dosage of accelerator. In these cases, the early-age strength and ductility of fiber concrete become dominant factors. Applications for shotcrete without any bolt and mesh applications need to consider rapid set times, early-age strength, and ductility development because the fibers are the only mode of reinforcement (Vandewalle, 1993). Early-age strength can be properly designed using chemical admixtures. These are applicable to rapid repair of structures, pavements, slope stability, or rock slide stabilization. Figure 10 shows an application for casting specimens using shotcrete mixtures. The specimens were prepared for testing by flexural and round panel test methods.

Designing FRC requires the use of material properties that are obtained from an experimental program. The test results are used to obtain material property data, which are incorporated in the analytical, empirical, or computer simulation of design cases. The design procedures can be developed based on models for flexural, tension, and compression behavior.



Figure 10. Casting of Shotcrete FRC Samples for Flexural and Compressive Strength Testing.

The objective of this set of experiments was to document the different levels of energy absorption and residual load capacity of FRC tested in accordance with the modified ASTM C1609 procedure. It has been shown that the load in the post-crack range can be influenced by the amount of fibers that offer resistance to crack opening. Methods of structural analysis are being developed to design concrete slabs using the various degrees of strain softening exhibited by the material. Researchers also are developing techniques for designing concrete slabs using plastic analysis. These analytical approaches are also included in the present report.

Results of the three-point bending test for polymeric fibers for two alternative mixtures are shown in Figure 11. Results of the experimental analysis on the flexural data of polymeric fibers are summarized in Table 12.

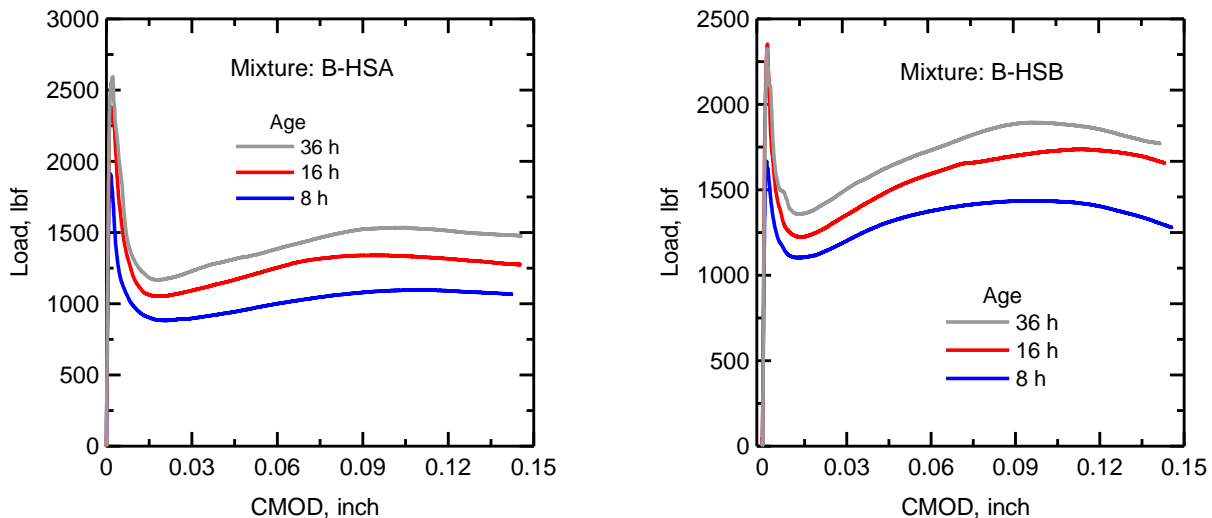


Figure 11. Effect of Polymeric Fibers on Flexural Responses at 8, 16, and 36 Hours.

Results show that the average elastic flexural stiffness of both normal strength samples, B-CSA and B-CSB, increases by 45 percent due to the curing from 8 to 16 hours. While there is no significant change in flexural stiffness of B-CSA samples from 16 to 36 hours, there was a 30 percent increase in this parameter for B-CSB samples. No significant change in elastic flexural

stiffness was observed for the high strength mixtures, B-HSA and B-HSB. There is no clear trend for the change of deflection at maximum load for different mixtures by increasing the curing from 8 to 16 hours, or from 16 to 36 hours. While this parameter increased by 11 to 17 percent for B-CSA mixture, it decreased by 7 to 12 percent for B-CSB samples and increased 17 to 60 percent for B-HSA samples.

Table 12. Summary of Experimental Analysis on Flexural Data of Polymeric Fibers.

Sample Code	Age, hr	Statistical Measure	Elastic Flexural Stiffness, kips/in	Deflection at Max Flexural Load, in	CMOD at Max Flexural Load, in	Max Flex. Load, lbf	MOR, psi	Flexural Toughness, lbf in
B-CSA	8	Average	1,008	0.0017	0.0017	1,268	228	71.2
		Std. dev.	201	0.0002	0.0003	171	31	0.42
	16	Average	1,558	0.0018	0.0016	2,292	413	108.7
		Std. dev.	66	0.0002	0.0002	160	29	3.68
	36	Average	1,465	0.0020	0.0017	2,482	447	129.2
		Std. dev.	34	0.0001	0.0002	107	19	6.15
B-CSB	8	Average	1,377	0.0016	0.0016	1,637	295	92.5
		Std. dev.	162	0.0004	0.0003	13	2	2.54
	16	Average	1,533	0.0019	0.0018	2,127	383	116.2
		Std. dev.	87	0.0002	0.0002	191	34	0.49
	36	Average	1,997	0.0015	0.0019	2,486	448	112.1
		Std. dev.	254	0.0005	0.0004	23	4	12.02
B-HSA	8	Average	1,670	0.0013	0.0013	1,707	307	74.8
		Std. dev.	458	0.0001	0.0002	288	52	0.71
	16	Average	1,810	0.0019	0.0017	2,446	440	126.8
		Std. dev.	121	0.0003	0.0001	88	16	30.40
	36	Average	1,778	0.0022	0.0019	2,620	472	123.6
		Std. dev.	234	0.0002	0.0006	37	7	17.6
B-HSB	8	Average	1,818	0.0013	0.0015	1,598	288	106.2
		Std. dev.	411	7.07E-05	7.07E-05	97	18	13.43
	16	Average	1,572	0.0020	0.0018	2,288	412	122.4
		Std. dev.	34	0.0000	0.0000	91	16	22.06
	36	Average	1,724	0.0019	0.0017	2,476	446	135.7
		Std. dev.	143	0.0002	7.07E-05	214	39	13.08

Comparing the results for different mixtures at 8, 16, and 36 hours indicates that increasing the curing time has a proportional effect on flexural toughness and maximum flexural load/MOR parameters, especially for curing between 8 to 16 hours. The toughness from 8 to 16 hours increased by 80, 20, 65, and 28 percent for the B-CSA, B-CSB, B-HSA, and B-HSB samples, respectively. From 16 to 36 hours, the toughness increased only 18 and 11 percent for the B-CSA and B-HSB samples, while it decreased slightly for the B-CSB and B-HAS samples. The increase in maximum flexural load/MOR from 8 to 16 hours was 95, 50, 53, and 55 percent for the B-CSA, B-CSB, B-HSA, and B-HSB samples, respectively. The increase was much lower from 16 to 36 hours, indicating that due to the addition of accelerator admixtures, the mixtures

gained early strength rapidly during the first 16 hours, after which time the rate of strength increase slowed significantly.

Results for the B-CSA and B-CSB mixtures show that increasing the fiber dosage from 10 lb/yd³ to 12 lb/yd³ leads to a 30 percent increase in elastic flexural stiffness, maximum flexural load/MOR parameters, and flexural toughness after 8 hours. However, at 16 and 36 hours, the results for these two mixtures are similar. In the high-strength mixtures, B-HSA and B-HSB, increasing the fiber dosage from 10 lb/yd³ to 15 lb/yd³ results in a decrease in all parameters at all ages. The only exceptions are flexural stiffness and flexural toughness, which increased by 8 and 42 percent at 8 hours, respectively. This result may be attributable to the addition of a high volume of fibers to the mixtures, which could decrease workability and flowability of the concrete. This could then result in increasingly large pores and a decrease in the FRC strength. These results show the importance of using adequate, but not excessive, amounts of fibers to obtain a high-performance FRC.

Results for Polymeric Fibers (Type 2, 3, 4, and 5)

The previous section examined only one type of polymeric fiber (P-Type3). This section examines a similar mixture of concrete reinforced with different polymeric fibers. The results of three-point bending tests for all of the fibers are shown in Figure 12. A summary of the experimental analysis for all flexural data is shown in Table 13.

Average flexural stiffness of mix 1 with P-Type 3 fibers is 17, 12, 5, and 6 percent higher than mixes 2, 3, 4, and 5 with other types of fibers, respectively. Mix 1 reinforced with P-Type 3, and mix 3 reinforced with P-Type 4, have the highest maximum flexural load/MOR. The flexural toughness of mix 1 with P-Type3 fibers is 65, 29, 15, and 13 percent higher than that of mixes 2, 3, 4, and 5, respectively.

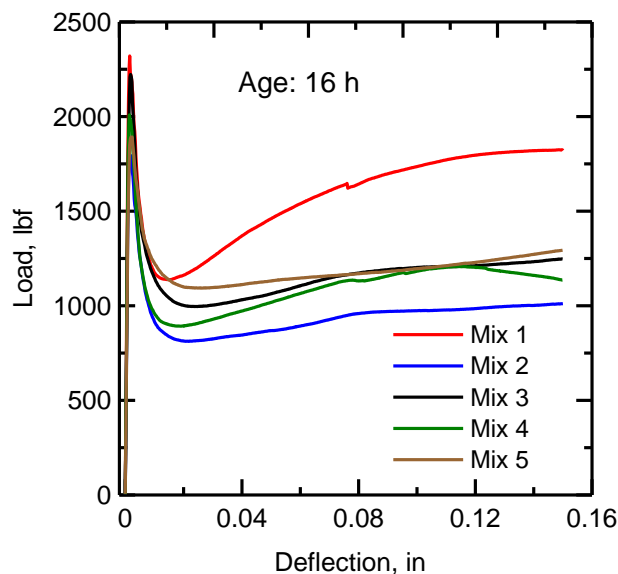


Figure 12. Effect of Different Polymeric Fibers on the Flexural Response at 16 Hours.

Table 13. Summary of Experimental Analysis of Polymeric Fibers (Types 2, 3, 4 and 5).

Mix No.	Statistics	Stiffness, kips/in	Defl. at Max Load, in	CMOD at Max Load, in	Max. Load, lb	Modulus of Rupture psi	Defl. Capacity, in	CMOD Capacity, in	Flex. Tough., lbf.in
Mix 1	Average	1,603	0.0017	0.0017	2,228	401	0.0884	0.1506	139.72
	Std. Dev.	32	0.0001	0.0002	129	23	0.0379	0.0667	73.31
Mix 2	Average	1,367	0.0018	0.0018	1,958	352	0.0900	0.1508	84.74
	Std. Dev.	88	0.0001	0.0000	225	41	0.0030	0.0005	1.83
Mix 3	Average	1,434	0.0019	0.0018	2,241	404	0.0932	0.1502	108.47
	Std. Dev.	159	0.0003	0.0003	11	2	0.026	0.0395	28.34
Mix 4	Average	1,534	0.0018	0.0024	1,992	359	0.0858	0.1504	121.89
	Std. Dev.	466	0.0001	0.0012	47	9	0.021	0.0005	61.74
Mix 5	Average	1,517	0.0022	0.0020	1,836	331	0.0942	0.1501	124.02
	Std. Dev.	166	0.0002	7.07E-05	91	16	0.019	7.07E-05	15.93

INVERSE ANALYSIS OF LOAD-DEFLECTION RESPONSE

The researchers have done extensive work in the development, design, analysis, and fieldwork with FRC (Soranakom & Mobasher, 2007a; Soranakom & Mobasher, 2007b; Soranakom & Mobasher, 2008). Traditionally, the compressive strength is a major design parameter in the design of reinforced concrete structures. However, not all loading cases, applications, and specifications translate directly into the compressive strength values. Accordingly, tensile response has a dominant effect on the performance of FRC materials. Therefore, compressive strength cannot be used as the sole measure of structural analysis, design, quality, and performance. By using the design methodology in this section, the transportation community can realize the potential for the use of fibers in improving ductility in tensile regions, which refers to the zone below the neutral axis in a flexural beam. This work has culminated in a series of formulations for simplified design and analysis procedures, incorporating the reliable stress-strain relationship based on material behavior. ACI is considering several publications in this area (such as ACI 544) as guides for use in designing FRC.

Figure 13 shows the bilinear elastic plastic model in compression and tension for an FRC material. The tension and compressive stress and strain are both linear in the elastic range until the first cracking strain, ϵ_{cr} , is reached. Since the compressive strength is higher than tensile strength, a non-dimensional parameter $\omega > 1$ is defined as the ratio of compressive to tensile strength, and thus, $\epsilon_{cy} = \omega \epsilon_{cr}$. After tensile cracking, the load-carrying capacity drops to a constant level defined by $\mu E \epsilon_{cr}$. Two main parameters are therefore Young's Modulus, E , and the first cracking strain in tension, ϵ_{cr} . The following normalized parameters define the characteristics of the stress-strain curve:

- Compressive strain to tensile strain ratio at failure, $\omega = \epsilon_{cy} / \epsilon_{cr}$.
- Tensile strain capacity, α and β_{tu} .

- Compressive strain capacity, λ_{cu} .
- Strain softening stiffness coefficient, $-\infty < \eta < 0$.
- Stiffness ratio, $\gamma = E_c / E$.

α represents the strain in the descending branch of stress after the cracking. By setting the parameter $\alpha=1$ and η as an extremely small number, one can obtain the strain-softening parameters from this model. The behavior of a specimen under flexure is dominated by the cracking that initiates at the notch and grows along the depth of the specimen. As such a test progresses, the deformation localizes at the notch due to crack propagation. The stress transmitted through the cracked faces of sample is the tensile stress that is simplified as a constant stress measure and depends on a parameter $0 < \mu < 1$, represented as a fraction of tensile strength. For example, $\mu = 0.3$ indicates that the tensile post-cracking load-carrying capacity is limited to 30 percent of the tensile strength of the specimen. Figure 14 shows the simplified strain and stress variation along a cross section.

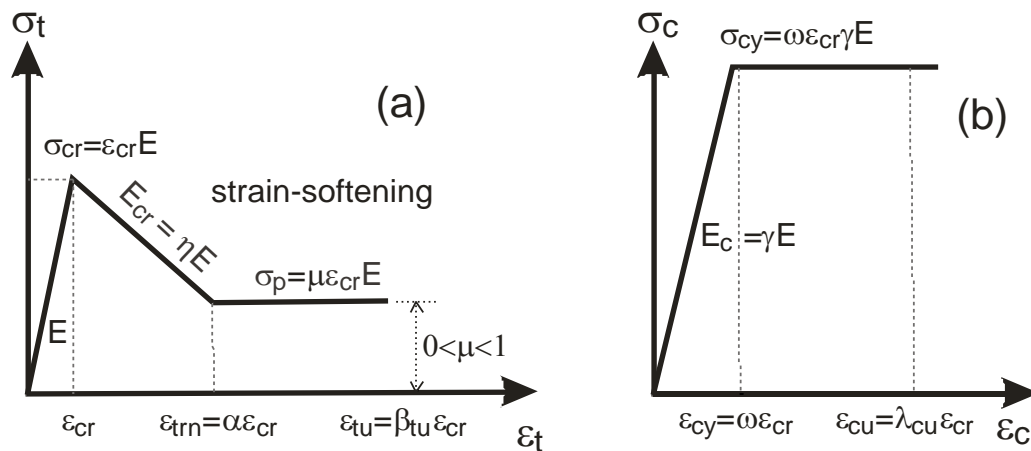


Figure 13. Stress-strain Material Model for FRC Strain Softening Materials: (a) Tension Model and (b) Compression Model.

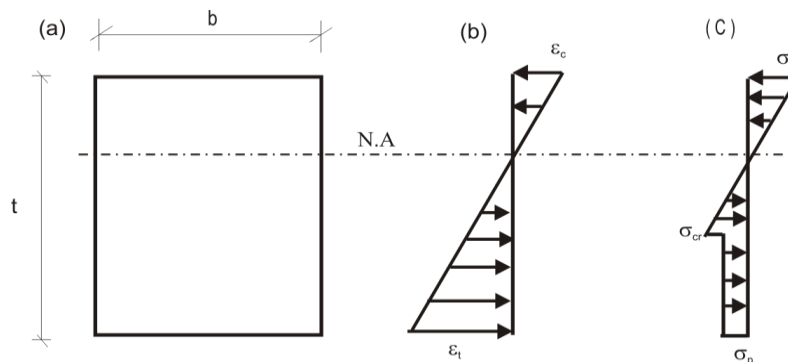


Figure 14. Rectangular FRC Section and the Simplified Strain and Stress Variations in Bending (Soranakom & Mobasher, 2007b).

Closed form solutions for the moment-curvature response were derived explicitly and published recently (Mobasher, 2011). The procedure first identifies the potential interaction of parameters and defining the stress-strain response according to the applied normalized maximum compressive strain, λ , in three stages: elastic tension and compression ($0 < \lambda \leq 1$ and $0 < \beta \leq 1$), post-peak tension-elastic compression ($1 < \beta$, $1 < \lambda \leq \omega$), and post-peak tension-plastic compression ($1 < \beta$ and $\omega < \lambda \leq \lambda_{cu}$). The neutral axis depth ratio, k , is found by solving equilibrium of forces. The moment capacity is then calculated from the tension and compression forces and the neutral axis location; the corresponding curvature is obtained by dividing the maximum compressive strain with the neutral axis depth. Finally, the moment, M , and curvature, ϕ , are expressed in terms of the cracking moment and curvature, M_{cr} and ϕ_{cr} , respectively, and their dimensionless parameters, M' and ϕ' . Expressions for calculating neutral axis depth ratio, k , moment, and curvature are obtained as follows.

For a given set of material parameters and beam dimensions (b and d are the width and the height of the beam), the moment-curvature response can be generated by substituting any value of normalized maximum tensile strain, β , from zero up to the ultimate tensile strain, β_{cu} . The model presented in Figure 15 represents the derivations for moment-curvature responses of both a stress-softening and strain-hardening material with different tensile and compressive responses. For example, in the case where the tension response is in strain-softening mode while the compression response is still elastic, one can calculate the location of k , the moment capacity, and curvature. k is found by solving the equilibrium of net internal forces equal to zero:

$$k = \frac{C_1 - \sqrt{\beta^2 C_1}}{C_1 - \beta^2}; \text{ where } C_1 = \eta(\beta^2 - 2\beta + 1) + 2\beta - 1 \quad (\text{Eq. 1})$$

The nominal moment capacity, M_n , is obtained by taking the first moment of force about the neutral axis, $M_n = F_{c1}y_{c1} + F_{t1}y_{t1} + F_{t2}y_{t2}$, and expressed as a product of the normalized nominal moment, m' , and the cracking moment, M_{cr} , as follows:

$$M_n = m' M_{cr} \quad M_{cr} = \frac{\sigma_{cr} b h^2}{6} \quad (\text{Eq. 2})$$

$$m' = C_2 \frac{k^2 - 2k + 1}{\beta^2} + \frac{2\beta k^3}{1 - k} \text{ where } C_2 = C_1 + 2C_1\beta - \beta^2 \quad (\text{Eq. 3})$$

$$M_{cr} = \frac{\sigma_{cr} b h^2}{6} \quad (\text{Eq. 4})$$

$$\phi = \phi' \phi_{cr} \quad \phi_{cr} = \frac{2\varepsilon_{cr}}{d} \quad (\text{Eq. 5})$$

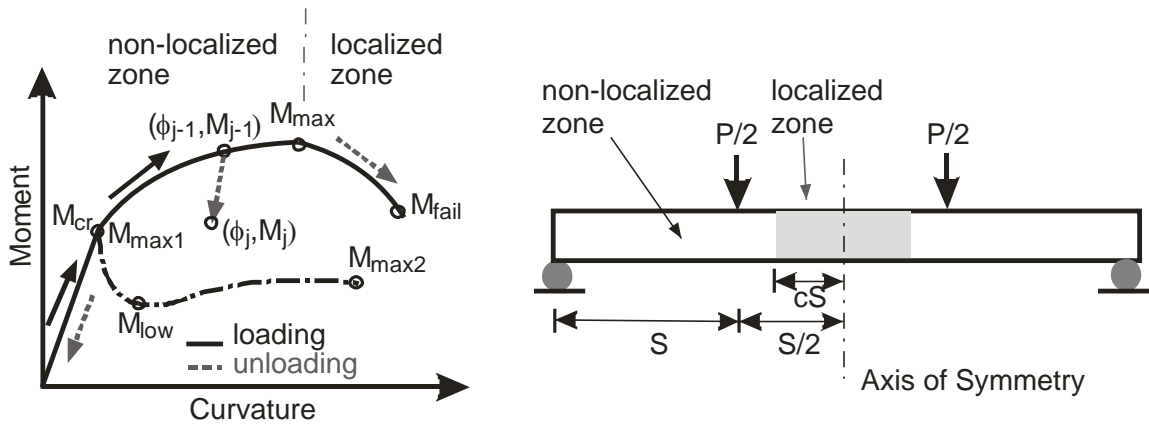


Figure 15. Closed-form Moment Curvature Relationship (for Tensile Strain-softening and Hardening Response) and Applied for Calculation of Load Deflection of the Flexural Beam (Mobasher, 2011).

The methodology used in the design of conventional reinforced concrete according to ACI 318 is adopted next (ACI Committee 318, 2005). The nominal moment capacity of a flexural member, M_n , must be decreased by a reduction factor to account for variability in materials and workmanships. The reduced capacity must be greater than the ultimate moment, M_u , due to factored loading:

$$\phi_r M_n \geq M_u \quad (\text{Eq. 6})$$

where ϕ_r is the reduction factor for strain-softening FRC and taken within the range of 0.7 to 0.85, equal to the reduction factor for compressive failure of plain concrete stipulated by ACI 318. Despite the fact that post-crack flexural response of FRC is ductile such that it can sustain large deflections after cracking, it may fail abruptly with little warning after passing the ultimate moment. For this reason, a conservative reduction factor for compressive failure is adopted. One can show that the post-crack normalized moment curvature response depends mainly on the normalized post-crack tensile strength parameter, μ . The moment-curvature response becomes elastic-perfectly plastic when μ reaches the critical value of μ_{crit} , given by:

$$\mu_{crit} = \frac{\omega}{3\omega - 1} \quad (\text{Eq. 7})$$

μ_{crit} represents the transition from a deflection-softening to a deflection-hardening material. For typical steel fiber-reinforced concrete (SFRC) with ω between 6 and 12, μ_{crit} varies in a narrow range from 0.353 to 0.343. This indicates that the post-crack tensile strength in FRC must be at least 35 percent of its tensile strength before it can exhibit deflection hardening. This value is in agreement with the values reported by other researchers (Nemegeer-Harelbeke, 1998; Barros et al., 2005).

Back-calculation of Material Properties from Flexural Tests

This section introduces a theoretical method to utilize the load deflection results of flexural specimens for obtaining tensile material properties. This section also presents a comparison of the material properties with the available ASTM approaches. By utilizing the back-calculation procedure, the researchers sought to determine equivalent material properties used in the procedures proposed in calculation for moment curvature and load deflection. This approach forms the basis for the development of design equations for various structural elements.

Due to the lack of a comprehensive testing program prior to the design and construction phase, many material properties used in current design procedures are estimated based on relationships with uniaxial compressive strength, f'_c . This may not be a realistic approach to capture the mechanisms of tensile failure using compressive strength properties; hence, new procedures are needed. Several test methods are available to characterize post-crack tensile strength of FRC. Gopalaratnam addressed the experimental and analytical merits and drawbacks of these methods (Gopalaratnam, 1995).

In the conventional approach, material properties are estimated based on prior experience and verified through testing. As samples are tested to meet the specified strength in design calculations, the strength of a flexural member is correlated empirically with its compressive and tensile strength, and then verified during the construction quality control phase. Other test methods developed for the characterization of ductility and toughness may be applicable to differentiate in-between various comparative samples; however, their utility for design purposes are questionable. It would be ideal to obtain fundamental tensile properties from flexural tests, but it is imperative that the discrepancy between the two be addressed in design calculations and actual values obtained from testing be subjected to appropriate safety factors.

To verify the theoretical derivations for flexural loading, the researchers studied the model applied to FRC beams under several cases of deflection-softening and deflection-hardening under the three-point and four-point bending tests, for which tensile data may not have been available. The closed-form solutions for moment-curvature diagrams can be used to predict load deformation response and can be followed through a back-calculation procedure to measure material properties from flexural tests. The researchers found the material parameters for tension models by fitting the model to simulate the flexural response. If tension results are available, one can use a forward calculation to predict the flexural response. If such results are not available, one can use the flexural data to obtain effective tensile properties. Since the material parameters for compression model are less dominant in the prediction of the load deflection, they can be estimated from the uniaxial compressive strength or tensile data. To capture the post-peak response, especially in low-volume fraction composites, tests need to be conducted under closed-loop control with the CMOD as the controlled variable. In this test, the CMOD is measured across the face of the notch using an extensometer. The loading procedure also measures the fracture toughness parameter, G_f , defined as the area under the load-deflection response.

Representative back-calculations of stress-strain responses using a plasticity model for AR glass fibers are shown in Figure 16 and compared with control experiments in Figure 17. Back-

calculated tensile parameters of flexural samples using the plasticity model are shown in Table 14.

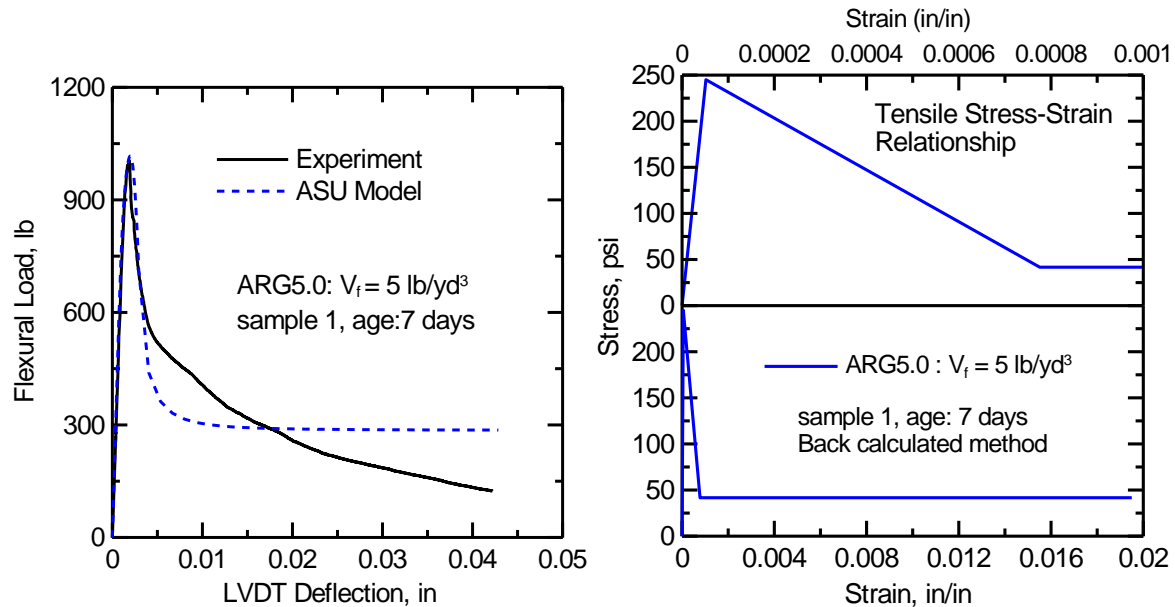


Figure 16. a) Experimental Results and Simulated Flexural Load-deflection Response of Concrete with Glass Fibers b) Back-calculated Stress-Strain Relationship for a Control Sample at 7 Days.

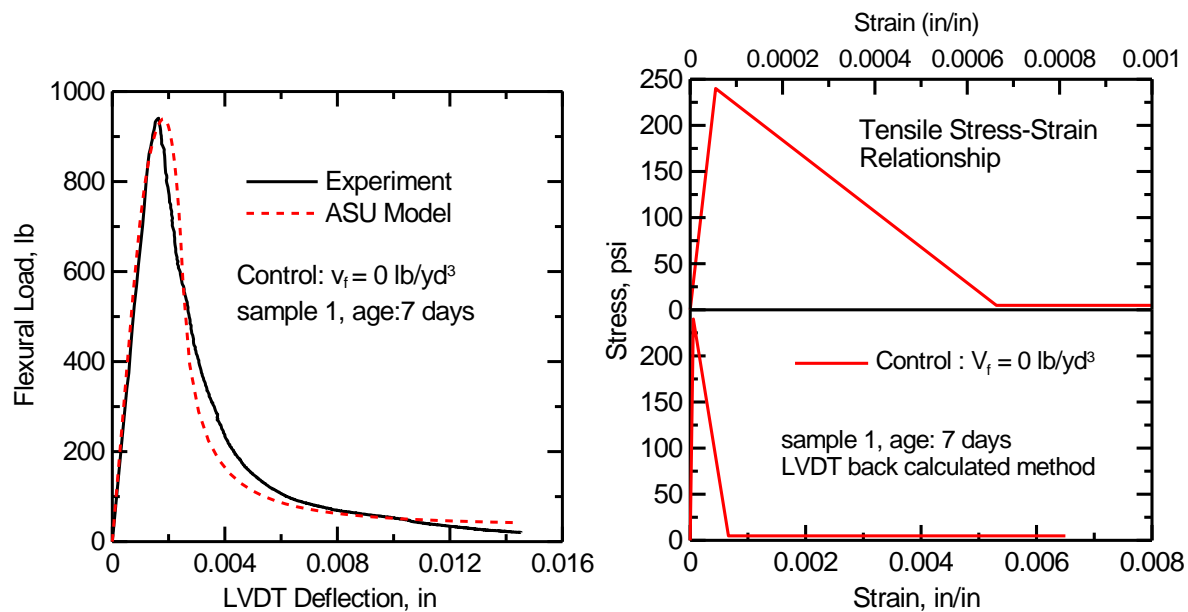


Figure 17. a) Experimental Results and Simulated Flexural Load-deflection Response and b) Back-calculated Stress-Strain Relationship for a Control Sample at 7 Days.

Table 14. Back-calculated Tensile Parameters of Flexural Samples Using a Plasticity Model.

Mix ID	Sample Code	Age, days	First Crack Tensile Strain (ϵ_{cr}), μstr	Young's Modulus (E), ksi	First Crack Tensile Strength (σ_{cr}), psi	Normalized Post-Crack Tensile Strength (μ)	Normalized Transition Tensile Strain (α)	Transition Tensile Strain, (ϵ_{trn}), μstr	Ultimate Tensile Strain (ϵ_{tu}), μstr
Plain	Plain_WC.55_1d_1	1	56	3,949	220	0.02	7	389	6,631
	Plain_WC.55_1d_2	1	57	3,668	210	0.02	7	400	6,001
	Plain_WC.55_1d_3	1	58	3,949	230	0.02	6	349	6,998
	Average	1	57	3,855	220	0.02	7	379	6,543
	Plain_WC.55_3d_1	3	54	4,344	235	0.02	12	649	7,001
	Plain_WC.55_3d_2	3	62	3,949	245	0.02	9	558	6,998
	Average	3	58	4,147	240	0.02	11	604	6,999
	Plain_WC.55_7d_1	7	55	4,344	240	0.02	12	663	6,497
	Plain_WC.55_7d_2	7	57	4,344	245	0.02	12	682	7,500
Average	7	56	4,344	243	0.02	12	672.5	6,999	
GlassF5	GlassF5_WC.55_1d_	1	57	3,949	225	0.20	7	399	17,999
	GlassF5_WC.55_1d_	1	60	3,949	235	0.17	7	417	18,002
	GlassF5_WC.55_1d_	1	54	3,949	215	0.22	7	382	18,999
	Average	1	57	3,949	225	0.20	7	399	18,333
	GlassF5_WC.55_3d_	3	50	4,739	238	0.24	12	603	8,999*
	GlassF5_WC.55_3d_	3	53	4,739	250	0.17	12	633	19,496
	Average	3	51	4,739	244	0.21	12	618	19,496
	GlassF5_WC.55_7d_	7	52	4,739	245	0.17	15	775	19,501
	GlassF5_WC.55_7d_	7	52	4,739	245	0.17	15	775	19,000
Average	7	52	4,739	245	0.17	15	775	19,250	

* Ultimate tensile strain of this sample is back-calculated only up to 0.02 in, where the LVDT stopped recording

Inverse Analysis of Load Deflection Response of Polymeric Fibers (Type 1 and 2)

Representative back-calculations of stress-strain responses using the bilinear elastic-plastic model for polymeric fibers are shown in Figure 18. Back-calculated tensile parameters of flexural samples using the model are also shown in Table 15.

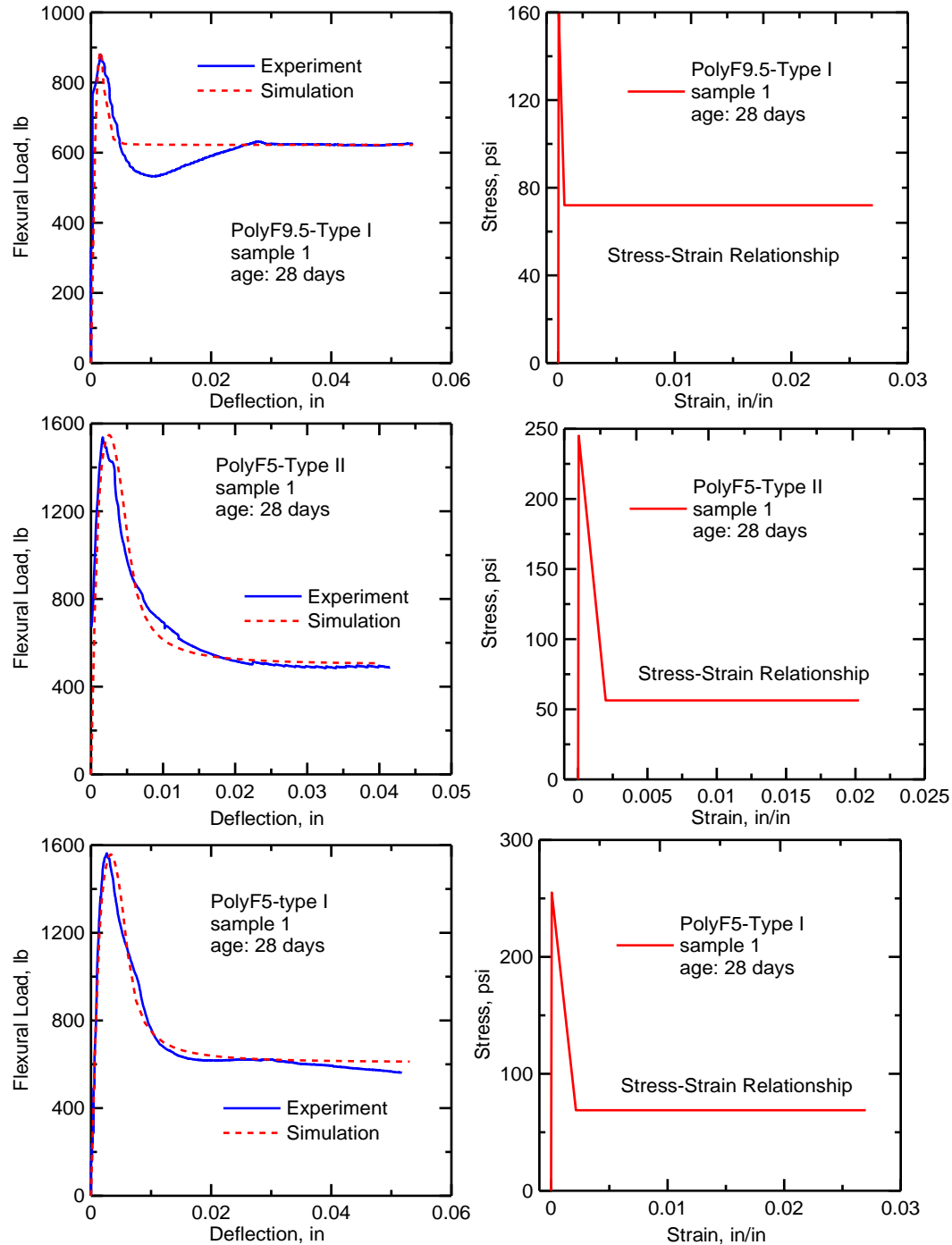


Figure 18. Experimental and Simulated Load-deflection Response and Back-calculated Stress-Strain Relationship of Three Samples with Different Fiber Types and Contents Tested at 28 Days.

Table 15. Back-calculated Tensile Parameters of Flexural Samples Using the Strain-softening Model.

Mix ID	Sample Code	Age, days	First Crack Tensile Strain (ϵ_{cr}), μstr	Young's Modulus (E), ksi	First Crack Tensile Strength (σ_{cr}), psi	Normalized Post-Crack Tensile Strength (μ)	Normalized Transition Tensile Strain (α)	Transition Tensile Strain, (ϵ_{trn}), μstr	Ultimate Tensile Strain (ϵ_{tu}), μstr
PolyF9.5_Type1	PolyF9.5_Type1_14d_1	14	102	1,622	165*	0.39	12	1,224	20,308
	PolyF9.5_Type1_14d_2	14	96	1,622	155*	0.43	16	1,536	20,352
	Average	14	99	1,622	160	0.41	14	1,380	20,330
	PolyF9.5_Type1_28d_1	28	44	3,605	160*	0.45	12	528	26,765
	PolyF9.5_Type1_28d_2	28	44	4,326	190*	0.43	16	704	20,288
	Average	28	44	3,965.5	175	0.44	14	616	23,526
PolyF5_Type2	PolyF5_Type2_14d_1	14	48	3,824	185	0.2	50	2,400	20,088
	Average	14	48	3,824	185	0.2	50	2,400	20,088
	PolyF5_Type2_28d_1	28	44	5,544	245	0.23	45	1,980	20,161
	PolyF5_Type2_28d_2	28	58	3,824	220	0.30	40	2,320	25,201
	Average	28	51	4,684	233	0.265	42.5	2,150	22,681
PolyF5_Type1	PolyF5_Type1_14d_1	14	71	2,868	205	0.20	32	2,272	20,114
	PolyF5_Type1_14d_2	14	52	3,824	200	0.23	25	1,300	20,129
	Average	14	62	3,346	203	0.22	29	1,786	20,122
	PolyF5_Type1_28d_1	28	67	3,824	255	0.27	32	2,144	27,128
	PolyF5_Type1_28d_2	28	75	3,250	245	0.29	25	1,875	25,867
	Average	28	71	3,537	250	0.28	29	2,010	26,498

Note that the present approach can reliably simulate the response of the specimens for different fiber contents. The bilinear elastic-plastic model presented here as a design approach captures the location of the neutral axis, the linear compressive stress, and the residual tensile stress.

DATA REDUCTION BY AVERAGE RESIDUAL STRENGTH METHOD (ARS)

ASTM test methods C1399 and C1609 present alternative ways to measure the post-cracking characteristics of FRC and report the results in terms of ARS values. The popularity of ASTM C1399 is due to the fact that the experimental portion of the test can be accomplished using an open-loop testing machine that is available in many material testing labs (Nemkumar & Ashish, 1999; Nemkumar & Ashish, 2000; ASTM, 1999a). According to the ASTM C1399 method, first a steel plate is placed underneath a concrete beam and the specimen is loaded under a four-point bending setup until the concrete cracks. Then, the steel plate is removed and the cracked specimen is reloaded to obtain post-crack flexural strengths at deflection levels of 0.02, 0.03, 0.04, and 0.05 inches. Finally, the equivalent stress results are averaged to represent an ARS value. This parameter has been used to compare different material formulations, but some designers have been using it as a tensile strength measure. It is imperative to note that the ARS value is not an equivalent elastic stress and cannot be associated with the post-crack tensile strength, or with the tensile residual strength parameter. The ARS method has been extended to ASTM C1609 (ASTM, 1999b). As the post-peak response is averaged, the residual load is used in the elastically equivalent flexural stress using the section modulus of the uncracked beam to calculate a stress measure. In doing so, the load is divided by the equivalent elastic section modulus. The ARS value is reported as an equivalent elastic stress in a specimen that is no longer elastic. The properties are measured in accordance with a flexural neutral axis assumed at the centroid of the specimen, whereas due to cracking the neutral axis has shifted significantly toward the compression zone. The ARS method therefore overestimates the residual uniaxial tensile strength obtained based on the present approach.

To illustrate the fundamental differences between the two methods, the stress distribution during the late stage of loading composites is presented across the depth of the cross section. The strain distribution across the cross section is shown in Figure 19. Note that, according to the ARS method, the stress distribution is linear and the neutral axis remains at the center of the section. However, in accordance with the bilinear elastic plastic model (also called the bilinear softening model), the neutral axis moves toward the compression zone and a uniform tensile stress distribution is distributed over the tensile zone. Figure 19 implies that the residual flexural strength cannot be a substitute for residual tensile strength in design, since the residual flexural strength is just an equivalent form of stress and not a material property.

COMPARISON BETWEEN POST-PEAK RESIDUAL STRENGTH AND ARS METHOD

Direct correlation of residual strength from ASTM C1399 and the bilinear elastic-plastic method, shown in Figure 20, indicates that the ARS method overestimates the residual tensile strength by as much as two to three times. The experimental test data were reduced using both methods, and the plot of residual strength in accordance to ARS values was plotted vs. the post peak residual strength obtained by the bilinear elastic-plastic method. The simplifications due to the assumption of the location of neutral axis lead to very high nominal flexural stress levels in the

far tension fiber, which are far greater than the actual tensile strength. Extreme caution must be exercised in applying the ARS method to design and analysis of FRC sections. In fact, the ARS parameter is merely an equivalent elastic stress of the true nonlinear stress of the material. Thus, this parameter can serve only as a residual tensile strength index.

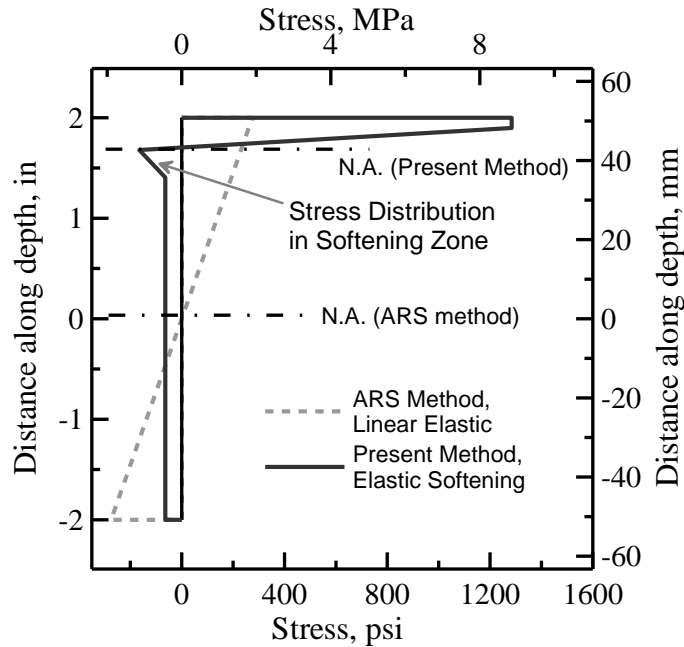


Figure 19. Comparison of Stress Distribution Determined Using the Present Approach and the ARS Method.

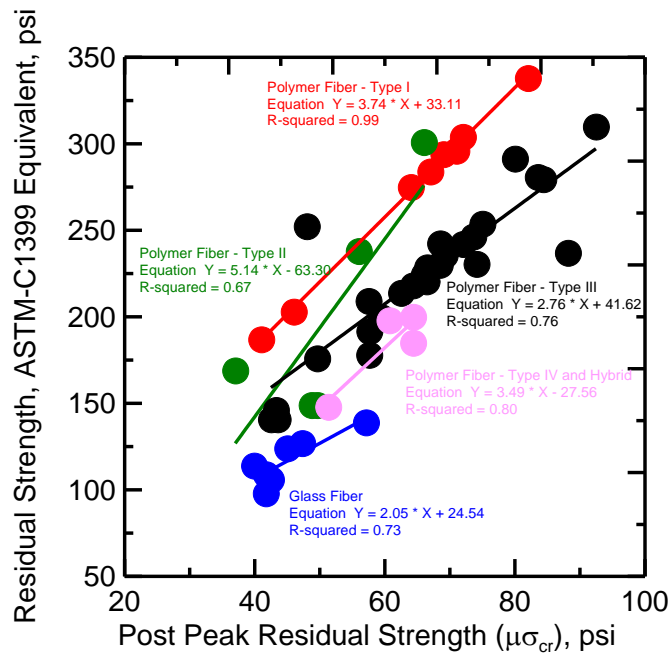


Figure 20. Comparison of Post-peak Strength with ARS for Various Types of Fibers.

DEVELOPMENT OF DESIGN EQUATIONS FOR FLEXURAL RESPONSE

A tensile stress-strain model also can be obtained directly from a uniaxial tension test. However, the test procedure is difficult to control and normally underestimates the flexural strength due to the size effect between uniform stress in direct tension tests and gradient stress in bending tests (Soranakom & Mobasher, 2007a; Soranakom & Mobasher, 2007b). To predict flexural behaviors, the back-calculation of tensile properties from the load-deflection curve of the four-point bending test is an option that indirectly incorporates the size effect in material properties. The design equations for flexural response are presented here with a minimum number of independent variables and dimensionless parameters. Cracking tensile strength and Young's modulus can be estimated according to ACI 318 (American Concrete Institute, 2005):

$$\sigma_{cr} = E\varepsilon_{cr} = 6.7\sqrt{f'_c} \quad (\text{psi}) \quad (\text{or} = 0.56\sqrt{f'_c} \quad (\text{MPa})) \quad (\text{Eq. 8})$$

$$E = 57,000\sqrt{f'_c} \quad (\text{psi}) \quad (\text{or} = 4,733\sqrt{f'_c} \quad (\text{MPa})) \quad (\text{Eq. 9})$$

Cracking tensile strain for FRC members can be calculated from Hooke's law as:

$$\varepsilon_{cr} = \frac{\sigma_{cr}}{E} = \frac{6.7\sqrt{f'_c}}{57000\sqrt{f'_c}} = \frac{0.56\sqrt{f'_c}}{4733\sqrt{f'_c}} = 118 \mu\text{str} \quad (\text{Eq. 10})$$

The yield compressive strength parameter, $\sigma_{cy} = 0.85f'_c$ from RILEM, is adopted here, in which f'_c is the ultimate uniaxial cylinder compressive strength (RILEM Technical Committee 162-TDF, 2003). Using the compressive strength as an input, the parameter ω is defined as the ratio of compressive strength to tensile strength and was reported in Tables 14 and 15. Applying the ACI-recommended equations for compressive and tensile strength, this function can be estimated as $\omega = 0.85(f'_c)^{0.5}/6.7$. By defining the initial cracking moment, $M_{cr} = \sigma_{cr}bh^2/6$, and the resistance factor defined in accordance with load and resistance factor design (LRFD) guidelines as ϕ_p , the expression for factored nominal moment capacity as an elastic material is shown in Figure 13. The moment capacity using an elastic-residual strength approach is represented by a function that utilizes the post-crack tensile strength, μ , and ultimate compressive strength, f'_c , is represented by Equation 12 (Chuang & Mai, 1989; Wee, Lu & Swaddiwudhipong, 2000):

$$\phi_p M_n = \frac{1}{6} \phi_p \sigma_{cr} b h^2 \quad (\text{elastic analysis}) \quad (\text{Eq. 11})$$

$$\phi_p M_n = \left[\frac{\mu \sqrt{f'_c}}{\xi \mu + 2 \sqrt{f'_c}} \right] \phi_p \sigma_{cr} b h^2 \quad \xi = 15.8 \text{ for } f'_c \text{ in psi, } \xi = 1.32 \text{ for } f'_c \text{ in MPa} \quad (\text{Eq. 12})$$

MINIMUM FLEXURAL POST-CRACK TENSILE STRENGTH REQUIREMENTS

In reinforced concrete structures, the minimum flexural reinforcement is enforced to avoid a sudden failure of a beam when its post-cracking strength is lower than its cracking moment. In an FRC system, the sudden drop in the moment capacity after cracking refers to the deflection-

softening response. The critical normalized post-crack tensile strength level, μ_{crit} , that maintains a load-carrying capacity equivalent to the cracking strength level ($M_u = M_{cr}$) is obtained by solving Equation 4 with a reduction factor $\phi_p = 1$.

$$\mu_{crit} = \frac{\omega}{3\omega - 1} \quad (\text{Eq. 13})$$

For typical FRC materials, the compressive-tensile strain ratio, ω , varies between 6 and 12. Thus, μ_{crit} varies in a narrow range between 0.34 and 0.35. Since the actual tensile strength and the strength used in the design calculations may be different by a factor of $7.5\sqrt{f'_c} / 6.7\sqrt{f'_c} = 1.12$, a slightly conservative value that ensures the post-crack capacity is always greater than the first cracking level of an actual flexural member is proposed as:

$$\mu_{min_flex} = 0.40 \quad (\text{Eq. 14})$$

MINIMUM POST-CRACK TENSILE STRENGTH FOR SHRINKAGE AND TEMPERATURE

Due to temperature and shrinkage conditions occurring during the curing process, a concrete slab with a large surface-to-volume ratio can be subjected to severe cracking due to restrained shrinkage stresses. To control crack width, minimum reinforcement for shrinkage and temperature must be placed perpendicular to the main flexural reinforcement. According to ACI 318, the minimum ratio of reinforcement to gross section area, ρ_{min_ST} , is:

$$\rho_{min_ST} = \begin{cases} 0.0020 & 40 \text{ ksi} < f_y < 50 \text{ ksi, deformed bar} \\ 0.0018 & f_y = 60 \text{ ksi, welded-wire fabric (smooth or deformed)} \\ \frac{0.0018 \times 60,000}{f_y} > 0.0014 & f_y > 60 \text{ ksi at } \varepsilon_{sy} = 0.35\% \end{cases} \quad (\text{Eq. 15})$$

where f_y is the yield strength of steel. When steel rebars or welded wire mesh are replaced with FRC, the minimum normalized post-crack tensile strength, μ_{min_ST} , guarantees that the same tensile performance can be determined by the equivalent tensile capacity for the same reliability index.

$$\phi_b \rho_{min_ST} f_y b h = \phi_p \mu_{min_ST} \sigma_{cr} b h \quad (\text{Eq. 16})$$

Here we can assume a reduction factor identical to the one mentioned in ACI 318 for bending structural members ($\phi_b = 0.90$). In these members, failure is controlled by reinforcement failure. On the other hand, the reduction factor $\phi_p = 0.70$ is used for a member in which the tensile failure is controlled by the post-crack capacity of the FRC. The use of higher and lower reduction factors in Equation 3.16 ensures the reliability index is maintained when the steel reinforcement is replaced with FRC. Conservative values of $\rho_{min_ST} = 0.0018$ and $f_y = 60,000$ psi are substituted

in Equation 16 to produce highest tension force and solve for μ_{min_ST} :

$$\mu_{min_ST} = \frac{140}{\sigma_{cr}} \quad (\text{psi}) \quad (\text{or} = \frac{0.97}{\sigma_{cr}} \quad (\text{MPa})) \quad (\text{Eq. 17})$$

DESIGN EXAMPLE FOR SLAB ON GRADE

The design procedure for strain-softening FRC is best suited to thin structural applications, such as slab systems in which the size effect is minimal and the internal forces are relatively low compared to the moment capacity. An example of slab on grade is presented to demonstrate the design calculations. Typically, slabs on grade are designed based on minimum shrinkage and temperature steel. Loads on slabs are not critical and are transferred directly to stiff compacted base materials. These slabs are allowed to crack but not disintegrate. Other types of slabs on grade and pavements that are designed based on applied load and subgrade modulus are not studied here.

The concrete slab is 5 inches thick, reinforced at mid-depth with #4 steel rebars placed 18 inches apart on center. The materials used are concrete with a compressive strength of 3,000 psi and steel with a yield strength of 60 ksi. In this analysis, this existing design is replaced with steel fiber reinforced concrete (SFRC) that has a compressive strength of 4,000 psi.

The slab is designed based on a 1-foot strip, and the amount of reinforcement, A_s , is calculated as:

$$A_s = \frac{\pi d^2}{4} \frac{12}{spacing} = \frac{\pi 0.5^2}{4} \frac{12}{18} = 0.131 \frac{\text{in}^2}{\text{ft}} \quad (\text{Eq. 18})$$

The plastic compressive zone is calculated according to the ACI stress block concept:

$$a = \frac{A_s f_y}{0.85 f_c' b} = \frac{0.131 \times 60}{0.85 \times 3 \times 12} = 0.257 \quad (\text{Eq. 19})$$

The factored ultimate moment, M_u , is then equal to the reduced nominal moment capacity, $\phi_b M_n$:

$$\begin{aligned} M_u &= \phi_b M_n = \phi_b A_s f_y \left(d - \frac{a}{2} \right) \\ &= 0.9 \times 0.131 \times 60 \left(2.5 - \frac{0.257}{2} \right) \frac{1}{12} = 1.40 \text{ kips-ft/ft} \end{aligned} \quad (\text{Eq. 20})$$

Equivalent Moment Capacity with SFRC, $f_c' = 4,000$ psi

Calculate the cracking tensile strength of SFRC according to the following equation:

$$\sigma_{cr} = 6.7\sqrt{f_c'} = 6.7\sqrt{4000} = 424 \text{ psi} \quad (\text{Eq. 21})$$

Calculate the cracking moment:

$$M_{cr} = \frac{\sigma_{cr}bh^2}{6} = \frac{424 \times 12 \times 5^2}{6} \frac{1}{12000} = 1.77 \text{ kips-ft/ft} \quad (\text{Eq. 22})$$

Calculate the compressive-tensile strength ratio by:

$$\omega = \frac{\sigma_{cy}}{\sigma_{cr}} = \frac{0.85 \times 4000}{424} = 8.02 \quad (\text{Eq. 23})$$

Determine the normalized post-crack tensile strength as demand and solve for required post-crack residual strength:

$$\mu = \frac{M_u \omega}{3\omega\phi_p M_{cr} - M_u} = \frac{1.40 \times 8.02}{3 \times 8.02 \times 0.7 \times 1.77 - 1.40} = 0.395 \quad (\text{Eq. 24})$$

It can be verified that the reduced nominal moment capacity of the SFRC slab is equal to the ultimate moment determined from the reinforced concrete slab:

$$\phi_p M_n = \left[\frac{\mu\sqrt{f_c'}}{15.8\mu + 2\sqrt{f_c'}} \right] \phi_p \sigma_{cr} bh^2 \quad (\text{Eq. 25})$$

$$= \left[\frac{0.395\sqrt{4000}}{15.8(0.395) + 2\sqrt{4000}} \right] 0.7(424)(12)(5)^2 \frac{1}{12000} = 1.40 \text{ kips-ft/ft} \quad (\text{Eq. 26})$$

However, the required μ must be checked against the minimum post-crack tensile strength for flexure, defined in Equation 13, $\mu_{min_flex} = 0.40$. Thus, use $\mu = 0.40$.

Equivalent Tensile Capacity

Assume plain concrete in the reinforced concrete slab has no residual strength; thus, the amount of reinforcement will be replaced with an SFRC having the same tensile capacity:

$$\phi_b A_s f_y = \phi_p \mu \sigma_{cr} b h \quad (\text{Eq. 27})$$

The post-crack tensile strength is calculated as:

$$\mu = \frac{\phi_b A_s f_y}{\phi_p \sigma_{cr} b h} = \frac{0.9 \times 0.131 \times 60}{0.7 \times 0.424 \times 12 \times 5} = 0.397 \quad (\text{Eq. 28})$$

The minimum normalized post-crack tensile strength for shrinkage and temperature can be calculated by the following equation:

$$\mu_{\min_ST} = \frac{140}{\sigma_{cr}} = \frac{140}{424} = 0.33 \quad (\text{Eq. 29})$$

The calculations in this example point to several potential design approaches. If the goal is to replace the existing reinforced concrete slab with an SFRC system and still have the same performance and reliability index as the original design, the post-crack tensile strength must be 0.40 based on the minimum flexural strength. However, if only shrinkage and temperature cracking are of concern, the required strength can be reduced to 0.33. In this case, a parameter of $\mu = 0.40$ is specified to meet a performance level that is equivalent to the reinforced concrete slab. The specified post-crack tensile strength for material testing must be calculated using the same cracking tensile strength used in the design calculations, which may be different from the actual value obtained from testing. According to the definition in Equation 1, the post-crack tensile strength is:

$$\sigma_p = \mu \sigma_{cr} = 0.40 \times 424 = 170 \text{ psi} \quad (\text{Eq. 30})$$

CONCLUSION

The researchers propose a design guideline for flexural members made of strain-softening FRC. The closed-form solutions have been simplified to a single design equation to estimate flexural strength. The researchers also propose setting the minimum normalized post-crack tensile strength at 0.40 for FRC systems to prevent sudden failure of the beam section after flexural cracking. This value is slightly greater than the critical value of 0.35 that changes the beam response from deflection-softening to deflection-hardening. To meet the serviceability criterion, the crack width, due to shrinkage and temperature, must be kept within an acceptable range. By equalizing the tensile capacity of the minimum reinforcement ratio required by ACI code and the

post-crack tensile strength capacity of the FRC, the minimum normalized post-crack tensile strength should be $140/\sigma_{cr}$. Since FRC is best utilized in slab systems in which flexural stress is relatively low, an example of slab on grade was used to illustrate the calculation steps and specify post-crack tensile strength to be verified in material testing.

CHAPTER 4. INTERNAL CURING

INTRODUCTION

The use of concrete mixtures containing blended cements is becoming commonplace. Most cement manufacturers produce one or more blended cement products, and ready-mix producers generally are comfortable with blending portland cement with one or more mineral admixtures during concrete production. This is practiced commonly for both normal-strength and high-performance concretes (Bentz, 2007). However, due to slower reaction rates, blended cement concretes may have different curing requirements and can exhibit distinct sensitivities to curing conditions (Parrott, 1995; Shattaf, Alshamsi & Swamy, 2001; Bentz, 2002).

Over the past decade, research on internal curing has focused on laboratory measurements of the autogenous deformation of internally cured concrete mixtures (Jensen, 2005). Most reports focus on unrestrained autogenous deformation and fundamental concepts of applications of lightweight aggregates (Kovler & Jensen, 2007), rather than the strength development of lightweight aggregates in hot-weather conditions. Recently, some states (such as Ohio) have begun to consider the beneficial effects of using internal curing (Delatte, Mack & Cleary, 2007). However, more needs to be understood about the practical implications of these materials in order for them to be taken from laboratory concepts to field realities.

Pozzolanic materials such silica fume and fly ashes react with calcium hydroxide, $\text{Ca}(\text{OH})_2$, that is produced by the hydration of portland cement. Because there are different chemical reactions present, the accompanying chemical shrinkage is different from that of portland cement. For example, while portland cement hydration typically is accompanied by a chemical shrinkage on the order of 0.07 mass of water per mass of cement for complete hydration, for fly ash, the same coefficient is on the order of 0.10 to 0.16 (Bentz & Garboczi, 1991). This means that if and when these mineral admixtures react completely in a blended cement system, their demand for curing water can be much greater than that in a conventional portland cement concrete. When this water is not readily available, because of the emptying of the capillary pores, for example, significant autogenous deformation and early-age cracking may result. More specifically, HPC often requires specialized curing procedures to avoid early-age cracking, which results from early emptying of the capillary pores, as well as the high self-desiccation and autogenous shrinkage that follow soon thereafter (Tuthill, 1936). Thus, the curing and application methods of curing are of great significance when considering the durability and performance of these mixtures.

This chapter addresses potential alternatives for low-humidity and high-temperature curing often encountered in Arizona (Kovler & Jensen, 2007). The desire to move internal curing from the laboratory to the field, and the need for more research in this area, was the impetus for this work.

CURING ASPECTS OF HPC

Adequate curing is vital to the production of high-quality concrete and strongly influences properties of hardened concrete such as durability, strength, water tightness, abrasion resistance, volume stability, resistance to freeze/thaw, and deicer salts. Exposed slab surfaces are especially

sensitive to curing due to the high surface area-to-volume ratio. Strength development and impermeability can be compromised significantly when curing is defective. In addition to promoting the hydration process, adequate curing also minimizes shrinkage (Aïtcin, 1998).

External and Internal Curing

External curing, as the traditional method of applying moisture to the exposed surface of the concrete, may include ponding, spraying, wet burlap, plastic sheeting, and application of curing compounds. In addition, various accelerated curing techniques can be applied. In general, external curing methods can be divided into two categories: water curing, which supplies additional moisture and also prevent moisture loss, and sealed curing, which prevents loss of moisture only. It is believed that water curing is more effective than sealed curing, and water ponding is the preferred water-curing method for high-strength and high-performance concrete (Jensen & Hansen, 2001).

Most high-strength and high-performance concretes have a low w/cm ratio with insufficient mixing water to maintain the water-filled coarse capillaries needed to sustain cement hydration and pozzolanic reactions. For this reason, curing based on an internal water supply is more effective. Internal water curing is preferable since the low permeability and sealing will not prevent self-desiccation (ASTM, 1999a; ASTM, 1999b).

Internal curing requires the introduction of a component that serves as a curing agent to the concrete mixture. This agent can be a normal aggregate introduced with specific conditions (e.g., water-saturated state) or a new component (e.g., an admixture or super absorbent polymers) (Mechtcherine, Dudziak & Schulze, 2006). Internal curing can be classified as internal sealing, where the agent is intended to delay/prevent loss of water from hardened concrete, or internal water curing, where the agent serves as a water reservoir and gradually releases the water. These methods are described in the following sections.

Internal Sealing

Dhir et al. introduced a method of concrete curing that involves adding water-soluble chemicals during the mixing process that will reduce water evaporation as the concrete is exposed to air-drying while also reducing water loss to the underlying concrete (Dhir et al., 1994). Water-soluble polymers having hydroxyl (-OH) and ether (-O-) functional groups satisfy the requirements for “self-cure chemicals,” in that they enhance water retention and provide an increased degree of hydration in the concrete. These admixtures alter the C-S-H gel morphology, reducing absorptivity of the concrete (Dhir, Hewlett & Dyer, 1996).

Jensen and Hansen proposed a new method for preventing self-desiccation by using super-absorbent polymer particles in the concrete mixture (Jensen & Hansen, 2001). During concrete mixing, the particles of super-absorbent polymers absorb a huge amount of water and form macro-inclusions containing free water. This free water is consumed during cement hydration, providing internal curing to the surrounding paste matrix.

The water-tightness and impermeability of high-performance mixtures negatively affects the efficiency of traditional external curing, which depends primarily on the moisture transport process. As the internal curing agent is finely dispersed and becomes part of the system, it can delineate the permeability of low w/b ratio cementitious systems. By this means, the internal water supply can be considered as the most efficient method for reducing autogenous shrinkage, since it directly affects self-desiccation.

Aggregates used in normal concrete may contain water, which can internally cure concrete. Even normal-weight aggregate, if pre-saturated, may serve as an internal curing agent and can reduce autogenous shrinkage to a certain extent (Zhutovsky, Kovler & Bentur, 2002). Addition of pre-saturated lightweight aggregates with large open porosity is a much more effective internal curing method. Lightweight aggregates have been used in concrete for over a century as a method to reduce the self-weight of concrete, but its use as an internal curing agent is a more recent development (Jensen & Hansen, 2001; Philleo, 1991; Bentz & Weiss, 2008). Several studies have found that self-desiccation can be counteracted by utilizing pre-saturated lightweight aggregate (Hammer, 1992; Vaysburd, 1996; Weber & Reinhardt, 1995; Weber & Reinhardt, 1997). These researchers suggested incorporating saturated lightweight aggregate into the concrete mixture to provide the internal source of water necessary to replace that consumed by chemical shrinkage during hydration. As the cement hydrates, this extra water will be drawn from relatively large pores in the lightweight aggregate into the much smaller pores in the cement paste. This will minimize the development of autogenous shrinkage, since according to the Kelvin-Laplace equation shrinkage stress is controlled by the size of the smallest pores (Bentz, Geiker & Hansen, 2001). This has been referred to as “autogenous curing” (Weber & Reinhardt, 1997). Since self-desiccation could be diminished or even prevented by this method, the autogenous shrinkage, occurring in parallel with self-desiccation, also would be affected. The results of experiments on lightweight concrete in which normal aggregate was replaced by pre-saturated lightweight aggregate show that high-strength concrete without autogenous shrinkage could be developed successfully by using this method (Schwesinger & Sickert, 2002; van Breugel, Outwerk & De Vries, 2000; Lura & van Breugel, 2000; Kitsutaka et al., 2002; Bentur, Igarashi & Kovler, 2001; Lura, van Breugel & Maruyama, 2002).

EARLY-AGE SHRINKAGE

HPC with low w/cm ratios are characterized by a high cracking sensitivity, which is a consequence of increased autogenous shrinkage. Autogenous shrinkages of HPC can reach high strain values (e.g., -250×10^{-6} in/in) within 24 hours, leading to premature cracking due to the low strength of materials if movement is fully restrained (Cusson & Hoogeveen, 2008). Adequate shrinkage prevention measures must be active at very early ages since self-desiccation cannot be eliminated by traditional curing methods. Several researchers applied internal curing by means of saturated lightweight aggregate and showed it to be effective in eliminating autogenous shrinkage (Takada et al., 1998; Collins & Sanjayan, 1999; Kohno et al., 1999). By performing the free and restrained shrinkage testing of large-size HPC specimens, Cusson and Hoogeveen found that internal curing eliminates autogenous shrinkage almost completely while maintaining the critical tensile stress well under the tensile strength to prevent cracking (Cusson & Hoogeveen, 2008). The internal drying of concrete pores due to hydration generates a driving force to transport water from the pores of the lightweight aggregate into the partially dried pores

of the cementitious matrix. The mechanisms of this transport process also may be associated with capillary effects, since the pores in the paste matrix are considerably smaller than those of the lightweight aggregate and, as a result, capillary suction may take place (Bentur, Igarashi & Kovler, 2001). Normal-weight aggregates (due to less porosity) have less water available to contribute to the drying pores of cementitious matrix.

Replacing the normal-weight aggregate with sufficient volume of pre-saturated lightweight aggregate can reduce or eliminate the plastic shrinkage cracking of mortars and concretes under severe exposure conditions (Henkensiefken et al., 2010). The supply of water reduces the settlement accompanying evaporation and the magnitude of the capillary stresses that are developed during drying, as the water-filled pores in the lightweight aggregate generally are larger than those in the hydrating cement paste.

EXPERIMENTAL PROGRAM

The researchers evaluated the effect of internal curing, supplied via saturated surface-dry, lightweight coarse aggregates, on the compressive strength development of HPC. It was expected that internal curing would be particularly beneficial for the concretes containing a type F fly ash, because it provides free water for hydration reactions.

The effect of internal curing on compressive strength was studied in increments of 7 and 28 days. To capture this effect, the researchers studied three strength levels (low-strength, mid-strength, and high-strength). At each strength level, they tested one control and two lightweight mixtures with two different lightweight coarse aggregates. The scope of the test program is shown in Table 16 and includes a test matrix consisting of the number of replicates for each mix code designated by the type of lightweight coarse aggregate and the different ages tested under compression loadings. For all compression tests, 3-inch by 6-inch cylinders were used.

The mixture proportions of all samples are shown in Table 17. The fine aggregate was normal sand with the grain size distribution shown in Figure 21. Portland cement (Type II) was used as the binding agent, and type F fly ash (Cholla, manufactured by Salt River Materials Group) was used as a partial cement replacement material. The properties of the lightweight aggregates are presented in the following section.

Table 16. Scope of the Test Program.

Intended Strength Level	Mix Code	Conditioning Regime	Lightweight Coarse Aggregate	Source	Compression Tests	
					Age	
					7 Days	28 Days
Low-Strength	C-L	Sealed Room Temp.	Control (no LWA)	Salt River Materials Group	2	2
	CBA-L	Sealed Room Temp.	Cholla Bottom Ash	Cholla plant, Salt River Materials group Flyash	2	2
	SBA-L	Sealed Room Temp.	Sintered Bottom Ash	Universal Aggregate	2	2
Mid-Strength	C-M	122° F, RH<10%	Control (no LWA)	Salt River Materials Group	2	2
	CBA-M	122° F, RH<10%	Cholla Bottom Ash	Cholla plant, Salt River Materials group Flyash	2	2
	SBA-M	122° F, RH<10%	Sintered Bottom Ash	Universal Aggregate	2	2
High-Strength	C-H	122° F, RH<10%	Control (no LWA)	Salt River Materials Group	2	2
	CBA-H	122° F, RH<10%	Cholla Bottom Ash	Cholla plant, Salt River Materials group Flyash	2	2
	SBA-H	122° F, RH<10%	Sintered Bottom Ash	Universal Aggregate	2	2

LWA = lightweight aggregate

Table 17. Mix Design of All Mixes.

Strength Level	Low-Strength		Mid-Strength		High-Strength	
	C-L	CBA-L, SBA-L	C-M	CBA-M, SBA-M	C-H	CBA-H, SBA-H
Portland Cement (Type II), lb/yd ³	455	455	555	555	655	655
Fly Ash (Type F), lb/yd ³	305	305	370	370	440	440
Fine Aggregate, lb/yd ³	1,290	1,290	1,205	1,205	1,205	1,205
Coarse Aggregate, lb/yd ³	1,600	825	1,475	715	1,290	530
Water, lb/yd ³	315	315	355	355	370	370
Density, lb/yd ³	3,900	3,200	3,900	3,200	3,900	3,200
Superplasticizer, %	0	0	0.4	0.4	0.8	0.8
w/cm	0.42	0.42	0.38	0.38	0.34	0.34
s/cm	1.70	1.70	1.30	1.30	1.10	1.10
FA, %	40%	40%	40%	40%	40%	40%

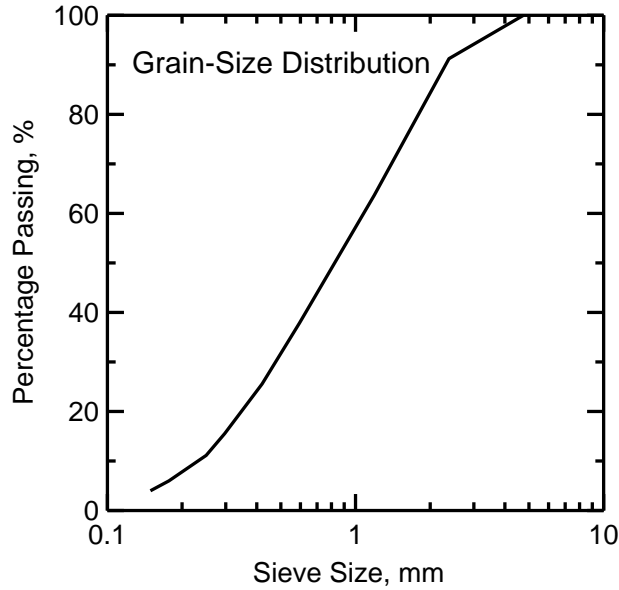


Figure 21. Grain Size Distribution of Fine Aggregate.

Lightweight Coarse Aggregates

Figure 22 shows photographs of the coarse aggregates used in this study, and Table 18 lists the particle size distributions for these aggregates. The physical properties of lightweight aggregates are very important when they are used in internal curing. The most important physical property of the lightweight aggregates is their ability to absorb a large portion of water and retain it for release as desiccation occurs. Table 19 presents the absorption properties of two lightweight aggregates used in this study, along with specific gravities and void contents.

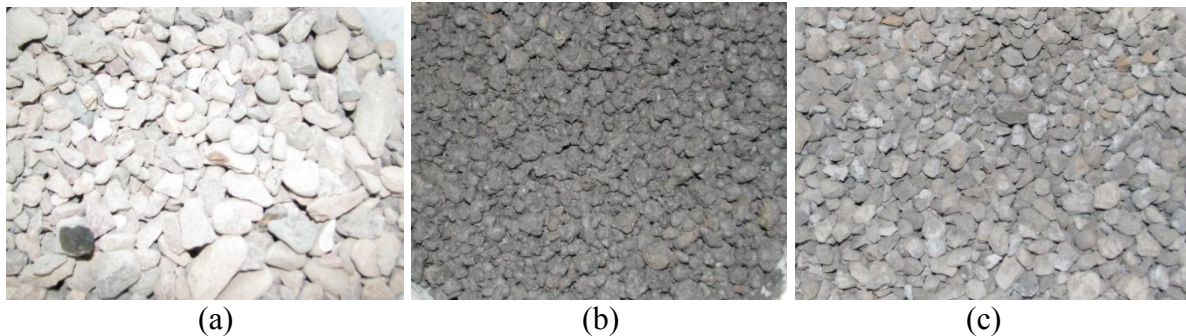


Figure 22. The Aggregates Used in This Study: a) Normal Weight Aggregate, b) Bottom Ash Aggregate, and c) Sintered Bottom Ash Aggregate.

Table 18. Particle Size Distribution of the Lightweight Aggregates Used in This Study.

Sieve Size	Percentage Passing, %	
	Bottom Ash	Sintered
6in	100	100
4in	100	100
3in	100	100
2in	100	100
1 ½in	100	100
1 ¼in	100	100
1in	100	100
¾in	100	99
½in	99	93
⅜in	42	66
¼in	2	1
#4, #8, #10, #16, #30, #40, #50	1	1
#100	0	1
#200	0	0.7

Table 19. Specific Gravities, Absorption, and Void Content of LWAs Used in This Study.

Property	Percentage Passing, %	
	Bottom Ash	Sintered Bottom Ash
Bulk Specific Gravity (Dry)	1.297	1.323
Bulk Specific Gravity (SSD)	1.417	1.738
Apparent Specific Gravity	1.474	2.260
Absorption (%)	9.24	31.32
Void Content (%)	48	46

SSD = saturated surface-dry

Pre-saturation, Mixing, and Casting Procedure

The lightweight aggregates were submerged in water for more than 48 hours prior to the casting (see Figure 23). Before making concrete, the submerged lightweight aggregates were dried with a cloth until they reached the saturated surface-dry state. The researchers adopted the following mixing procedure:

1. Pour water into a mixer.
2. Gradually introduce cementitious materials into the mixer, including cement and fly ash, and blend for 2 minutes as shown in Figure 24.
3. Add fine aggregate to the mixer and blend for 2 minutes before adding the coarse aggregate and mixing for 4 additional minutes to combine all the ingredients thoroughly.
4. Lubricate compressive cylinder molds, then pour three layers of concrete into each mold. Compact each layer using a thin rod.
5. Cover the compressive specimens with lids immediately after casting. Two different conditioning methods were considered for these samples. The low-strength samples were kept sealed inside the molds prior to testing at 7 and 28 days, while the mid- and high-

strength samples were kept in an incubator under drying conditions at a constant temperature of 105° F.

6. Demold the specimens before testing with a compression hydraulic machine.

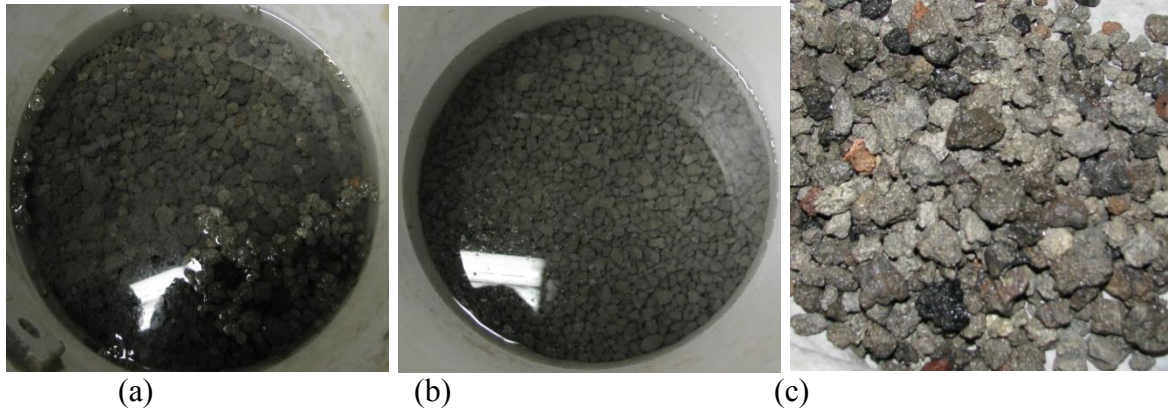


Figure 23. Submerged Lightweight Aggregates in Water: a) Bottom Ash, b) Sintered Bottom Ash, and c) Saturated Surface-dry Condition of Aggregates Prior to Use.



Figure 24. Casting Concrete with Lightweight Aggregate: a) Materials before Pouring into Mixer and b) Materials after Mixing.

RESULTS AND DISCUSSION OF COMPRESSIVE TESTS

Low-Strength Samples

Figures 25 through 27 show the results of the compressive tests on low-strength control, bottom ash, and sintered bottom ash samples at 7 and 28 days. Results of the experimental analysis and the associated parameters of modulus of elasticity, peak axial strain, compressive strength, and Poisson's ratio are summarized in Table 20.

As presented in the table, the modulus of elasticity of CBA-L and SBA-L samples show 20 percent and 15 percent reduction at 7 days, as compared to the control sample, while the values of strain at the peak stress increase by 33 percent and 25 percent over the control sample,

respectively. The compressive strength of CBA-L samples at 7 days shows a reduction by 19 percent. However, the compressive strength of SBA-L samples at 7 days increases by 18 percent. Poisson's ratio of both internally cured samples increases in the range of 11 to 18 percent at 7 days, compared to the control samples.

Similar results were observed at later ages (28 days), as reductions in the range of 14 to 27 percent are reported for the modulus of elasticity of internally cured samples. Also, both internally cured samples show increases in the values of strain at the peak stress at 28 days; 78 percent and 89 percent increases over the control sample are reported for CBA-L and SBA-L samples, respectively. Values of Poisson's ratio increase for CBA-L by 9 percent and decrease for SBA-L by 8 percent at later ages. Both CBA-L and SBA-L samples show increases in the values of peak stress by as much as 25 percent at 28 days, indicating that increased hydration overcomes any strength reduction due to the addition of porous lightweight aggregates.

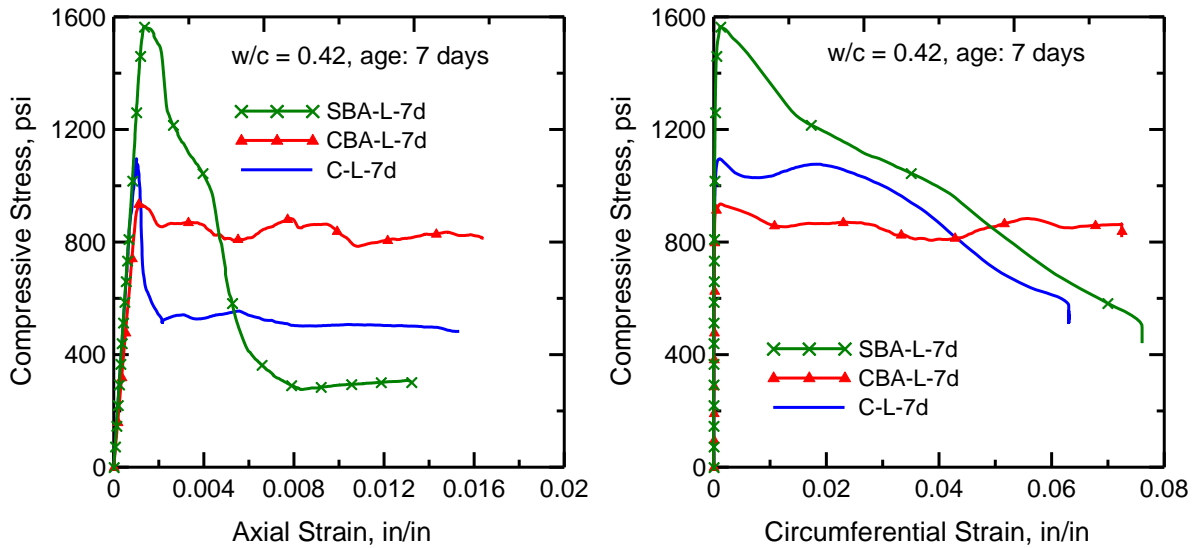


Figure 25. Comparative Results of Compression Tests at 7 Days (Low-strength Level).

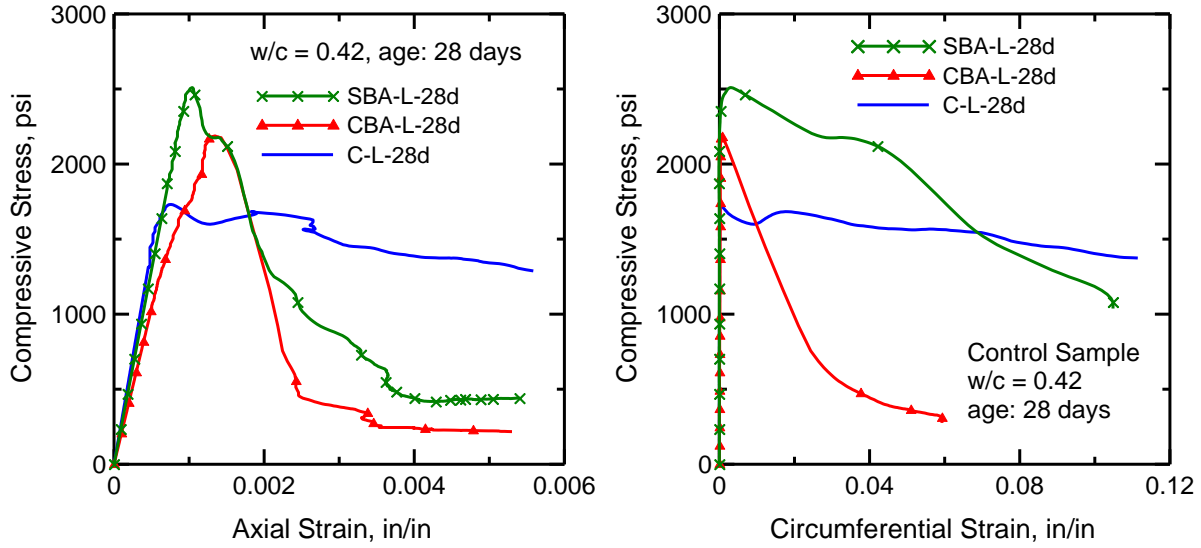


Figure 26. Comparative Results of Compression Tests at 28 Days (Low-strength Level).

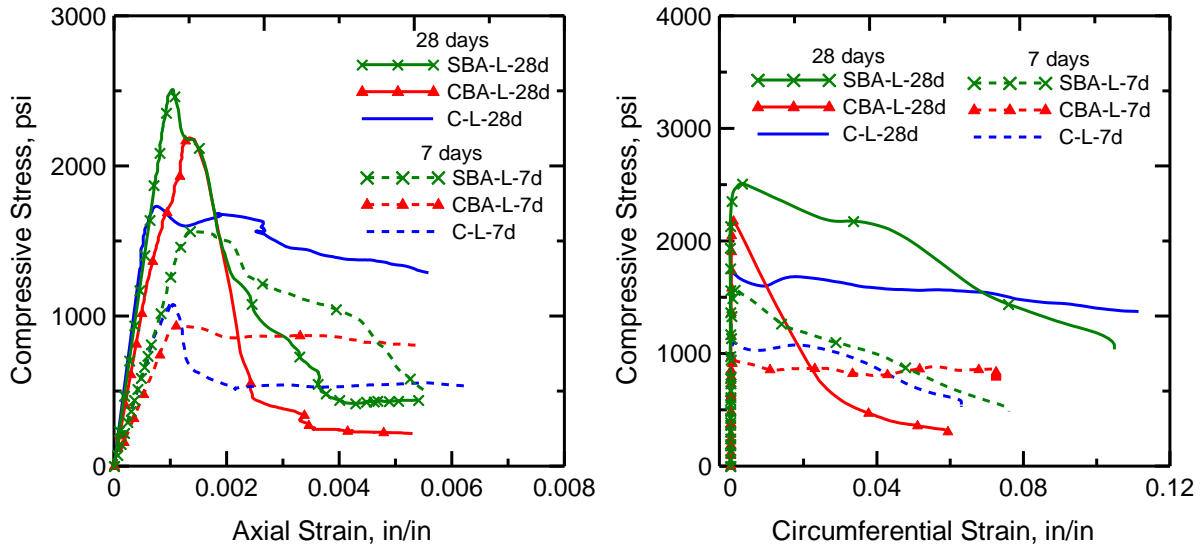


Figure 27. Effect of Internal Curing on the Compressive Test Results (Low-strength Level).

Table 20. Compression Data Summary (Low-strength Level).

Mix	Sample Code	Age, days	Modulus of Elasticity, $\times 10^6$ psi	Peak Axial Strain, in/in	Compressive Strength, psi	Poisson's Ratio
C-L	C-L-7d-1	7	1.255	0.0014	1,348	0.189
	C-L-7d-2	7	1.206	0.0010	1,095	0.208
	Average	7	1.230	0.0012	1,222	0.199
	C-L-28d-1	28	2.480	0.0009	2,254	0.251
	C-L-28d-2	28	2.875	0.0008	1,730	0.232
	Average	28	2.677	0.0009	1,992	0.242
CBA-L	CBA-L-7d-1	7	0.913	0.0011	935	0.265
	CBA-L-7d-2	7	1.032	0.0021	1,033	0.204
	Average	7	0.972	0.0016	984	0.2345
	CBA-L-28d-1	28	1.847	0.0018	2,695	0.258
	CBA-L-28d-2	28	2.076	0.0013	2,187	0.270
	Average	28	1.961	0.0016	2,441	0.264
SBA-L	SBA-L-7d-1	7	0.870	0.0016	1,317	0.238
	SBA-L-7d-2	7	1.230	0.0013	1,565	0.203
	Average	7	1.050	0.0015	1,441	0.220
	SBA-L-28d-1	28	1.995	0.0024	2,554	0.213
	SBA-L-28d-2	28	2.593	0.0010	2,509	0.231
	Average	28	2.294	0.0017	2,531	0.222

Mid- and High-Strength Samples

Figures 28 through 33 show the results of the compressive tests on mid-strength and high-strength control, bottom ash, and sintered bottom ash samples at 7 and 28 days. Results of the experimental analysis and the associated parameters of modulus of elasticity, peak axial strain, compressive strength, and Poisson's ratio are summarized in Tables 21 and 22.

The modulus of elasticity and strain at peak stress of mid-strength internally cured samples at 7 days are very similar to the control samples. The compressive strength of internally cured mid-strength samples shows a 10 percent increase due to the addition of lightweight aggregates and subsequent increase in the hydration. Poisson's ratio decreased at 7 days for mid-strength samples due to internal curing. Later age results for mid-strength samples are very similar to the 7 days results; the only difference is the magnitude of increase in compressive strength due to internal curing, which is about 70 percent more than the control samples. Also, peak axial strains are doubled for internally cured samples.

An 18 percent reduction in the modulus of elasticity is reported for SBA-H. However, no difference is observed between CBA-H and C-H on this parameter. Strain at peak stress

increases in CBA-H by 10 percent and decreases in SBA-H by 15 percent, as compared to the control samples. However, compressive strength increases in both internally cured samples in the range of 30 to 40 percent. An increase in the Poisson's ratio in the range of 7 to 13 percent is reported due to internal curing. At 28 days, both internally cured samples show an increase in the modulus of elasticity in the range of 10 to 35 percent. Reductions in peak axial strains of 57 percent and 14 percent are observed for CBA-H and SBA-H samples, respectively. However, 31 percent and 14 percent increases are reported in the compressive strength of 28-day high-strength samples of CBA-H and SBA-H, respectively. Poisson's ratio increases by 17 percent for SBA-H and by 7 percent for CBA-H.

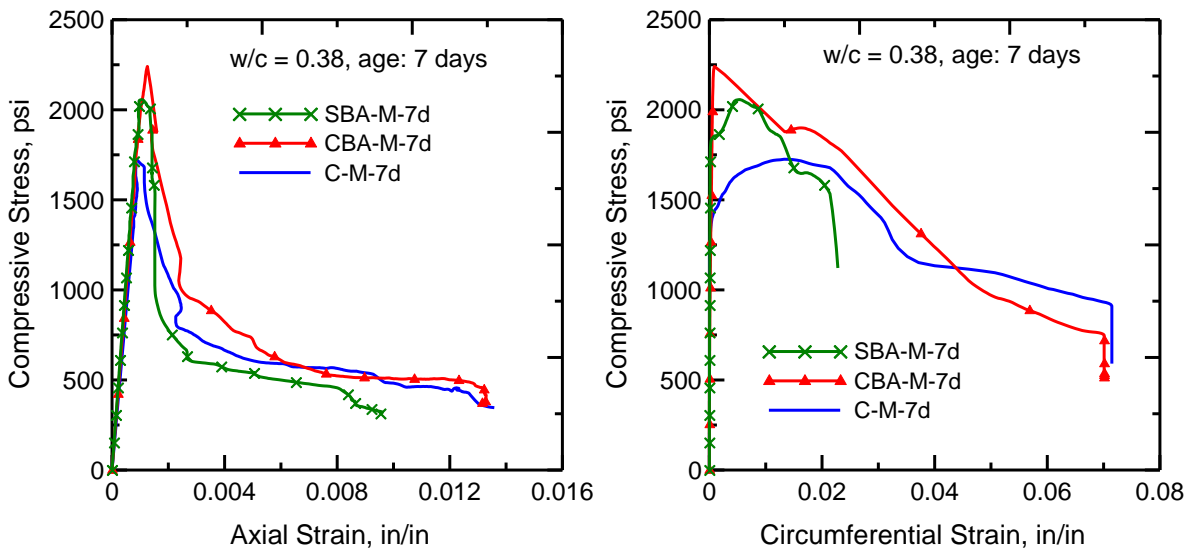


Figure 28. Comparative Results of Compression Tests at 7 Days (Mid-strength Level).

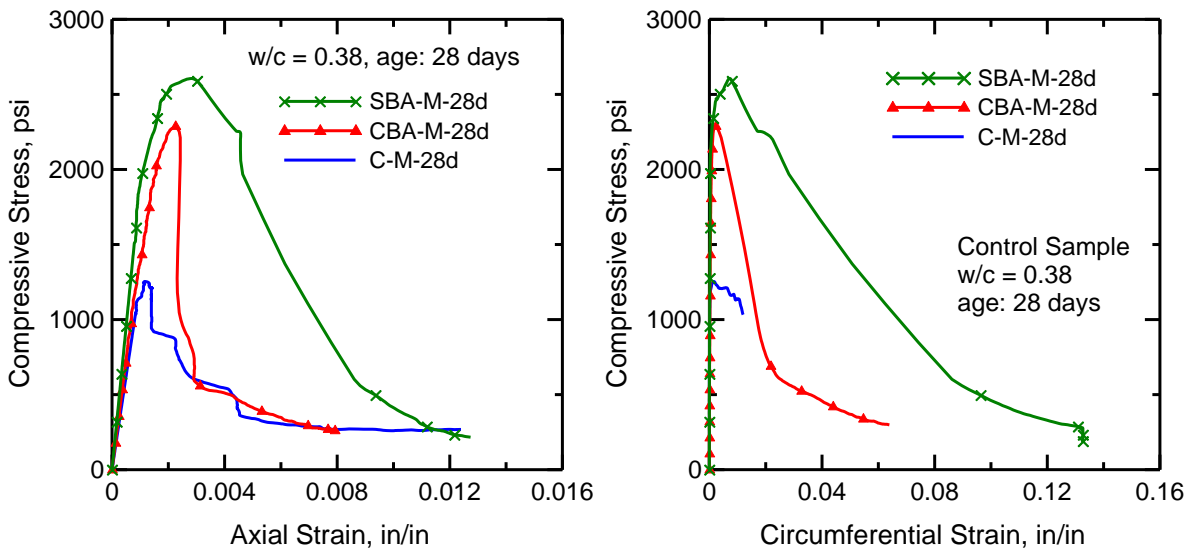


Figure 29. Comparative Results of Compression Tests at 28 Days (Mid-strength Level).

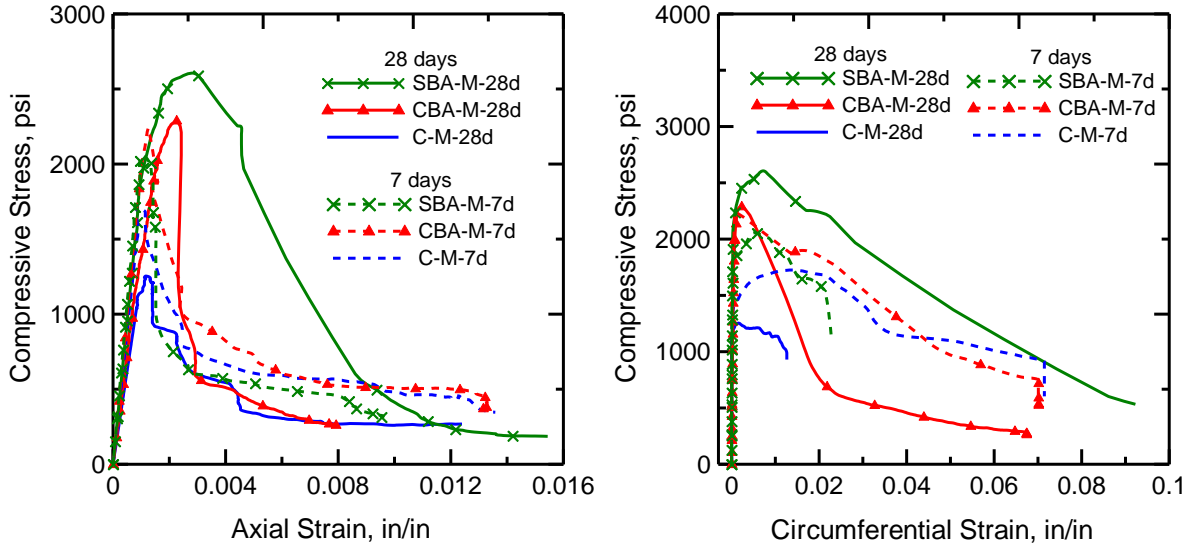


Figure 30. Effect of Internal Curing on the Compressive Test Results (Mid-strength Level).

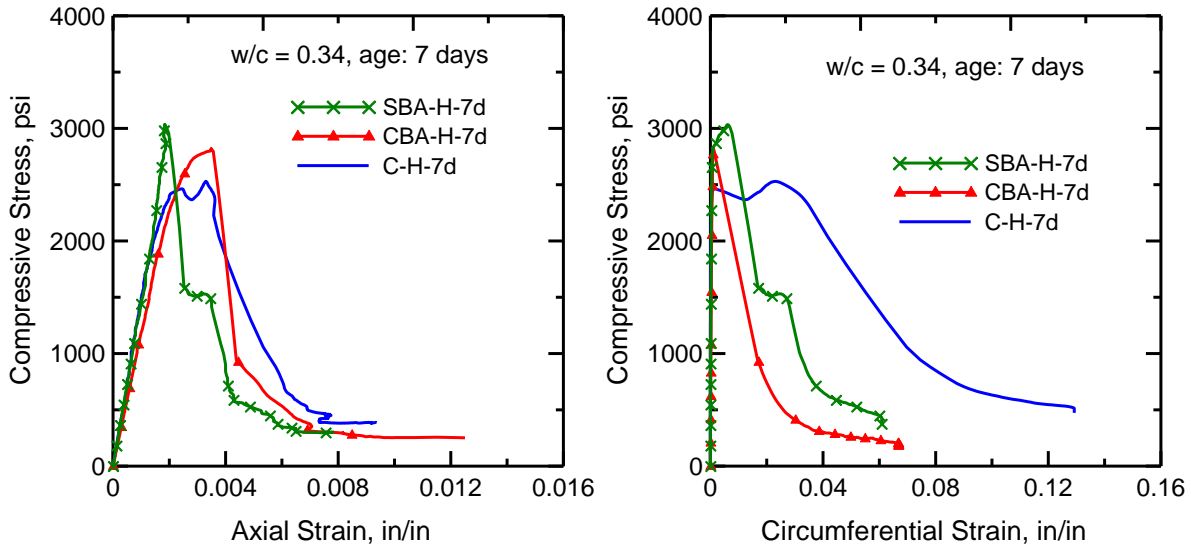


Figure 31. Comparative Results of Compression Tests at 7 Days (High-strength Level).

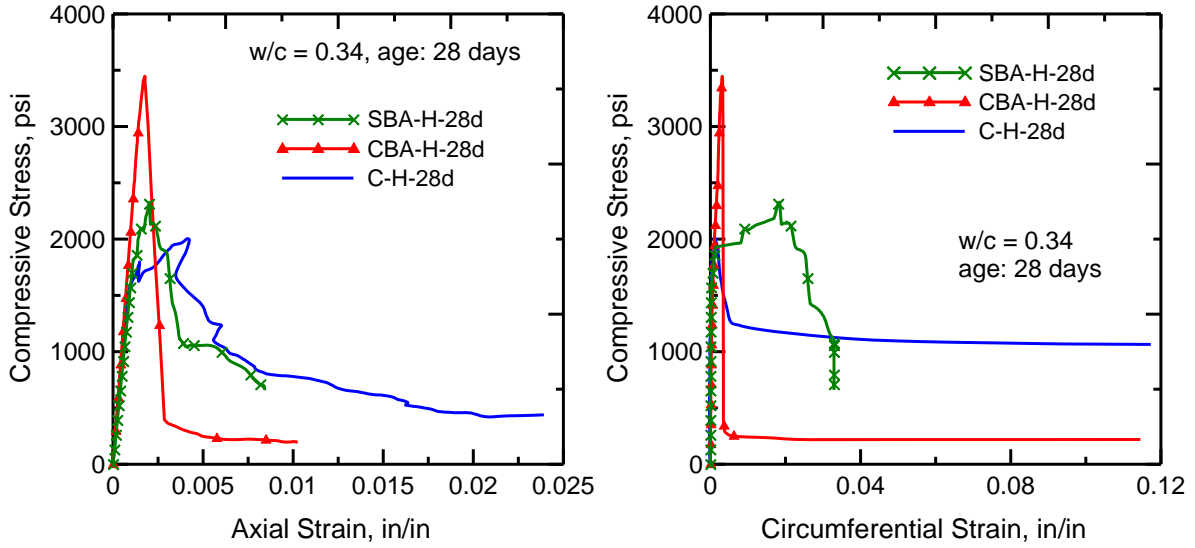


Figure 32. Comparative Results of Compression Tests at 28 Days (High-strength Level).

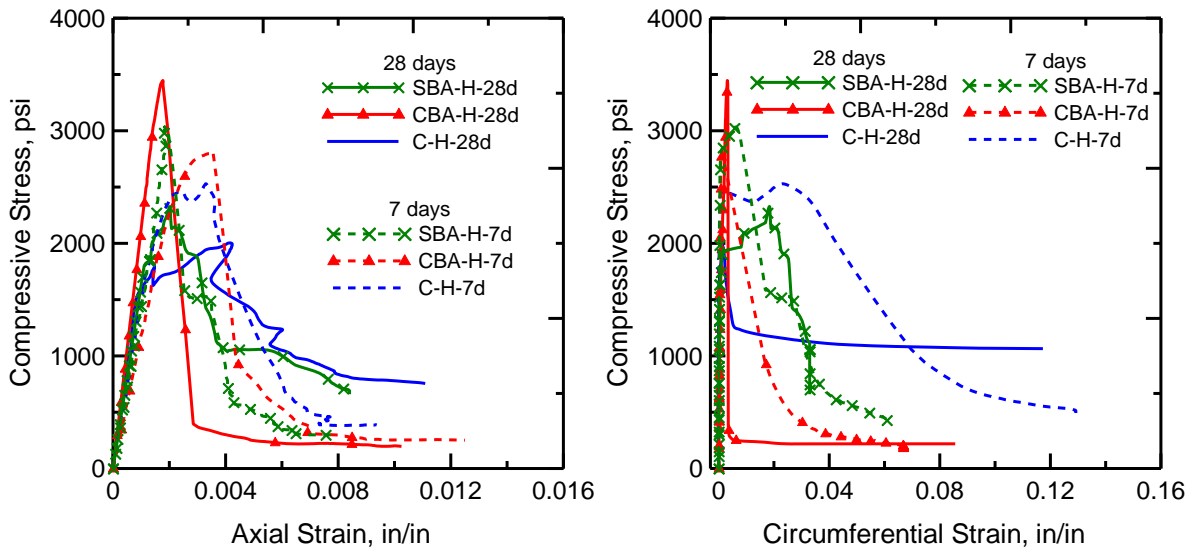


Figure 33. Effect of Internal Curing on the Compressive Test Results (High-strength Level).

Table 21. Compression Data Summary (Mid-strength Level).

Mix	Sample Code	Age, days	Modulus of Elasticity, x10 ⁶ psi	Peak Axial Strain, in/in	Compressive Strength, psi	Poisson's Ratio
C-M	C-M-7d-1	7	1.592	0.0014	1,720	0.237
	C-M-7d-2	7	1.767	0.0008	1,725	0.215
	Average	7	1.680	0.0011	1,722	0.226
	C-M-28d-1	28	1.245	0.0012	1,253	0.219
	C-M-28d-2	28	1.951	0.0011	1,406	0.204
	Average	28	1.598	0.00115	1,330	0.211
CBA-M	CBA-M-7d-1	7	1.478	0.0073*	1,468	0.208
	CBA-M-7d-2	7	2.008	0.0013	2,240	0.177
	Average	7	1.743	0.0013	1,854	0.192
	CBA-M-28d-1	28	1.404	0.0022	2,195	0.189
	CBA-M-28d-2	28	1.471	0.0022	2,288	0.276
	Average	28	1.438	0.0022	2,242	0.232
SBA-M	SBA-M-7d-1	7	1.401	0.0069*	1,721	0.234
	SBA-M-7d-2	7	2.141	0.0011	2,056	0.162
	Average	7	1.771	0.0011	1,888	0.198
	SBA-M-28d-1	28	1.483	0.0058*	1,962	0.239
	SBA-M-28d-2	28	1.905	0.0028	2,606	0.241
	Average	28	1.694	0.0028	2,284	0.240

* The peak axial strains for these samples are related to the second peak in the curve

Table 22. Compression Data Summary (High-strength Level).

Mix	Sample Code	Age, days	Modulus of Elasticity, $\times 10^6$ psi	Peak Axial Strain, in/in	Compressive Strength, psi	Poisson's Ratio
C-H	C-H-7d-1	7	1.321	0.0032	1,630	0.253
	C-H-7d-2	7	1.450	0.0033	2,529	0.141
	Average	7	1.386	0.0032	2,079	0.197
	C-H-28d-1	28	1.636	0.01*	1,904	0.201
	C-H-28d-2	28	1.806	0.0042	2,003	0.219
	Average	28	1.721	0.0042	1,954	0.210
CBA-H	CBA-H-7d-1	7	1.179	0.0035	2,818	0.248
	CBA-H-7d-2	7	1.105	0.0099*	2,491	0.174
	Average	7	1.142	0.0035	2,655	0.211
	CBA-H-28d-1	28	2.528	0.0068*	1,671	0.229
	CBA-H-28d-2	28	2.129	0.0018	3,446	0.264
	Average	28	2.329	0.0018	2,559	0.246
SBA-H	SBA-H-7d-1	7	1.348	0.0036	2,749	0.217
	SBA-H-7d-2	7	1.455	0.0018	3,033	0.228
	Average	7	1.401	0.0027	2,891	0.222
	SBA-H-28d-1	28	2.149	0.0053	2,126	0.227
	SBA-H-28d-2	28	1.629	0.002	2,327	0.224
	Average	28	1.889	0.0036	2,226	0.225

* The peak axial strains for these samples are related to the second peak in the curve

CONCLUSION

The superior results obtained for the internally cured samples with lightweight aggregates, especially sintered bottom ash, indicate that there is great potential to use them for hot-weather concreting, as well as when external curing is not possible, practical, or economical. The lower strengths observed for the mid-strength and high-strength samples may be due to the harsh conditioning regime at the temperature of 122° F and very low relative humidity (RH<10 percent), which cause excessive moisture loss for which the available internal moisture cannot compensate.

CHAPTER 5. HIGH-VOLUME FLY ASH CONCRETE

INTRODUCTION

One of the most effective ways to decrease the cost of concrete is to reduce the cement content, especially in areas where short-term strength is not a critical design parameter. By replacing a portion of the cement with higher quantities of fly ash, in the range of 30 to 40 percent class F, agencies can reduce the overall cost of the concrete and reduce the thermal mass generation, especially in large sections such as drilled shafts and bridge piers.

To study the material properties of HVFA concrete, the researchers measured the mechanical properties of HVFA specimens sampled from a construction site where HVFA concrete was used in the construction of composite decks. The objective of this work was to study the effect that using 35 percent fly ash as a partial replacement for cement has on the mechanical properties of the concrete while also examining the cracking tendency of the concrete.

MECHANICAL PROPERTIES

This section presents the results of compression tests and cyclic three-point bending tests on HVFA containing 35 percent cement replacement with class F fly ash. Concrete samples are evaluated at 7 and 28 days. Table 23 shows the mixture proportions of the concrete.

Table 23. Mixture Proportions of HVFA Concrete.

HVFAC	Weight Proportions
FA, %	35%
Type II Cement	360 lb/yd ³
Fly ash Content	200 lb/yd ³
Water Content	275 lb/yd ³
Coarse Aggregate, Cholla	1806 lb/yd ³
Fine Aggregate, Cholla	1261 lb/yd ³
w/cm	0.49

The samples were kept at the construction site and covered with sealed plastic sheets for 24 hours before being moved to the testing laboratory. Samples were cured in 70° F water for 7 and 28 days. A water-cooled diamond blade circular saw was used to cut a 0.5-inch notch at the mid-span of the specimens for three-point bending or fracture tests. The specimens were allowed to dry in the laboratory for 12 hours prior to testing.

Compressive Properties of HVFA Concrete

Figure 34 shows an overview of the instrumented specimen (3-inch by 6-inch cylinder) used to obtain the full cycle of the stress-strain response in compression tests as shown in Figure 35. Table 24 presents the results of compression tests on HVFA concrete at 7 and 28 days. Figure 36 shows the plot of the stress-strain curves obtained from closed-loop compression tests for samples after 7 and 28 days of curing. The test results indicate that, with 35 percent fly ash replacement, one can reach a strength of 3,000 to 4,000 psi after 28 days of curing. Additional testing is required in this area to document the statistics of strength gain using HVFA mixtures with even longer curing periods to develop application areas for HVFA mixtures.



Figure 34. Curing of Specimens in the Water Tank at a Constant Temperature of 70° F.

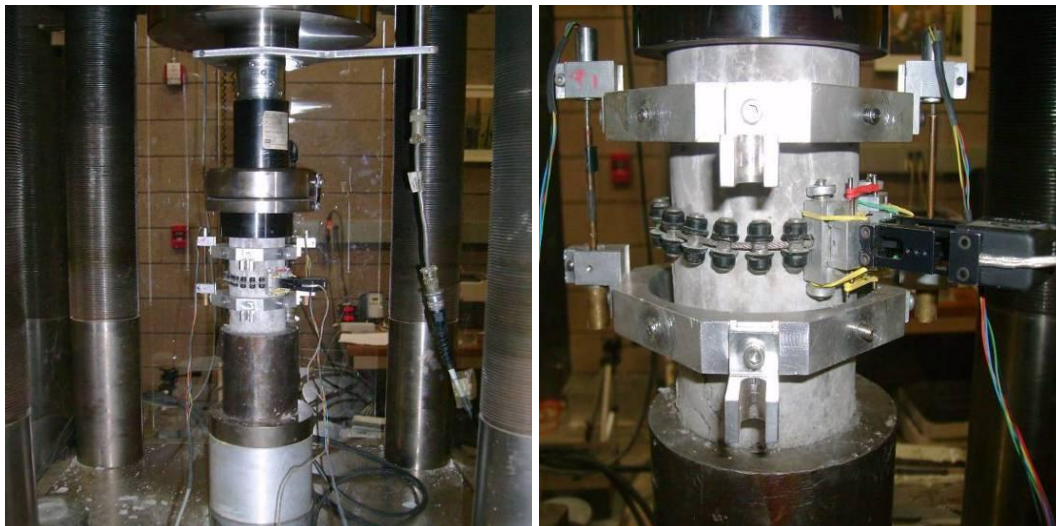


Figure 35. Closed-loop Compression Test Setup.

Table 24. Compression Test Results for the HVFA Concrete Samples at 7 and 28 Days.

Sample ID	Age, days	Fly Ash, %	Strength, psi	Strain at Peak Load, 10^{-3} in/in	Modulus of Elasticity, ksi	Poisson's Ratio	Toughness, psi
HVFAC_7d_1	7	35	2,600	4.347	5.02	0.184	4.97
HVFAC_7d_2	7	35	2,689	2.017	3.89	0.13	3.9
HVFAC_28d_1	28	35	3,230	1.815	7.65	0.186	4.16
HVFAC_28d_2	28	35	3,806	3.461	6.94	0.158	9.26

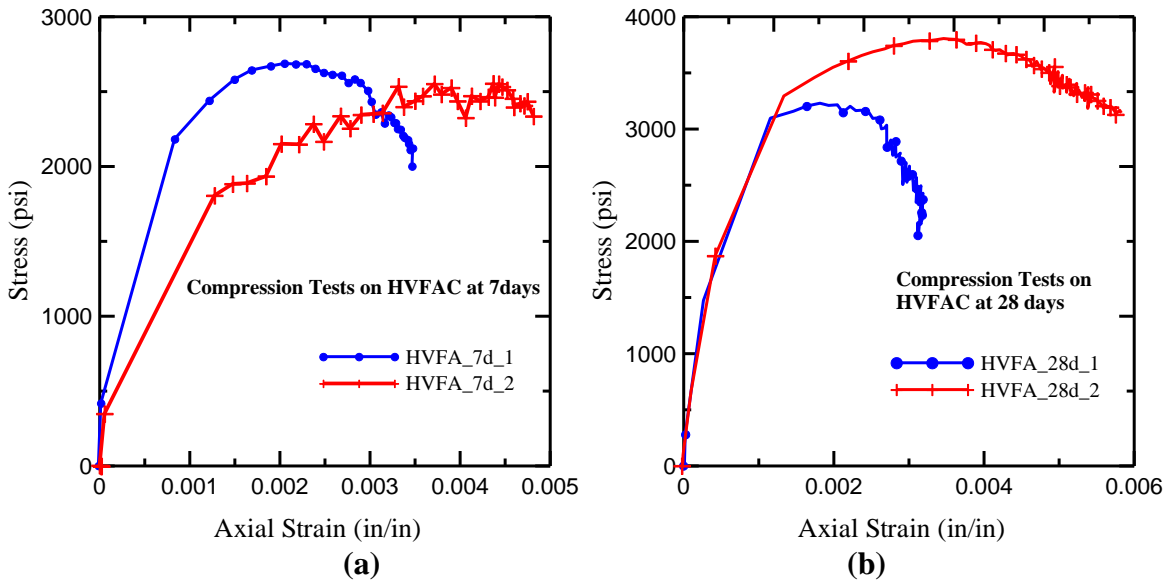


Figure 36. Compressive Stress vs. Axial Strain of HVFA Concrete at a) 7 Days and b) 28 Days.

Flexural Properties of HVFA Concrete

Flexure tests may be conducted under several loading configurations. Since the tensile strength of concrete is relatively low, the tests involving only opening or tensile displacements along the crack, called mode I tests, are quite important. In the most common mode I test configuration, a notched beam is loaded at mid-span. The test is performed under closed-loop control with CMOD as the controlled variable. Figure 37a shows the flexural test setup. In this test, the CMOD was measured across the face of the notch using an extensometer. The extensometer measuring CMOD at the notch is shown in Figure 37b.

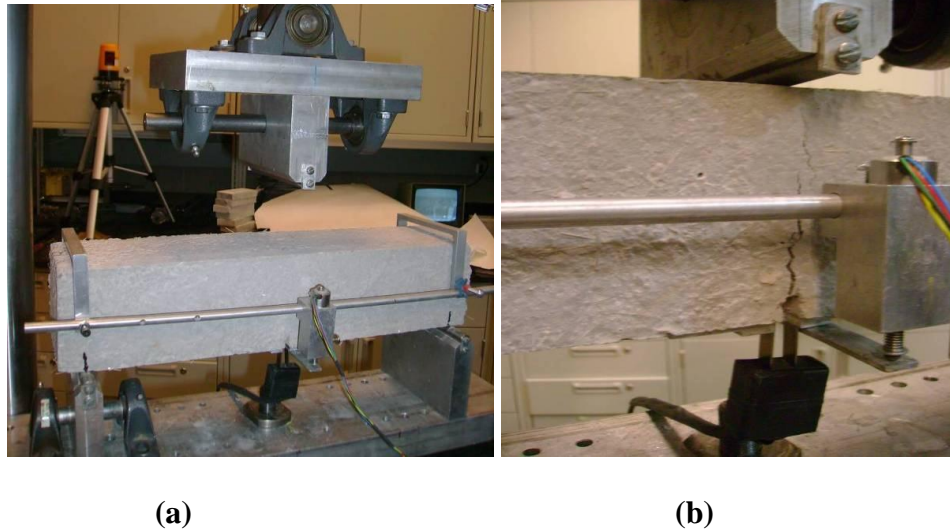


Figure 37. a) Closed-loop Flexural Test Setup; b) Measuring CMOD at the Notch by Extensometer and Displacement at the Mid-span by LVDT.

Three-point cyclic flexural tests were performed on 18-inch by 4-inch by 4-inch beam specimens with an initial notch of 0.5 inches. A test span of 16 inches was used. The deflection of the beam was measured using a spring-loaded LVDT with a range of 0.1 inch. The results of the fracture tests on HVFA concrete at 7 and 28 days are presented in Table 25. Figure 38 shows plots of the load vs. CMOD curves obtained from the cyclic flexural tests.

Table 25. Three-point Bending Test Results for HVFA Concrete Samples at 7 and 28 Days.

Sample ID	Age, days	Fly Ash, %	Max Load, lb	Average Max Load, lb	Flexural Strength, psi	CMOD at Peak Load, $\times 10^{-3}$ in	Avg. CMOD at Max Load, $\times 10^{-3}$ in	Deflection at Max Load, $\times 10^{-3}$ in/in	Avg. Deflection at Max Load, $\times 10^{-3}$ in/in
HVFA_7d_1	7	35	1,069	1079	401	1.963	1.75	1.433	1.34
HVFA_7d_2	7	35	1,090		409	1.543		1.248	
HVFA_28d_1	28	35	1,083	1161	406	1.617	1.72	3.861	3.18
HVFA_28d_2	28	35	1,166		437	2.01		4.106	
HVFA_28d_3	28	35	1,234		463	1.522		1.587	

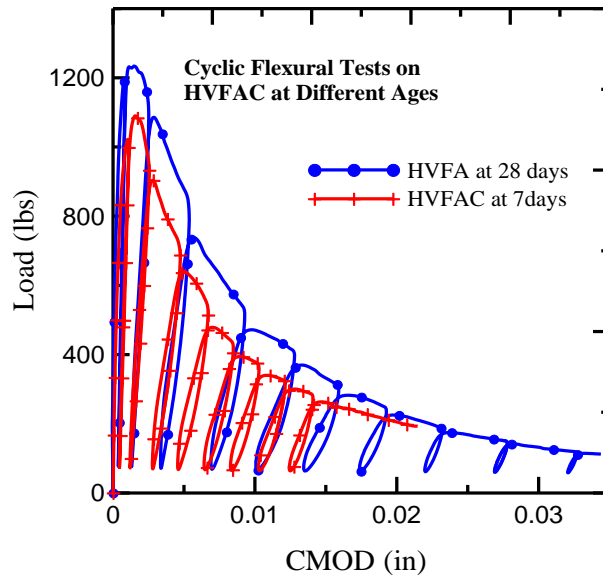


Figure 38. Flexural Response of Load vs. CMOD of HVFA Concrete at 7 and 28 Days.

CRACKING TENDENCY OF HVFA CONCRETE DUE TO RESTRAINED SHRINKAGE

Ring-type specimens were used to simulate restrained shrinkage cracking of HVFA concrete. The setup consists of a 2.625-inch-thick cylinder of concrete, which is cast around a rigid steel ring 11.4 inches in diameter and 5.25 inches high, as shown in Figure 39. Three such specimens were prepared. The specimens were demolded after 24 hours and cured in a curing room using wet burlap for 3 days. Then, the samples were moved to the laboratory and kept in a shrinkage chamber for observation. Drying was allowed from the outer circumferential surface. The specimens then were placed in an environmental chamber at a temperature of 104° F and inspected for 42 days using a continuous recording of the strain gauges attached to the inner surface of the steel ring. A view of the chamber is shown in Figure 40.

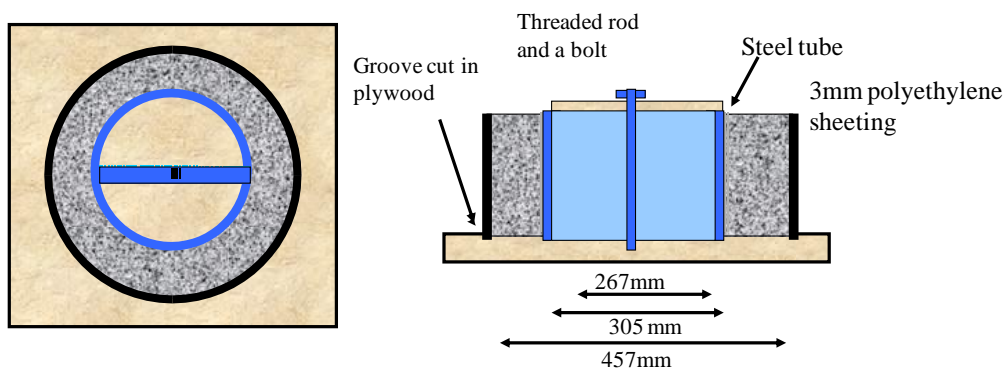


Figure 39. Configuration and Geometry of the Ring Test Specimen.



Figure 40. Shrinkage Chamber (with Cover Door Removed) Designed to Subject Restrained Concrete Ring Samples to Low Humidity Conditions.

The researchers examined the surface of the specimens for new cracks and attempted to measure the width of any existing cracks every 24 hours during the first 7 days. Thereafter, measurements were taken every 48 hours. None of the HVFA concrete specimens showed any cracking after the specimens were kept inside the chamber for 42 days. Figure 41 represents the response of strain gauges attached to the specimen. These responses are measured as a function of time and can be used to detect the timing of the cracking in the specimen. However, in the absence of any cracking, there was no sudden change observed in the response of the strain gauge that was mounted to steel specimens.

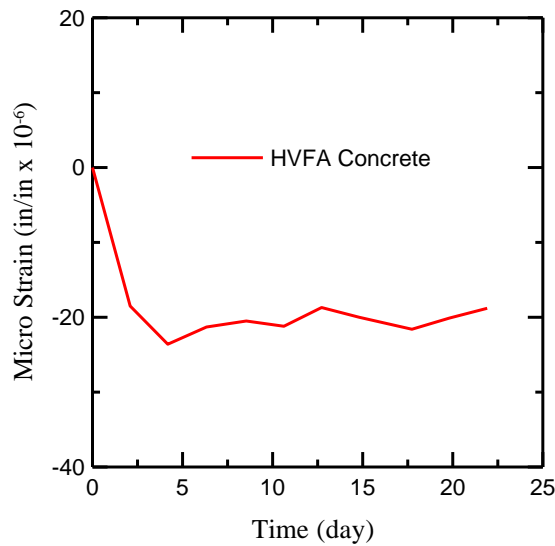


Figure 41. Strain Gauge Readings vs. Time for HVFA Concrete Specimen.

From the results of the shrinkage tests, it was concluded that using high dosages of fly ash as a partial replacement of cement in concrete significantly decreases the concrete shrinkage. This reduction in shrinkage strains is so significant that no cracking occurred in HVFA concrete samples after 42 days inside the environmental chamber. No transverse cracking was observed in HVFA concrete specimens after 42 days inside the shrinkage chamber as shown in Figure 42.



Figure 42. Examination of HVFA Concrete Specimens after Exposure to the Shrinkage Chamber.

CONCLUSIONS

Evaluation of compression, flexural, and shrinkage tests on the HVFA concrete mixtures indicates that, with the use of 35 percent cement replacement, it is possible to reach 3,000 psi compressive strength at 28 days. Flexural samples show that while the samples retain brittleness similar to plain concrete, the flexural strength and ductility improve with the increase of curing from 7 to 18 days. Restrained shrinkage tests indicated that the potential for restrained shrinkage cracking significantly decreases in samples with HVFA, as compared to samples that contain cement only. This hypothesis requires further evaluation with additional samples to document the potential for reduced cracking in the HVFA samples.

CHAPTER 6. ENHANCING DURABILITY CHARACTERISTICS OF CONCRETE

INTRODUCTION

Durability is defined as the concrete’s ability to resist weathering, chemical attacks, abrasions, or any other deterioration. Durable concrete will retain its original form, quality, and serviceability when exposed to its environment. This chapter focuses on the durability characteristics of cement-based materials. The sulfate attack and ASR susceptibility of concrete is presented, as is the cracking tendency of concrete due to restrained shrinkage. The effects of fly ash on enhancing the performance of concrete against sulfate attacks and ASR are demonstrated first, followed by a discussion of the effect of adding fiber in controlling shrinkage cracking. This chapter concludes with some useful guidelines for the material design of concrete.

SULFATE ATTACK AND ASR

A variety of fly ashes were used experimentally to study their effectiveness in controlling the level of damage caused by sulfate attack and ASR. At a macro-scale study of sulfate attacks, the researchers followed the general guidelines of the ASTM C1012 test method using 1-inch by 1-inch by 11-inch specimens. The change in the test response (expansion) of paste mixtures was of significant interest in the blended cement systems. Three class F fly ashes (F1, F2, F3), two class C fly ashes (C1, C2), and one labeled as O fly ash (due to its high SO₃ content) were defined. Table 26 shows the oxide properties of the materials used.

Table 26. Chemical and Physical Properties of Raw Cementitious Materials.

Lab	Cement	F1	F2	F3	C1	C2	O
SiO ₂	21.62	62.93	58.72	56.48	52.16	37.2	41.1
Al ₂ O ₃	4.06	22.84	24.86	25.61	30.11	20.39	17.37
Fe ₂ O ₃	3.54	4.01	4.94	3.01	2.71	5.32	3.45
CaO	63.90	2.57	4.56	3.22	8.93	25.91	19.8
MgO	1.40	1.64	1.57	1.67	1.37	3.79	1.33
SO ₃	2.81	0.14	0.21	0.38	0.51	1.93	10.12
Na ₂ O	0.06	1.46	1.11	1.22	0.51	1.88	0.96
K ₂ O	0.54	1.53	1.11	1.49	1.55	0.45	0.78
L.O.I	1.42	0.16	0.25	5.43	0.4	0.22	4.18
ASTM	I/II	F	F	F	C/F	C	N

Na₂O = sodium oxide; K₂O = potassium oxide; LOI = loss on ignition; N = Class N pozzolan; other abbreviations are as previously defined

The linear expansions were measured using digital comparators for 18 months, and the results of four replicate samples were averaged for reporting. Figure 43 presents expansion-time curves for paste specimens at 30 percent replacement levels. The researchers observed that a majority of class F fly ash formulations could reduce the expansion up to 35 percent more than the control, while class C fly ashes behaved similar to the control. The O fly ash had a large expansion after about 200 days of exposure due to excessive SO₃ content (>10 percent).

At a micro-scale, environmental SEM and quantitative energy dispersive spectroscopy (EDS) were used to study the exposed specimens for the determination of reaction products and fronts as shown in Energy: Kilo Electron Volts (keV)

Figure 44.

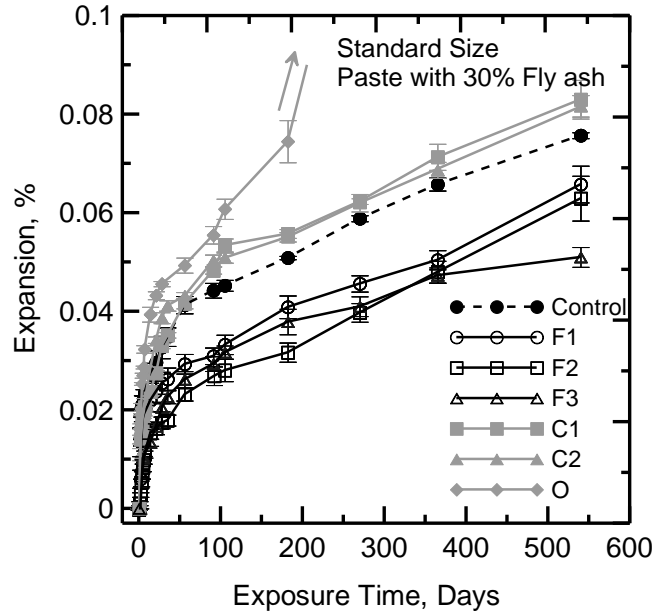


Figure 43. Expansion Curves for Standard Size Paste Specimens with 30 Percent Fly Ash.

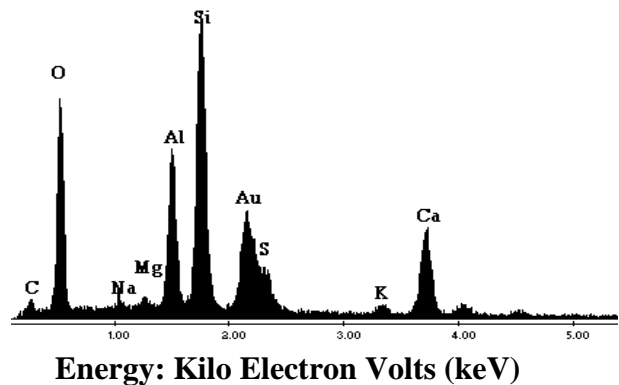
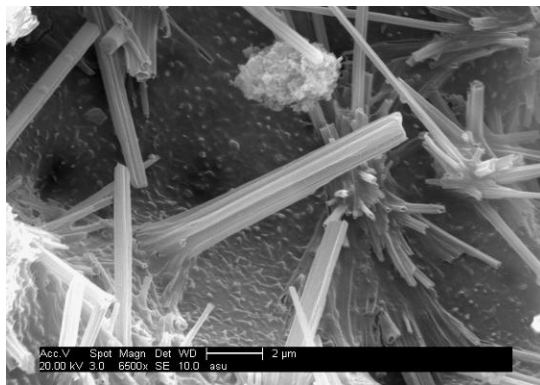


Figure 44. SEM Images and EDS Spectra for Ettringite Formation in Sulfate Attack.

Test methods followed the ASTM C1567 procedure to study the potential reduction of ASR in blended cements (ASTM, 2008). In this test method, 1-inch by 1-inch by 11-inch mortar bars were made with reactive aggregates with a specified grading, which were exposed to a normal sodium hydroxide (NaOH) solution at 176° F for 14 days, after 1 day of initial water curing at the same temperature. While different specifications specify different expansion limits, the aggregate-cementitious system usually is considered non-reactive if the expansion is less than

0.1 percent after 14 days of exposure. In our study, seven fly ashes with different compositions, including four class Fs (F1, F2, F3, and F4), one class C (C1), one natural pozzolan class N (N1), and one unqualified class C with a high SO₃ content (C2) were used. The results of the macroscopic linear expansion measurement of the mortar bars are presented in Figure 45. At a 30 percent replacement level, all the fly ashes, including the class C, showed expansions less than 1 percent and could be considered safe mixtures. The behavior of the blended cement systems followed almost the same trend after 14 days and up to 28 days of exposure. SEM and quantitative energy dispersive spectroscopy (EDS) are used in order to characterize the products of reaction that are responsible for the observed expansions as shown in Energy: Kilo Electron Volts (keV)

Figure 46.

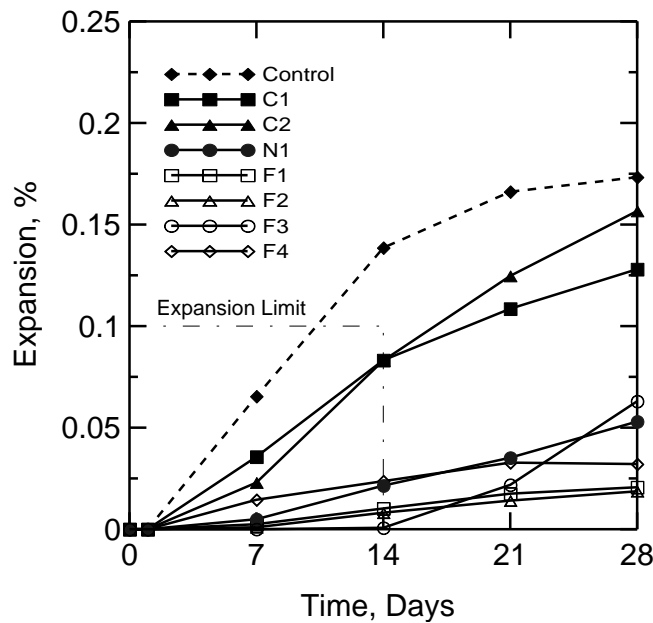


Figure 45. Effect of 30 Percent Fly Ash Replacement on ASR Expansion (ASTM 1567).

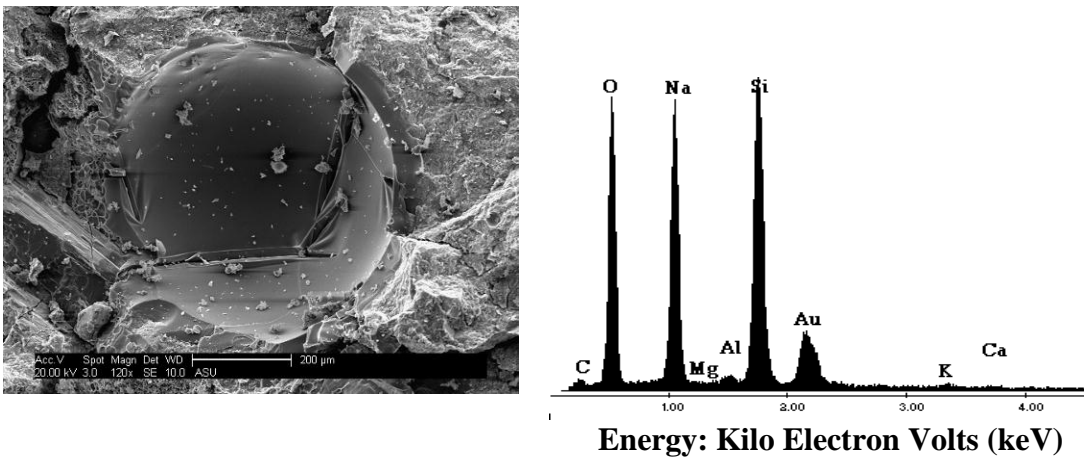


Figure 46. SEM for a Typical ASR Gel Formed in Control Specimen.

GUIDELINES FOR MATERIAL DESIGN

Many aspects of designing concrete structures are based on a single parameter—the compressive strength of concrete at 28 days of curing. There have been efforts to consider other properties in the design process, such as durability and energy absorption; this section discusses a few examples of serviceability-based designs.

The increasing use of concrete in hot climates has drawn attention to deleterious chemical processes, such as corrosion and alkali-aggregate reactions which are aggravated by high temperatures. The combined effects of cold winters and dry summer months should be considered in proportioning and production of durable concrete (American Concrete Institute, 2001). Suitable cementitious materials and properly proportioned concrete mixture produced under strict quality controls will be resistant to sulfates in soil or groundwater. Tables 27 through 29 show the required proportioning to resist sulfate attack and ASR. Although aggregates commonly are considered inert fillers in concrete, this is not always the case. Certain aggregates can react with alkalis in cement, causing expansion and deterioration. Carefully selecting aggregate sources and using low-alkali cement, pretested pozzolans, or ground slag will alleviate this problem. Table 28 shows the levels of allowable alkalinity. LBA is alkalinity of cement in pounds (lb), calculated by multiplying the cement content of the concrete in lb/yd^3 by the alkali content of the cement divided by 100. For example, for a concrete containing 500 lb/yd^3 of cement with an alkali content of 0.81% Na_2O_e the value of $\text{LBA} = 500 \times 0.81/100 = 4.05 \text{ lb/yd}^3$.

KGA is alkalinity of cement in kilograms (kg), calculated by multiplying the cement content of the concrete in kg/m^3 by the alkali content of the cement divided by 100. For example, for a concrete containing 300 kg/m^3 of cement with an alkali content of 0.91% Na_2O_e the value of $\text{KGA} = 300 \times 0.91/100 = 2.73 \text{ kg/m}^3$.

Table 27. Requirements to Protect against Damage to Concrete by Sulfate Attack (Takada et al., 1998).

Severity of Potential Exposure	Water-soluble Sulfate (SO_4)	Sulfate (SO_4) in Water, ppm	w/cm by Mass, max	Cementitious Materials Requirements
Class 0 Exposure	0.00 to 0.10	0 to 150	No special requirements for sulfate resistance	No special requirements for sulfate resistance
Class 1 Exposure	> 0.10 and < 0.20	> 150 and < 1500	0.50	C 150 Type II or equivalent
Class 2 Exposure	0.20 to < 0.20	1500 to < 10,000	0.45	C 150 Type V or equivalent
Class 3 Exposure	2.0 or greater	10,000 or greater	0.40	C 150 Type V plus pozzolan or slag

The spalling of concrete in bridge decks is a serious problem. The use of deicing salts causes corrosion in the reinforcing steel, which in turn produces an expansive force that causes the concrete to spall above the steel. Ample cover over the steel and the use of a low-permeability, air-entrained concrete will ensure durability in most cases, but more positive protection, such as

epoxy-coated reinforcing steel, cathodic protection, or chemical corrosion inhibitors, is needed for severe exposure conditions.

Table 28. Minimum Levels of Pozzolanic Replacement and Alkalinity that Will Provide Various Levels of ASR Prevention (Thomas, Fournier & Folliard, 2008).

Type of SCM	Alkali Level of SCM (%Na ₂ O*)	Minimum Replacement Level				
		Level W	Level X	Level Y	Level Z	Level ZZ
Fly Ash (CaO <18%)	< 3.0	15	20	25	35	See Table 7 in Henkensiefken et al., 2010
	3.0 – 4.5	20	25	30	40	
Slag	< 1.0	25	35	50	65	
Silica Fume (SiO ₂ > 85%)	< 1.0	1.2 x LBA or 2.0x KGA	1.5 x LBA or 2.5x KGA	1.8 x LBA or 3.0x KGA	2.4 x LBA or 4.0x KGA	

SCM = supplementary cementitious materials; LBA = alkalinity of cement in pounds (lb); KGA = alkalinity of cement in kg; other abbreviations are as previously defined

* %Na₂O equivalent = %Na₂O + 0.658 x %K₂O

Table 29. Allowed Alkali Contents to Provide Various Levels of ASR Prevention (Collins & Sanjayan, 1999).

Prevention Level	Maximum Alkali Content (%Na ₂ O*), lb/yd ³
V	No limit
W	5.0
X	4.0
Y	3.0
Z	See Table 7 in Henkensiefken et al., 2010
ZZ	

* %Na₂O equivalent = %Na₂O + 0.658 x %K₂O

Water permeability and gas permeability are two indicators of concrete transport properties and can be used for the prediction of concrete durability. Typical results for water permeability of concrete, reported by the Concrete Society, are as follows (Concrete Society, 1988):

- Dense (7,000 psi) concrete with slag and superplasticizer: 0.2 inches.
- Good quality concrete to resist aggressive environment: < 1.2 inches.
- Concrete in water-retaining structures: < 2 inches.

Requirements for a permeability index for different protection levels are presented in Table 30.

Table 30. Protective Quality Based on Autoclam Air Permeability Index (Basheer, 1993).

Protective Quality	Autoclam Air Permeability Index: Ln (Pressure)/min
Very Good	< 0.10
Good	> 0.10<0.50
Poor	>0.50<0.90
Very Poor	>0.90

Restrained Shrinkage Test (Ring Test)

To understand the effect of fiber addition in controlling shrinkage cracks, additions of 2.5, 5, 7.5, and 10 lb/yd³ of AR glass fiber were studied. The same sample size and constant high-temperature chamber as presented in Chapter 5 were used in this study. Four concrete mix designs were developed with a w/cm ratio of 0.55 and a slump of 2.5 to 3.5 inches. The mixture proportions of all mixes are shown in Table 31.

Four replicate ring specimens were made from each batch. The samples were kept in a laboratory environment and covered with sealed plastic sheets to be cured for 24 hours. After demolding, the top surfaces of the ring samples were sealed by a silicon rubber adhesive to protect the surfaces from losing any moisture.

Table 31. Mixture Proportions of the AR Glass and Control Samples (lb/ft³).

Mix ID	Control	ARG2.5	ARG5.0	ARG7.5
Portland Cement	43.5	43.5	43.5	43.5
Fine Aggregates	87	87	87	87
Water	23.9	23.9	23.9	23.9
AR Glass Fiber	0.0	0.095*	0.19*	0.28*
w/c	0.55	0.55	0.55	0.55
Aggregate/Cement	2.0	2.0	2.0	2.0

ARG2.5, ARG5.0, and ARG7.5 represent specimen labeling based on the amount of fiber addition in lb/yd³
* 0.095, 0.19, and 0.28 lb/ft³ are equal to 2.5, 5, and 7.5 lb/yd³

Response of Strain Gauges

The response from the strain gauge reading is recorded every minute. A typical plot from a strain gauge attached to steel ring for a plain concrete sample is shown in Figure 47. Three stages can be seen in the response of the strain gauge to the passing of time. The first stage (lasting 3 hours to less than 24 hours) shows the effect of rising temperatures and expansion of the steel ring due to the placement in a chamber. After the steel ring reaches the same constant temperature as the chamber, the strain gauge response reflects the effect of shrinkage in concrete at stage 2. In this stage, the response of the concrete cast around the steel ring is linear elastic. When the shrinkage strain in the concrete exceeds the strain corresponding to ultimate tensile strength, cracks initiate. The effect of stress relaxation due to concrete cracking is a sudden change in the strain recorded by the steel ring. This sudden shift in the strain gauge results shows that the timing of the cracking is due to the very low residual post-crack tensile strength in plain concrete. In stage 3, the strain in steel relaxes to approximately zero in the plain concrete sample. Visible crack width increases over time in this stage. The strain gauge's response can therefore be used to detect the time to cracking quite accurately. For example, in Figure 47, the concrete cracked at approximately 6 days.

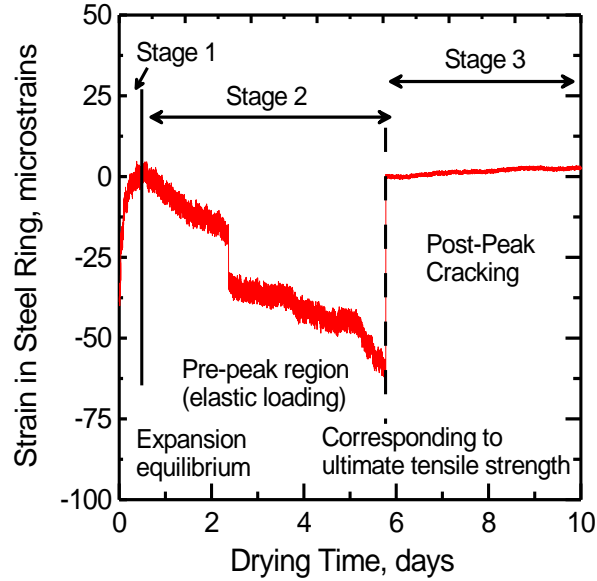


Figure 47. Typical Results Obtained Using a Strain Gauge Attached to a Steel Ring in a Plain Concrete Sample.

Responses of strain gauges for different mixtures are shown in Figure 48. The results clearly indicate that using AR glass fibers delays cracking in concrete samples for 1 or 2 days. According to the figure, only the control sample and ARG2.5 show an abrupt drop in strain gauge data due to cracking. Cracking happens between 6 and 8 days for all samples.

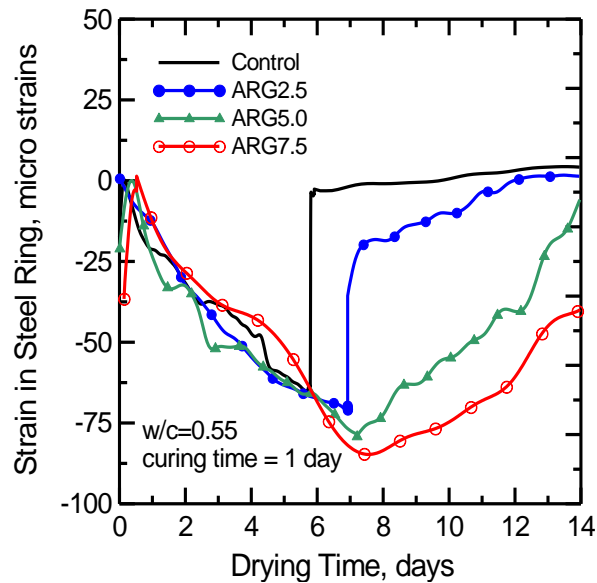


Figure 48. Effect of an AR Glass Fiber Addition on Results Obtained Using Strain Gauges Attached to Steel Rings.

Imaging Developed Cracks on Ring Samples

To measure crack width, digital images were taken and analyzed. Imaging was performed for all specimens after 14, 21, and 28 days of drying in the chamber. Since the average cracking time was 7 days, 14, 21, and 28 days were chosen as convenient measuring stages, since these time periods provided a sufficient amount of time for shrinkage cracks to extend and become visible. The samples were mounted on a traveling round plate and photographed with a 10x digital camera (Pulnix TM1325CL). This enabled the researchers to scan the entire surface of the specimen and examine it for new cracks, as well as allowing them to measure the widths of the existing cracks. A view of the digital camera when taking pictures of cracks of a concrete sample is shown in Figure 49. Figure 50 shows images of transverse shrinkage cracks in the control and ARG5.0 samples.



Figure 49. Digital Camera Used for Crack Investigations and Crack Width Measurement.

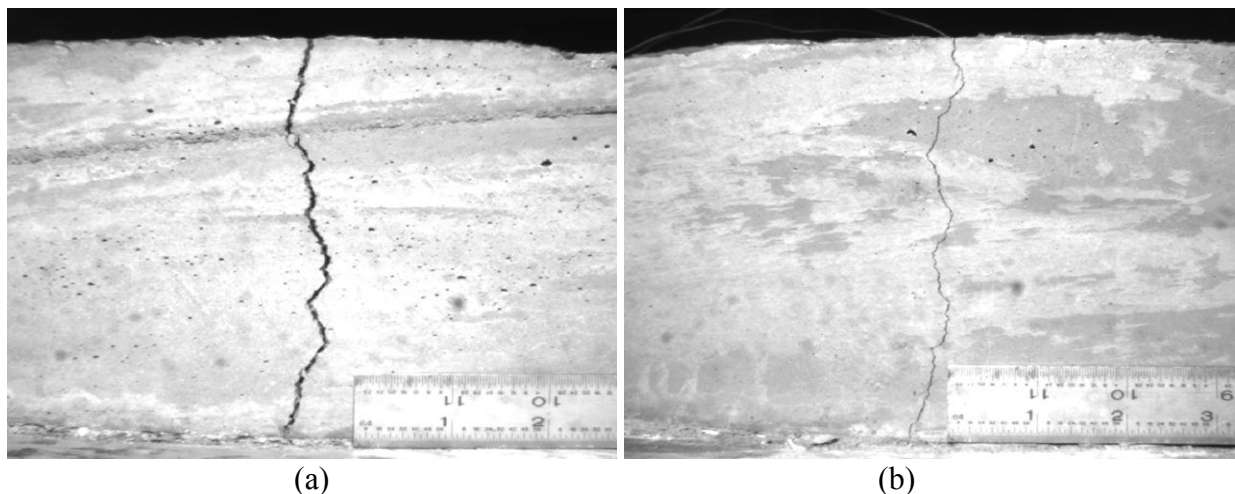


Figure 50. Transverse Cracks Caused by Restrained Drying Shrinkage on a) Control Sample and b) ARG5.0 Sample after Being Kept for 14 days in a Shrinkage Chamber.

The difference between the crack widths of the samples is obvious, but to take an accurate measurement, images were acquired along the crack length using a series of 8 to 12 photographs. To reconstruct the whole image, overlapping portions of images were cut off and images were attached along the crack length. Figure 51 shows that the crack width in the ARG5.0 sample is almost three times smaller than that in the control sample.

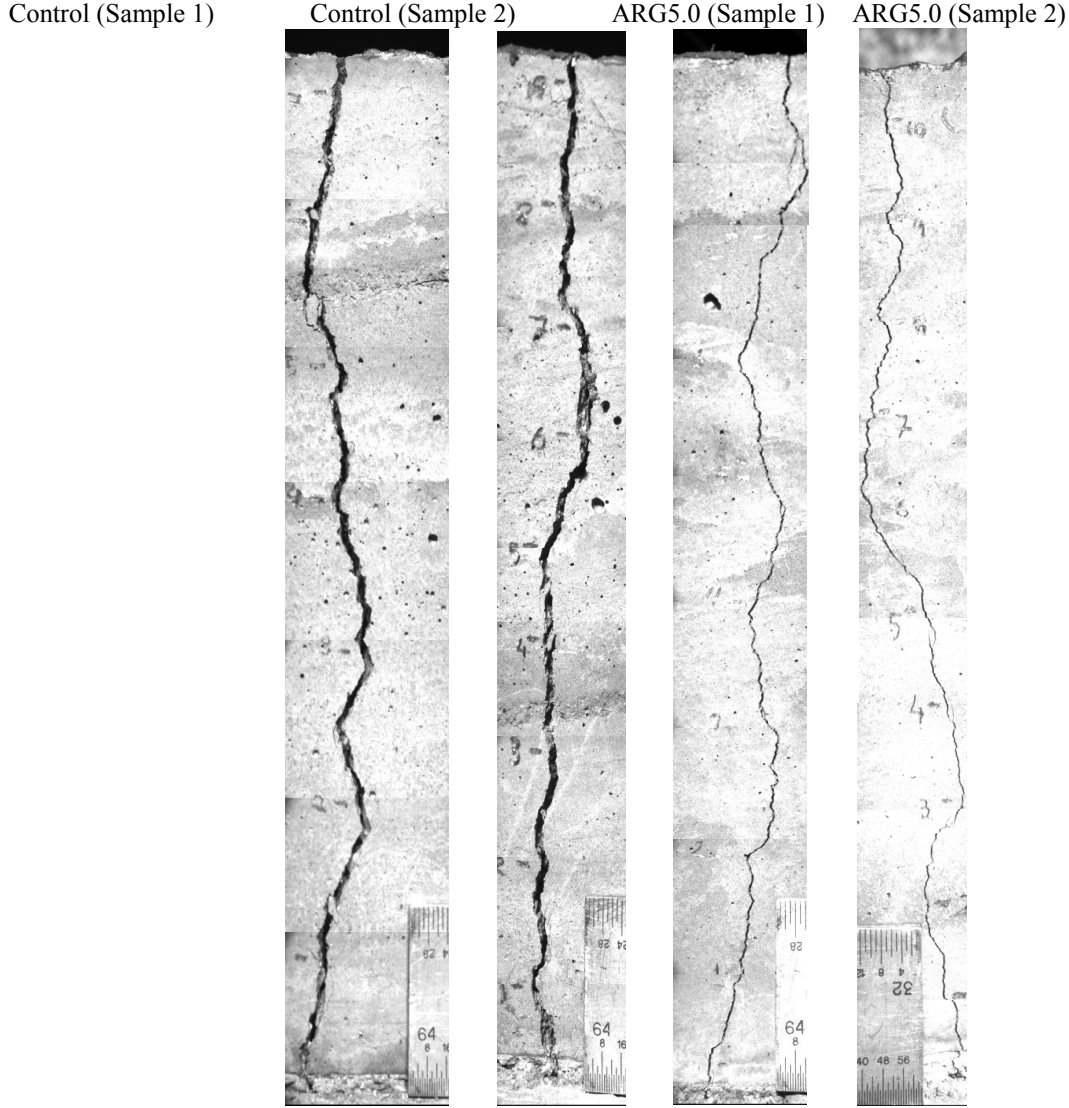
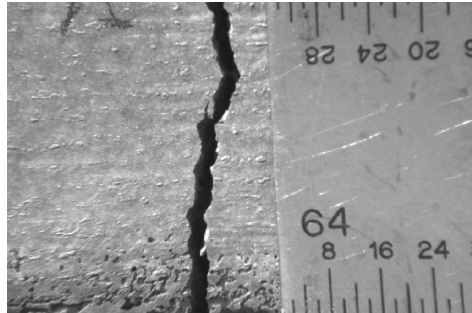


Figure 51. Reconstructed Shrinkage Crack Images of Control Group and ARG5.0 Samples.

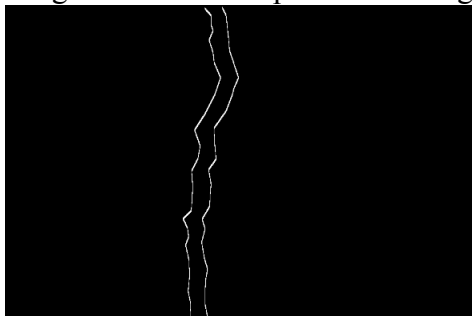
Image Analysis of Shrinkage Cracks

The aforementioned images were analyzed to measure the crack widths precisely. First, all of the images were converted from RGB color to an 8-bit format. Then, a MATLAB code was developed to read the 8-bit images, which asked the user for the scale factors and crack boundaries. The program then made a binary image (black and white) of the crack boundaries. In the next step, the crack width was measured automatically in pixel units at 64 different lines perpendicular to the crack length. The pixel results were converted to the real distance using an

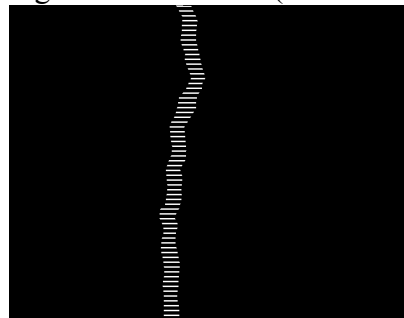
appropriate scale factor. Finally, the code calculated mean crack widths, standard deviations, and statistical analysis graphs, including crack width histograms and probability densities. Figure 52 shows the image analysis processes and output statistical results.



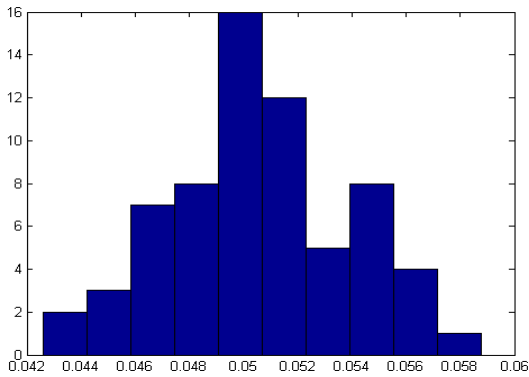
a) A grey image of the crack represented using an eight-bit resolution (256 intensity levels)



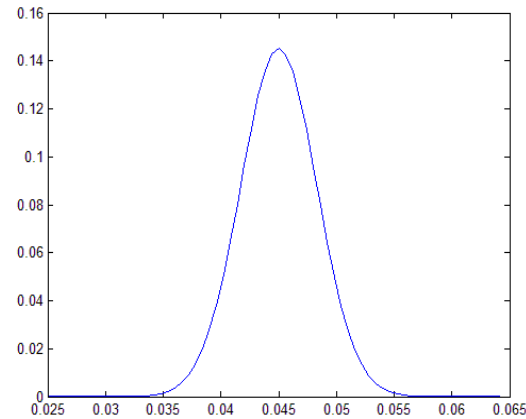
b) Binary image of crack



c) Crack width measurement using 64 line segments



d) Crack width histogram



e) Crack width probability density function

Figure 52. Steps in the Analysis of 1 of 8 Images Taken along the Bottom Side of a Crack.

To report the crack width of a sample, an average of crack width values was obtained from 8 to 12 discrete images along the crack length. Standard deviations of mean crack values also were calculated and reported. The crack widths and standard deviations of all mixtures are shown in Table 32. The results show that crack width dimension increased in all mixtures by increasing the drying time. The effect of adding fiber is significant in that it dramatically reduced crack width dimensions. By adding 2.5, 5, and 7.5 lb/yd³ AR glass fibers to plain concrete, the crack width dimensions at 14 days were reduced by 51, 72, and 82 percent, respectively. The same trend was observed after 21 and 28 days of drying in the shrinkage chamber.

Table 32. Mean Crack Width and Standard Deviation of Samples after 14, 21, and 28 Days.

Sample Code	Crack Width at 14 Days, in		Crack Width at 21 Days, in		Crack Width at 28 Days, in	
	Average	Standard Deviation	Average	Standard Deviation	Average	Standard Deviation
Control – Sample 1*	0.0460	0.0037	0.0575	0.0031	-	-
Control – Sample 2*	0.0451	0.0026	0.0562	0.0058	-	-
Control – Sample 3	0.05039	0.0025	0.0604	0.0033	0.0686	0.0027
Control – Sample 4	0.04003	0.0021	0.0471	0.0018	0.0537	0.0024
Control – Average	0.0454	0.0042	0.0553	0.0057	0.0611	0.0105
ARG2.5 – Sample 1	0.0134	0.0041	0.0185	0.0066	0.0208	0.0041
ARG2.5 – Sample 2	0.0217	0.0004	0.0277	0.0024	0.0324	0.0018
ARG2.5 – Sample 3	0.0135	0.0016	0.0154	0.0009	0.0192	0.0019
ARG2.5 – Sample 4	0.0391	0.0019	0.0468	0.0016	0.0483	0.0019
ARG2.5 - Average	0.0219	0.0121	0.0271	0.0141	0.0302	0.0134
ARG5.0 – Sample 1*	0.0143	0.0018	0.0175	0.0008	-	-
ARG5.0 – Sample 2*	0.0127	0.0018	0.0159	0.0018	-	-
ARG5.0 – Sample 3	0.0131	0.002	0.0168	0.0029	0.0208	0.0016
ARG5.0 – Sample 4	0.0096	0.0015	0.0137	0.0017	0.0189	0.0018
ARG5.0 – Average	0.0124	0.0020	0.0160	0.0017	0.0198	0.0013
ARG7.5 – Sample 1	0.0090	0.0013	0.0121	0.0013	0.0152	0.0015
ARG7.5 – Sample 2	0.0085	0.0019	0.0118	0.0008	0.0138	0.0008
ARG7.5 – Sample 3	0.0062	0.0011	0.0086	0.0006	0.0097	0.0010
ARG7.5 – Sample 4	0.0045	0.0010	0.0068	0.0017	0.0090	0.0008
ARG7.5 - Average	0.0070	0.0021	0.0098	0.0026	0.0119	0.0030

* Crack widths in these samples were not measured at 28 days.

As shown in Table 32 and in Figure 53, the standard deviation of the ARG2.5 mixture is much higher than that of the control samples and the other mixtures. It seems that the AR glass fiber content of 2.5 lb/yd³ is not enough to ensure cracking control. Meanwhile, the addition of 5 lb/yd³ AR glass fibers to the mixture results in a much lower variation in the results and reduces the crack width dimension by 70 percent.

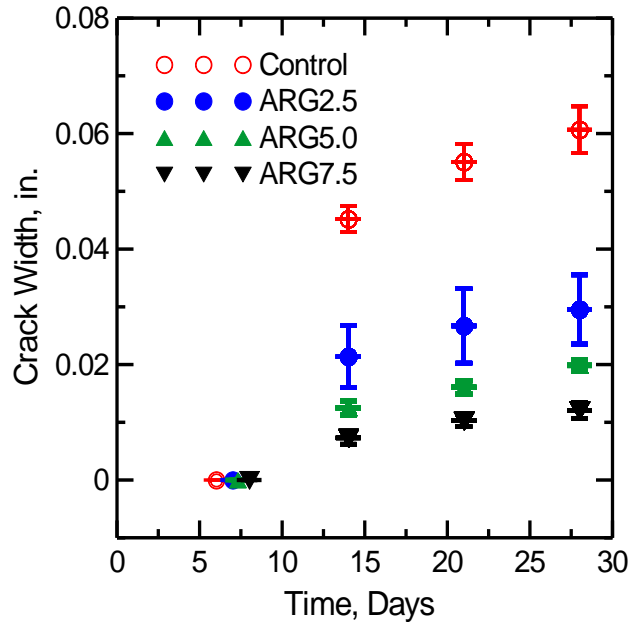


Figure 53. Mean and Standard Deviations of Shrinkage Crack Width of All Mixtures.

CHAPTER 7. PROCEDURES FOR STATISTICAL QUALITY CONTROL

INTRODUCTION

Statistical process control provides information about variations in the manufacturing process, and it allows one to understand and, when possible, improve the efficiency of concrete production, delivery, and construction. QC methods are implemented to monitor the change or shift in the mean or variation of a manufacturing process. These methods have been applied to the cement manufacturing process, and their use can be extremely beneficial in monitoring the delivery and construction of concrete. This chapter presents information about the economical design of concrete materials using hybrid control charts for active control and monitoring of concrete strength (Laungrungrong et al., 2010).

One of the critical environmental quality measures influenced by concrete production is CO₂ emissions. According to a Portland Cement Association report, by 2020, the industry aims to reduce CO₂ emissions by 10 percent from the 1990 baseline levels (Portland Cement Association, 2009). This chapter outlines a three-part strategy to achieve this goal:

- Improve energy efficiency by upgrading production plants with state-of-the-art equipment.
- Improve product formulation to reduce manufacturing energy consumption and minimize the use of natural resources.
- Conduct research and develop new applications for cement and concrete that improve energy efficiency and durability.

Control charts can be implemented to monitor the process and, when sufficient historical data become available, manufacturers can obtain better insight into operational procedures. They may be instrumental in monitoring concrete strength data and optimizing the operating process by identifying potential problems that may exist. A process typically operates under normal conditions (i.e., in control) and produces a product that satisfies the minimum specified strength. However, a change in normal operating conditions may cause the process to go out of control. An out-of-control process eventually will produce compressive strengths that no longer meet the minimum specified strength. The out-of-control condition may be caused by low-quality material, operator errors, or production changes. It is desirable to detect when this change occurs and identify what caused the process to go out of control, so that operators can take corrective action. If an assignable cause is not corrected, the process will continue to operate out of control, resulting in a significant degradation of the material and a significant percentage of product that is unacceptable for use.

There are several approaches for assessing the quality of concrete. Sykora recommended a standard deviation and coefficient of variation corrected for testing error to determine the uniformity of the concrete strength (Sykora, 1995). This method is useful for comparing variations within a plant but is not recommended for comparing variation from plant to plant. Leshchinsky suggested a metric that is a combination of two or more methods to improve the reliability and accuracy of concrete quality (Leshchinsky, 1991). Soroka focused on designing

the test scheme of concrete (Soroka, 1968). The minimum strength and sample size (n) can be chosen to achieve the acceptable producer's risk (rejecting "good" concrete) and consumer's risks (accepting "poor" concrete). The minimum strength can be estimated by three degrees of control based on the maximum values of the coefficient of variation—good (0.12), fair (0.2), and poor (0.3 or more). A sample size of $n = 9$ was recommended as a maximum practical sample size. If the sample size is increased, the risks are decreased. However, results indicate that increasing the sample size to $n = 15$ (not practical) is not enough to reduce a producer's risk to 10 percent. It was determined that the sample size and the minimum strength must be adjusted simultaneously to attain acceptable producer and consumer risks.

A CUSUM control chart for individual observations can be used to monitor concrete strength. The Cement and Concrete Institute proposed three different CUSUM charts for monitoring the mean strength (CUSUM M), mean range strength (CUSUM R) where the target mean range is determined by the value of standard deviation, and the correlation between predicted and actual strengths (CUSUM C) (Brown, 1984). Day recommended using the mean strength as the target value in the CUSUM chart (Day, 2006). The CUSUM control chart is used to distinguish between a significant change (real change in slope) and non-significant change (error of aberration).

ACI 214 provides examples of applying the CUSUM chart and discusses some of the difficulties with the CUSUM analysis (American Concrete Institute Committee 214, 2002). The ACI test method also notes that the CUSUM statistic is sensitive to the target (or the mean strength) and that different methods for estimating the average (mean) strength can lead to misleading conclusions. The average strength should be calculated separately for each project since different jobs and suppliers will affect the average strength calculation. Chen et al. proposed two indices (fitness and stability) for evaluating the quality of concrete production (Chen, Sung & Shih, 2005). A single QC level chart for concrete can be constructed using these two indices. The proposed method is easy to implement and applicable for comparing more than two manufacturers at the same time.

Statistical analyses were conducted to evaluate the nature of compressive strength of concrete as it is used in specifications for acceptance and/or rejection of samples. The proposed approaches are based on using control charts in the evaluation of variations in the test results. By combining the CUSUM control chart and a CUSUM-run chart, or an EWMA control chart and an EWMA-run chart, it is believed that early detection of shifts in the process mean becomes possible. The combined charts address both the consumers' and the producers' perspectives. The consumer can make a decision about accepting or rejecting a strength test. In addition, the concrete manufacturer can use the chart to determine if the monitored process is out of control, and it provides an opportunity to identify the possible causes for the situation.

By identifying the assignable causes of the out-of-control processes, the producer can then improve the manufacturing process by reducing product variation, unnecessary waste, or over-designed concrete mixtures. The CUSUM-run chart also can quickly indicate if the strength is less than the minimum acceptable level. Any delay in detection of unacceptable strength can result in additional penalties, project delays, and increased associated costs.

STATISTICAL ANALYSIS FOR QUALITY ASSURANCE

Control charting is widely used to monitor and improve process performance in manufacturing industries. Montgomery suggested that, in a general manufacturing process, the CUSUM chart or the EWMA control chart is more efficient as a moving average control tool in detecting small process shifts (1.5σ or less) in comparison to Shewhart control charts (Montgomery, 2008). The CUSUM and EWMA control charts often behave similarly in practice, although different weight functions can be applied to current and recent past data values.

The CUSUM method applies a constant weight factor to the entire historical set of data, whereas in the EWMA method, there is an exponential weight factor applied to the data, which gives current or recent past observations more weight than older data values. The proposed methodology evaluates compressive concrete strength using the combination of either the CUSUM or EWMA control chart with a standard run chart. The combination of a CUSUM (or EWMA) chart and a run chart was explored to determine the best conditions (i.e., the appropriate values of control variables) for monitoring concrete strength. The performance of the CUSUM-run chart and the EWMA-run chart were compared to determine which chart is more useful for the concrete industry.

Run Charts

The run chart is a graphical display of data points plotted by time, and it can be useful for monitoring individual strength data in concrete strength studies. The run chart focuses on process variability as a function of time or sampling point, and it graphically presents the stability of the process variation over time. Upward or downward shifts or trends in the process often will be visible on a run chart (Feigenbaum, 1991; George, 2002).

A horizontal line representing the minimum specified concrete strength (f'_c) can be added to the run chart and is useful for identifying unacceptable or unqualified concrete samples. For example, concrete is considered unqualified or unacceptable for use if an individual data value (concrete strength) has not reached or surpassed the f'_c line. The run chart plots data in its natural units of measure, which makes it easy to interpret. However, the run chart alone may not indicate an out-of-control or unstable process. As a result, the run chart should be combined with a monitoring scheme that provides information about the stability of the process.

Cumulative Sum Control Chart

Page introduced CUSUM plots where the cumulative sum is the sum of the deviations of the sample measurement (such as an individual observation or average of several observations) from a target (product specification) (Page, 1954). The general form of the cumulative sum is as follows:

$$C_i = \sum_{j=1}^n (x_j - \mu_0) \quad (\text{Eq. 31})$$

where C_i is the sum of the deviations from target for all observations up to and including the i th observation, x_j represents the i th observation, μ_0 is the target value, and n is the number of observations.

A deviation above the target is called a one-sided upper cusum (C^+), and a deviation below the target is called a one-sided lower cusum (C^-). The one-sided CUSUMs, which are plotted on a CUSUM chart, are as follows (Montgomery, 2008):

$$\begin{aligned} C_i^+ &= \max[0, x_i - (\mu_0 + K) + C_{i-1}^+] \\ C_i^- &= \max[0, (\mu_0 - K) - x_i + C_{i-1}^-] \end{aligned} \quad (\text{Eq. 32})$$

The initial CUSUM values are $C^+_0 = C^-_0 = 0$. The constant, K , is called the reference value and is calculated as $K = (|\mu_1 - \mu_0|)/2$ where μ_0 is the target mean and μ_1 is the out-of-control mean that the user wishes to detect. If the exact out-of-control mean is unknown, the user can let $K = k\sigma$, where σ is the process standard deviation and k is a constant chosen so that a particular shift is detected. For example, if it is important to detect a shift from target of 1.5 standard deviation (i.e., detect if the target has shifted to $\mu_0 + 1.5\sigma$ or $\mu_0 - 1.5\sigma$). Then $k = 1.5$ and $K = 1.5\sigma$. If the process standard deviation is not known, it can be estimated from the sample data.

The statistics C^+_i and C^-_i are plotted on the CUSUM chart. If C^+_i or C^-_i exceeds a predetermined decision value, H , it signals that the process is out of control. H is not arbitrary and should be chosen after careful consideration. H is defined as $H = h\sigma$, where h is selected after k is chosen. Commonly, $H = 4\sigma$ ($h = 4$) or $H = 5\sigma$ ($h = 5$). The choice of H in combination with the value of K often is made with respect to appropriate average run lengths (which will be discussed later in this report). For more discussion on the design of CUSUM charts, see Hawkins (1993) and Woodall & Adams (1993).

To illustrate the CUSUM method, consider simulated data consisting of two different sets of random responses. The two data sets differ only by an imposed change in the mean value of the population density. Suppose the target value is $\mu_0 = 3,500$ psi and we would like to detect of shift of one standard deviation (1.0σ). We simulate 20 observations, with the first 10 observations generated from a normal distribution with an in-control mean $\mu = 3,500$ psi and standard deviation $\sigma = 50$ psi. We then generate the remaining 10 observations with the mean for the out-of-control process. That is, the out-of-control mean is given by $\mu_1 = \mu_0 + \delta\sigma = 3,500 + 1(50) = 3,550$ (the standard deviation of the remaining 10 observations is still $\sigma = 50$). The value of K is $|\mu_1 - \mu_0|/2 = 25$. To define the range of variability, a variability scaling factor h is defined, and using value of $h = 4$ will result in $H = h\sigma = 200$. Our decision will be to assume the process has shifted out of control if any of our CUSUM values lie outside the decision value, $H = 200$.

Table 33 lists the lower and upper CUSUMs, C^+_i and C^-_i , and the CUSUM control chart is displayed in Figure 54. In this example, observation 12 ($C^+_{12} = 205.38$) is greater than $H = 200$. Thus, an out-of-control signal is detected. In other words, the CUSUM chart has detected the shift in the process mean within four samples after the shift has occurred. In this study, we want to simplify the plot by adding the negative sign in front of any numbers related to the lower-sided CUSUM (for graphical purpose only). We use both the positive and negative of the

decision value H (i.e., set $H^+ = 200$ and $H^- = -200$). For example, Period 4 from Table 33, $C_3^+ = 17.29$, but C_3^- will be set to -17.29 in the CUSUM plot as shown in Figure 54.

The process is considered to be out of control if any of the statistics plot beyond the decision value. If an out-of-control point is observed, a search for an assignable cause is in order. Montgomery noted that assignable causes may be due to problems including but not limited to equipment, process steps, operators, or materials (Montgomery, 2008). An out-of-control process can result in unstable and inaccurate results if no corrective action is taken. If an assignable cause can be identified, then it is possible to eliminate the problem and return the process to a state of statistical control. For the CUSUM control chart, if the process is in statistical control the user can, after some adjustment, decide whether to reset the one-sided upper and lower CUSUMs to zero ($C_i^+ = 0$ or $C_i^- = 0$). If the CUSUMs are reset after an out-of-control signal is detected, any possible bias resulting from the previous out-of-control process may be removed, and the process will continue to operate in control. However, if the statistics C_i^+ or C_i^- are not reset to zero after a corrective action, then it is possible that a shift in the process in the opposite direction may not be detected.

Continuing the previous example, the statistics C_i^+ and C_i^- are recalculated after setting the initial statistics to zero after the detection of an out-of-control signal. The results of these signals are then shown in the fifth and eighth columns in Table 33. The first out-of-control signal is detected at the 12th period for the upper CUSUM, so that $C_{12}^+ = 205.38$ will reset to $C_{12}^+ = 0$ for the next calculation. The C_{13}^+ can be computed using Equation 32 and is given as:

$$\begin{aligned} C_{13}^+ &= \max [0, x_i - (\mu_0 + K) + C_{12}^+] \\ &= \max [0, 3555.06 - (3500 + 25) + 0] = 30.06 \end{aligned}$$

The CUSUM chart based on the C_i^+ with resetting method signals three times at observation 12 ($C_{14}^+ = 205.38$), observation 17 ($C_{17}^+ = 258.56$), and observation 20 ($C_{20}^+ = 213.33$), in comparison to the 9 signals detected by the CUSUM chart without resetting (observations 14 through 20). There is no difference for the lower-sided CUSUMs, C_i^- , since no out-of-control situation has occurred. Figure 54 shows a comparison of the CUSUM chart with and without resetting.

Table 33. Sample Calculations of CUSUM with and without Resetting after an Out-of-control Signal Is Detected.

No. (i)	x_i	CUSUM					
		Upper			Lower		
		$x_i - 3525$	C_i^+	C_i^+ with Zero	$3475 - x_i$	C_i^-	C_i^- with Zero
1	3556.68	31.68	31.68	31.68	-81.68	0	0
2	3527.37	2.37	34.05	34.05	-52.37	0	0
3	3457.71	-67.29	0	0	17.29	17.29	17.29
4	3568.66	43.66	43.66	43.66	-93.66	0	0
5	3491.15	-33.85	0	0	-16.15	0	0
6	3472.99	-52.01	0	0	2.01	2.01	2.01
7	3498.84	-26.16	0	0	-23.84	0	0
8	3546.13	21.13	21.13	21.13	-71.13	0	0
9	3506.11	-18.89	0	0	-31.11	0	0
10	3458.85	-66.15	0	0	16.15	16.15	16.15
11	3640.46	115.46	115.46	115.46	-165.46	0	0
12	3614.92	89.92	205.38	205.38	-139.92	0	0
13	3555.06	30.06	235.44	30.06	-80.06	0	0
14	3540.1	15.1	250.54	45.16	-65.1	0	0
15	3640.84	115.84	366.38	161	-165.84	0	0
16	3557.61	32.61	398.99	193.61	-82.61	0	0
17	3589.95	64.95	463.94	258.56	-114.95	0	0
18	3588.34	63.34	527.28	63.34	-113.34	0	0
19	3568.54	43.54	570.82	106.88	-93.54	0	0
20	3631.45	106.45	677.27	213.33	-156.45	0	0

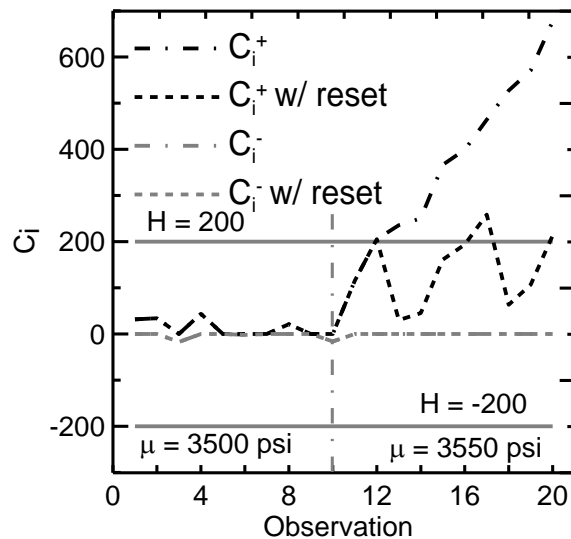


Figure 54. Comparison of the CUSUM Chart for Table 33 with Resetting (C_i^+ w/reset and C_i^- w/reset) and without Resetting (C_i^+ and C_i^-) When an Out-of-control Signal Is Detected.

Exponentially Weighted Moving Average Control Chart

Roberts proposed the EWMA control chart (Roberts, 1959). The EWMA statistic is calculated as follows:

$$z_i = \lambda x_i + (1 - \lambda) z_{i-1} \quad (\text{Eq. 33})$$

where λ ($0 < \lambda \leq 1$) is a weight assigned to the most current observation, x_i is the current observation, and z_{i-1} is the previous EWMA statistic with $z_0 = \mu_0$. If the process target, μ_0 , is not known, then the process mean can be used as the initial value. Using recursive substitution for z_{i-1} , Equation 33 can be rewritten as:

$$z_i = \lambda \sum_{j=0}^{i-1} (1 - \lambda)^j x_{i-j} + (1 - \lambda)^i z_0 \quad (\text{Eq. 34})$$

with $\lambda \sum_{j=0}^{i-1} (1 - \lambda)^j$ weights defined as:

$$\lambda \sum_{j=0}^{i-1} (1 - \lambda)^j = \lambda \left[\frac{1 - (1 - \lambda)^i}{1 - (1 - \lambda)} \right] = 1 - (1 - \lambda)^i \quad (\text{Eq. 35})$$

As a result, the limiting form given in Equation 35 includes information from past observations as well as the most current observation, x_i . To illustrate, consider the same data set used previously in the CUSUM example. Based on the function described in Equation 35, a value of $\lambda = 0.1$ indicates that the weight assigned to the current observation (x_i) is 0.1, and that the weight assigned to the previous observations are 0.09 (x_{i-1}), 0.081 (x_{i-2}), 0.0729 (x_{i-3}), and so on. The EWMA values, z_i , for this illustration are provided in the last column in Table 34. Figure 55 displays the plot of the EWMA control chart, with the weights of the previous mean values shown in the inset. The EWMA control chart consists of a center line and upper and lower control limits. The center line is the process target (or the process mean). The center line (CL) and upper and lower control limits (*UCL* and *LCL*) are defined as follows:

$$\begin{aligned} UCL &= \mu_0 + L\sigma \sqrt{\frac{\lambda}{2 - \lambda} [1 - (1 - \lambda)^{2i}]} \\ CL &= \mu_0 \\ LCL &= \mu_0 - L\sigma \sqrt{\frac{\lambda}{2 - \lambda} [1 - (1 - \lambda)^{2i}]} \end{aligned} \quad (\text{Eq. 36})$$

where L is a multiple of the standard deviation chosen to attain a certain average run length. If one or more z_i values fall beyond the upper or lower control limits, then the process is considered to be out of control.

In summary, the EWMA control chart or the CUSUM control chart can be used to monitor a process. For the EWMA control chart, Roberts suggested replacing x_i with \bar{x}_i in Equation 33

(Roberts, 1959). Montgomery also recommended replacing by $\sigma_{\bar{x}} = \sigma/\sqrt{n}$ where n is the subgroup size ($n > 1$) for both the CUSUM and EWMA charts (Montgomery, 2008). It is worth noting that, since the EWMA statistic is a function of weighted values, the normality assumption is not critical, whereas the CUSUM is sensitive to this assumption.

Table 34. Sample Calculations of EWMA Chart (All Values Are in psi).

No.	x_i	EWMA Zi ($\lambda=0.1$)
1	3556.68	3505.67
2	3527.37	3507.84
3	3457.71	3502.83
4	3568.66	3509.41
5	3491.15	3507.58
6	3472.99	3504.12
7	3498.84	3503.6
8	3546.13	3507.85
9	3506.11	3507.67
10	3458.85	3502.79
11	3640.46	3516.56
12	3614.92	3526.4
13	3555.06	3529.26
14	3540.1	3530.35
15	3640.84	3541.39
16	3557.61	3543.02
17	3589.95	3547.71
18	3588.34	3551.77
19	3568.54	3553.45
20	3631.45	3561.25

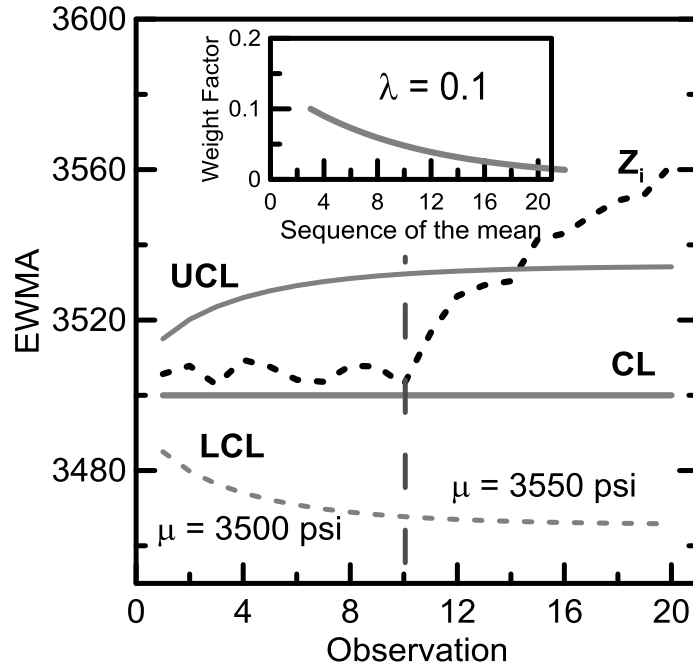


Figure 55. EWMA Chart for the Data (CL = Control Limit, UCL =Upper Control Limit, and LCL = Lower Control Limit) in Table 34.

Average Run Length

The average run length (ARL) can be used to analyze the statistical performance of control charts. ARL is defined as the average number of samples observed before the process signals out of control. The ARL can be used to evaluate the performance of the control chart or to determine the appropriate values of various parameters for the control charts presented. If the process is in control, but the control chart gives an out-of-control signal, then this signal is considered a false alarm. According to Woodall, an optimal detection algorithm has a large in-control ARL and a small out-of-control ARL (Woodall, 1985). For example, to determine the most appropriate values of λ and L for the EWMA chart, the acceptable value of the ARL and the magnitude of the shift in process mean (multiple of σ) can be stated, and then λ and L can be determined for a particular situation. Crowder proposed a different set of optimal parameters for a two-sided EWMA chart, which are reported in Table 35 (Crowder, 1987). The values of λ are set at 0.05, 0.1, 0.5, and 1.0, and the ranges of L are 2, 2.5, 3, and 3.5. The shift sizes vary from 0, 0.25, 0.5, and 1.0 (in terms of multiples of σ).

Table 35. ARL Performance of the Two-sided EWMA Control Chart with Varying L , λ , and Shift Size.

λ	Shift Size	$L=2$	$L=2.5$	$L=3$	$L=3.5$
0.05	0	127.53	379.4	1,379.35	6,464.6
	0.5	18.97	26.64	37.37	4.56
	1	8.38	10.79	13.51	16.6
0.1	0	73.28	223.35	842.15	4,106.29
	0.5	15.53	23.63	37.41	64.72
	1	6.62	8.75	11.38	14.79
0.5	0	26.45	91.17	397.56	2,227.34
	0.5	11.89	27.16	75.35	267.36
	1	4.91	8.27	15.74	35.97
1	0	21.98	80.52	370.4	2,149.34
	0.5	13.7	41.49	155.22	723.81
	1	6.25	14.92	43.89	160.95

For the CUSUM control chart, the ARL is determined by the parameters H and K . Hawkins recommended that the approximation for the ARL of CUSUM control chart (accurate to within 3 percent) can be obtained by (Hawkins, 1992):

$$ARL = \frac{1}{\Phi(-Y_{hk})} \quad (\text{Eq. 37})$$

Mandel proposed the model $Y_{hk} = \alpha_h + \beta_k + \zeta_h \eta_k + \zeta_h^* \eta_k^*$ (Mandel, 1969). The parameter Φ is defined as the cumulative normal distribution (i.e., $\Phi(p)$) and is the standard normal value that has area p to the left. All coefficients are calculated by weighted least squares. The coefficients α_h , ζ_h , and ζ_h^* are based on the value of h , whereas the coefficients β_k , η_k , and η_k^* depend on k . The range of h is between 0 and 9, and k varies between -2 to 3. To study the behavior of ARL, the CUSUM charting is explored using several scenarios. The ARL values for the one-sided CUSUM scheme are shown in Table 36.

Table 36. ARL Performance of the One-sided CUSUM with Various Values of k and h and with No Mean Shift.

h	k	ARL
5	0	37.5
5	0.25	142.3
5	0.125	67.6
5	0.5	942.6
4	0	26.4
4	0.25	77.1
4	0.125	42.8
4	0.5	339.2
3	0	17.3
3	0.25	39.3
3	0.125	25.3
3	0.5	117.7
2	0	10.1
2	0.25	18.1
2	0.125	13.3
2	0.5	38
1	0	4.8
1	0.25	7.1
1	0.125	5.8
1	0.5	11.2

PRELIMINARY STUDY OF HISTORICAL DATA

A preliminary study of approximately 300,000 yd³ of concrete delivered in different strength categories for a single concrete manufacturer obtained from ADOT’s Field office Automation SysTem (FAST) database is illustrated in Figure 56. The minimum specified compressive strength is plotted against the actual strength of concrete delivered to the job site. The actual strength of each data point is calculated as the average of two compressive strength values, which are obtained from a delivery lot of 50 yd³ of concrete. The solid line plotted in Figure 56 represents a correlation between specified and actual strengths. Most of the data are plotted above this line. Thus, the actual strength delivered exceeds that required by the job by 1,100 to 1,500 psi. Reducing the average and/or standard deviation of the cement strength in the mixture could control these observed differences in the cement strength. Optimizing the process (i.e., reducing the mean strength and the excessive variability) can have a significant impact on both the pay factor and sustainability. In particular, if the natural variability in compressive strength is better understood as a process, more informed (and less reactive) decisions about the acceptability of the lot will be made. This, in turn, can result in using less concrete, which would have a significant impact on environmental quality measures (such as CO₂ emissions).

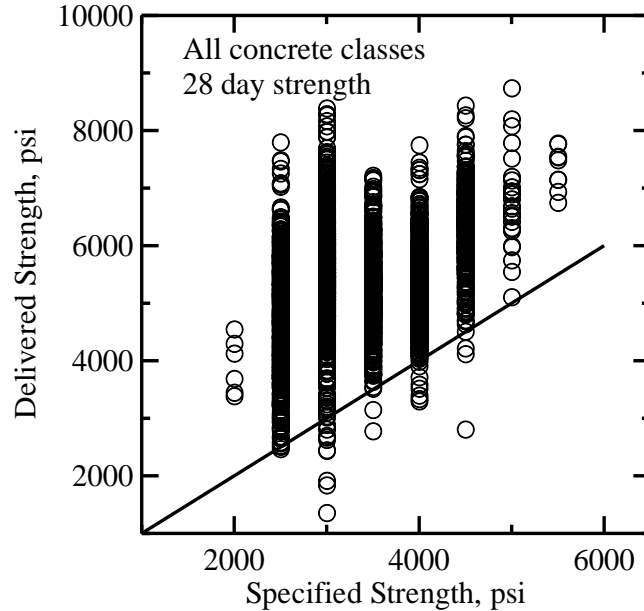


Figure 56. Correlation of Data Representing the Specified Strength of Concrete Delivered to a Job Site for a Single Ready-mix Producer. The Solid Line Represents a 1-to-1 Correlation.

The proposed combined control charts are applied to historical data given for various projects. The compressive strength data in the test case were chosen randomly from the ADOT FAST database. Five different concrete suppliers were chosen and, for each ready-mix supplier, two different plants were selected. For each plant, three separate mix specifications were selected. The researchers then studied the design histories for 28-day concrete strength supplied from these plants. Compressive strength test data from five bridge projects also were selected randomly and are shown in Table 37.

For all selected projects, the concrete strength data were collected from a rational subgroup and were not subject to individual observation. Typically, both CUSUM and EWMA charts are used with an individual observation. An individual observation can be replaced by the subgroup mean. Using subgroups of observations and calculating the sample mean (where the sample mean is used as the individual observation) are both valid as long as the subgroup data are similar for the CUSUM chart and EWMA chart (Roberts, 1959; Hawkins & Olwell, 1998). Montgomery also suggested replacing σ with $\sigma_{\bar{x}} = \sigma/\sqrt{n}$ (where n is size of subgroup) (Montgomery, 2008).

For the data collected from the ADOT projects, four of the projects (labeled B12, B23, D22, and D23) consist of varying sample sizes and would have required a different type of control chart to account for the varying sizes. As a result, they were removed from the study. Three projects (A12, C23, and D22) were removed from the study due to the extremely small sample sizes (containing five or fewer data points).

Table 37. Test Case Data Sets.

Project No.	f'_c	$\hat{\mu}$	$\hat{\sigma}$	N	AD	P
A11	3000	4696	132	7	0.25	0.63
A12	2900	4045	27	2	0.25	0.23
A13	2500	4001	110	11	0.45	0.23
A21	3000	5298	101	50	1.05	0.01
A22	2500	4435	109	59	1	0.01
A23	3000	4933	135	146	0.7	0.07
B11	3500	5092	185	19	0.74	0.04
B12⁺	4000	4788	186	6	0.63	0.05
B13	4500	6252	173	21	0.34	0.45
B21	3000	4523	157	8	0.24	0.67
B22	3500	4445	185	19	0.26	0.66
B23⁺	4000	5428	253	99	0.35	0.46
C11	4500	5421	205	72	0.31	0.55
C12	2500	4562	183	73	0.2	0.88
C13	4000	4241	127	28	0.61	0.1
C21	3000	5181	169	16	0.3	0.53
C22	3000	4945	144	20	0.19	0.89
C23	3000	5845	183	5	0.21	0.72
D11	3000	4243	134	94	0.42	0.32
D12	4000	4426	173	6	0.39	0.25
D13	3500	4695	131	20	0.29	0.58
D21	4000	5144	136	24	0.88	0.02
D22⁺	4000	5677	328	5	0.58	0.06
D23⁺	4000	4819	141	17	0.63	0.09
E11	5000	8250	112	28	0.85	0.02
E12	5500	7111	120	11	0.73	0.04
E13	5500	8631	143	20	0.59	0.11
E21	4500	6688	214	26	0.49	0.2
E22	5000	6874	300	57	0.38	0.4
E23	6000	6881	191	11	0.23	0.76
F1[*]	4500	5154	111	17	0.21	0.83
F2[*]	4500	5029	72	7	0.45	0.19
F3[*]	4500	4751	123	15	0.23	0.76
F4[*]	4500	5361	257	19	0.42	0.29
F5[*]	4500	4629	130	14	0.57	0.12

f'_c = required strength (psi); AD = Anderson-Darling statistic; p = p -value; ⁺ represents the unequal subgroup size; * represents the bridge projects

Since the basic assumption prior to the analysis was that the data are normally distributed, several tests can be used to determine if data appear to follow a normal distribution. In this study, the researchers employed a graphical method and a statistical test. The graphical method is the normal probability plot and was constructed for each data set. If the data fall along a straight line, then it can be assumed that the data are at least approximately normal.

The statistical test employed was the Anderson-Darling (AD) test (Stephens, 1974). A small AD statistic indicates that the data follow a normal distribution, at least approximately. A probability can be calculated for each AD statistic and is defined as a p -value. If the p -value is less than or equal to some stated level of significance (often set at 0.05), then there is evidence that the data are not normally distributed. For example, consider Figure 57 and Table 38, which display the results of the probability plots and the statistics summary for projects A11, A13, A21, A22, and A23. Results of the AD test and the p -values as reported in Table 38 indicate that samples A11, A13, and A23 appear to follow a normal distribution while samples A21 and A22 do not. The AD statistics and p -values for all test cases are given in Table 37. Based on the p -values, it appears that projects A21, A22, B11, D21, E11, and E12 do not follow a normal distribution. Therefore, these data streams were excluded from subsequent analysis. As a result of the investigation, 23 of the original 35 test cases were monitored using the CUSUM-run and EWMA-run control charts.

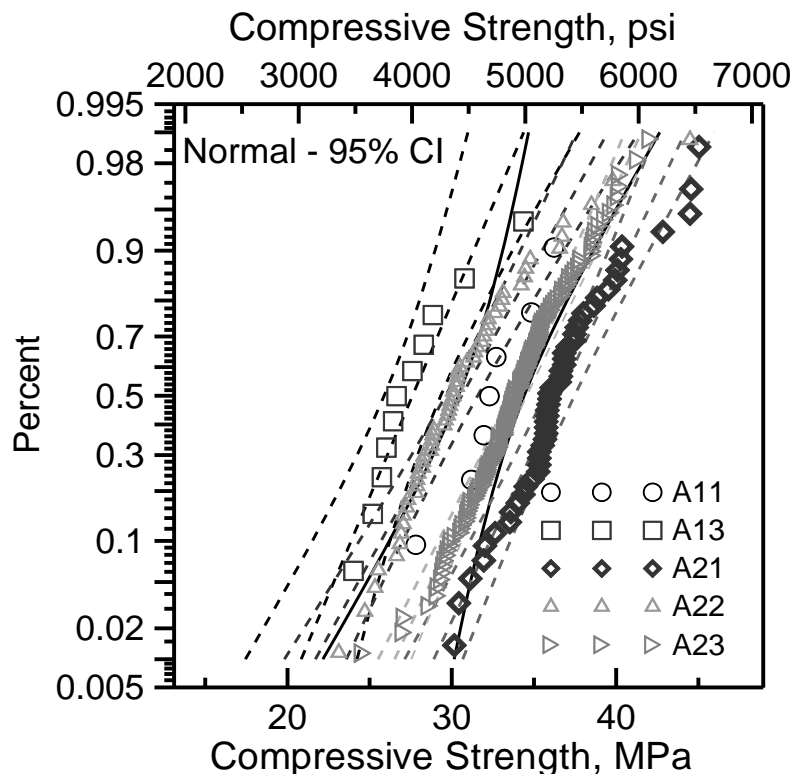


Figure 57. Probability Plot for Samples A11, A13, A21, A22, and A23 (CI = Confidence Interval).

Table 38. Statistics Summary for Samples A11, A12, A13, A21, A22, and A23.

Project	Mean, psi	Std. Dev. Psi	N	AD	p
A11	4691	132	7	0.248	0.629
A12	4047	28	2	*	*
A13	4003	110	11	0.447	0.226
A21	5308	102	50	1.045	0.009
A22	4438	109	59	0.997	0.012
A23	4931	135	146	0.698	0.067

* insufficient number of observation samples (N) to conduct the AD test statistic.

CONTROL CHART DESIGN

The researchers investigated the performance of the CUSUM chart for several combinations of h and k values ($h = 5, 4, 3, 2,$ and 1 and $k = 0, 0.125, 0.25,$ and 0.5). The CUSUM schemes with and without resetting C^+_i or C^-_i after an out-of-control signal are given and are applied to each test case. In addition, the CUSUM control chart under these scenarios is examined using two estimates of the target value, μ_0 . In the first case, the estimate used for the target value is the mean of the process data. In the second case, the specified strength, f'_c , is used as the target value, μ_0 . The CUSUM chart with the f'_c as the target value ensures consistency of the process in comparison to the specified strength, since f'_c is the constant.

As was seen in Table 36, the average concrete strength usually is higher than the f'_c . This leads to smaller values of C^+_i and larger values of C^-_i . On the CUSUM chart with f'_c target values, many out-of-control signals will occur. There also will be a noticeable trend in the upper-sided CUSUMs. On the lower CUSUM side, it will take a long time for an out-of-control signal to occur, since the test data commonly are above f'_c . To detect an out-of-control signal quickly, using the process mean as the target value is more reasonable than using f'_c . The results also indicate that resetting C^+_i or C^-_i after the limit is exceeded is a practical approach. Without resetting, the CUSUM scheme could result in problems with interpretation and identification of assignable causes, since resetting these statistics to 0 removes the historical effects of previous measurements.

The CUSUM scheme also can detect drifts that are either above or below the target. While it is acceptable for the compressive strength to be above the f'_c , it is necessary to have an early detection methodology to identify strengths below f'_c . If one or more points fall beyond the decision values, particularly the lower decision value, the control chart will produce an out-of-control signal. Subsequently, the one-sided lower CUSUM, C^-_i , as defined in Equation 32 is more appropriate for such analyses. In this procedure, as each data point is added to the sequence of the collected data (i.e., time series values of concrete strength), only values lower than the average process mean will affect the CUSUM chart.

Montgomery recommended choosing the appropriate values of H and K that result in large in-control ARLs and small out-of-control ARLs (Montgomery, 2008). In general, the selection of k is based on the shift size that the user wishes to detect. The value $k = 0.5$ ($K = 0.5 \sigma_{\bar{x}} = 0.5 \sigma / \sqrt{n}$) is used in practice. H is not chosen arbitrarily and should be chosen after k is selected. The value of h is chosen to achieve the desired ARL. Recommended h values are $h = 4$ ($H = 4 \sigma_{\bar{x}} = 4$

σ/\sqrt{n}), or $h = 5$ ($H = 5 \sigma_{\bar{x}} = 5 \sigma/\sqrt{n}$), which results in a CUSUM chart with good ARL performance so that the $1 \sigma_{\bar{x}}$ process mean shift can be detected.

To demonstrate the ARL performance of using $h = 4$ and $h = 5$ with $k = 0.5$, suppose that the process mean shifts $1 \sigma_{\bar{x}}$. Siegmund proposed a method for approximating the ARL (Siegmund, 1985):

$$ARL = \frac{\exp[-2\Delta(h+1.166)] + 2\Delta(h+1.166) - 1}{2\Delta^2} \quad (\text{Eq. 38})$$

where $\Delta = (\frac{\mu_1 - \mu_0}{\sigma_{\bar{x}}}) - k$ is used in the upper one-sided CUSUM and $\Delta = -(\frac{\mu_1 - \mu_0}{\sigma_{\bar{x}}}) - k$ marks

the lower one-sided CUSUM. For a process mean shift of $1 \sigma_{\bar{x}}$, we get $\frac{\mu_1 - \mu_0}{\sigma_{\bar{x}}} = 1$. We can

calculate the ARL for an upper one-sided chart (ARL^+), with $h = 4$ and $k = 0.5$, and $\Delta = 1 - k = 1 - 0.5 = 0.5$. The $ARL^+ = 8.343$ can be obtained using Equation 38. Using the same equation, the $ARL^+ = 10.336$ for $h = 5$ and $k = 0.5$. On the other hand, a 1σ shift downward in the process mean can be detected by the 8.343 ($h = 4$ and $k = 0.5$) and 10.336 ($h = 5$ and $k = 0.5$) samples, respectively.

For the EWMA chart, the recommended values of λ are 0.05, 0.10, and 0.20, and the usual three σ limits ($L = 3$) work reasonably well. Since smaller values of λ are used to detect smaller shifts in the process mean, the EWMA chart with $L = 3$ and $\lambda = 0.05$ and 0.1 are utilized. For a 1σ shift in the process mean, $ARL^+ = 13.51$ using $L = 3$ and $\lambda = 0.05$ and $ARL^+ = 11.38$ using $L = 3$ and $\lambda = 0.1$. The ARL^+ performance of the EWMA is similar to the CUSUM chart with $h = 5$ and $k = 0.5$.

PERFORMANCE OF THE COMBINED CONTROL CHARTS

The 23 test cases described in Table 37 were examined using the CUSUM-run and the EWMA-run control charts. Table 39 summarizes the results. A case is considered out of control if at least one point falls below the lower control limit. The CUSUM and EWMA charts perform similarly with respect to the same number of test cases (18 projects) that identified an out-of-control signal. There is only one difference between these two control methods. The EWMA chart noted an out-of-control signal on project E22, whereas project E23 signals out-of-control on the CUSUM chart. However, with respect to the acceptable minimum specified strength, E22 is considered a good mixture, because all of the strength data are greater than the required strength. Project E23 is not a good mixture since some of the strength data failed to meet the specified levels. Thus, the CUSUM chart is slightly better than the EWMA chart.

Table 39. Test Case Summaries When Monitoring the Process Mean.

Combined Control Charts		No Out-of-control Signal Found	Out-of-control Signal Found (Lower Control Limits)
EWMA	L=3 and $\lambda=0.05$	B13, A11, C21, D12, E23	A13, A23, B21, B22, C11, C12, C13, C22, D11, D13, E13, E21, E22, F1, F2, F3, F4, F5
	L=3 and $\lambda=0.1$	B13, A11, C21, D12, E23	A13, A23, B21, B22, C11, C12, C13, C22, D11, D13, E13, E21, E22, F1, F2, F3, F4, F5
CUSUM	h=4 and k=0.5	B13, B21, C21, D12, E22	A11, A13, A23, B22, C11, C12, C13, C22, D11, D13, E13, E21, E23, F1, F2, F3, F4, F5
	H=5 and k=0.5	B13, B21, C21, D12, E22	A11, A13, A23, B22, C11, C12, C13, C22, D11, D13, E13, E21, E23, F1, F2, F3, F4, F5

EXPERIMENTAL RESULTS AND FURTHER DISCUSSION

Scenario 1

In this scenario, the individual data values are equal to or greater than the lower control limit (i.e., in control), and no point plots below the f'_c . Figure 58 displays the combined charts for project C21 with $f'_c = 3,000$ psi. The lower control limit is $H^- = -4\sigma_{\bar{x}} = -4.92$ and $k = 0.5$ for the CUSUM chart. For the EWMA chart, the lower control limit is based on $L = 3$ and $\lambda = 0.05$. This case represents an in-control (stable) and capable process. Scenario 1 represents a good process since the process is stable under the acceptable level of concrete strength (greater than the f'_c). It therefore does not require any changes in the process.

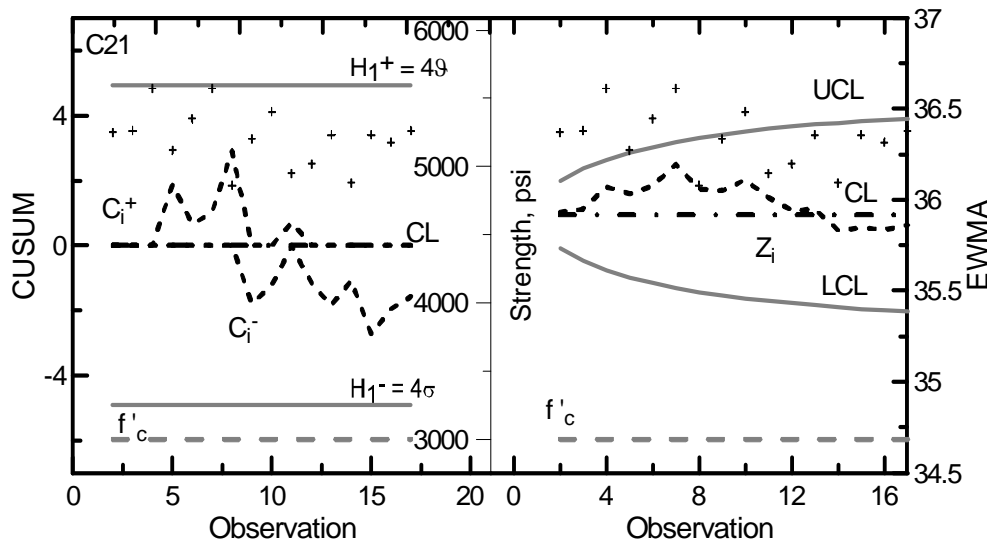


Figure 58. Plot of the Combined Control Charts for Project C21 (Subgroup Size=2) When $f'_c = 3,000$ psi (N =16).

Scenario 2

In Scenario 2, the process is in control and there is a point that falls below f'_c . Figure 59 displays the combined charts for project D12 with $f'_c = 4,000$ psi. There is no point that plots below the limit H ($H = -4\sigma_{\bar{x}} = -5.25$ and $k = 0.5$) for the CUSUM chart or the LCL ($L = 3$ and $\lambda = 0.05$) on the EWMA chart. However, observation 3, with a strength of 3,980 psi, falls below f'_c . In this situation, the process is said to be in control (stable) but not capable. Scenario 2 represents a poor process since the process is stable under an unacceptable level of concrete strength (lower than the f'_c). It is then necessary to inspect the concrete process and find the possible root cause of the problem in an effort to improve the concrete strength. This may require a new formulation of the cement mixture to increase the overall strength while minimizing the variation in the strength.

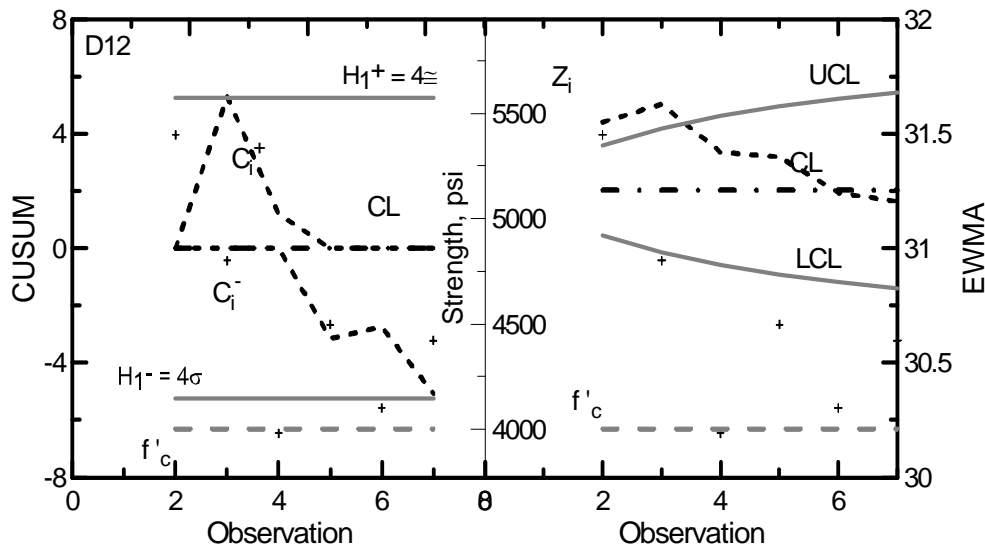


Figure 59. Plot of the Combined Chart for Project D12 (Subgroup Size=2) When $f'_c = 4,000$ psi ($N=6$).

Scenario 3

Scenario 3 consists of individual data values that may be less than the lower control limit (out-of-control process), but there are no points lower than the f'_c . Figure 60 demonstrates the combined charts for project D13 with $f'_c = 3,500$ psi. In this project, there were five observations that fall below the H ($H = -4\sigma_{\bar{x}} = -2.55$) for the CUSUM chart and eight observations that fall below the LCL ($L = 3$ and $\lambda = 0.05$) on the EWMA chart. In this case, the process is out of control (not stable) but capable. This is an acceptable situation since the process maintains an acceptable level of concrete strength (greater than f'_c). However, because the process signals that it is out of statistical control, it is important to determine if this is a real out-of-control situation or a false alarm. If the process truly is out of control, the assignable cause should be identified and corrective action taken to bring the process back into statistical control. The importance of identification and correction in this scenario cannot be overstated. Even though the strength did not plot below the acceptable minimum for the current samples, an out-of-control process left unchecked will continue to operate out of control and eventually will result in concrete strengths that no longer meet the acceptable minimum.

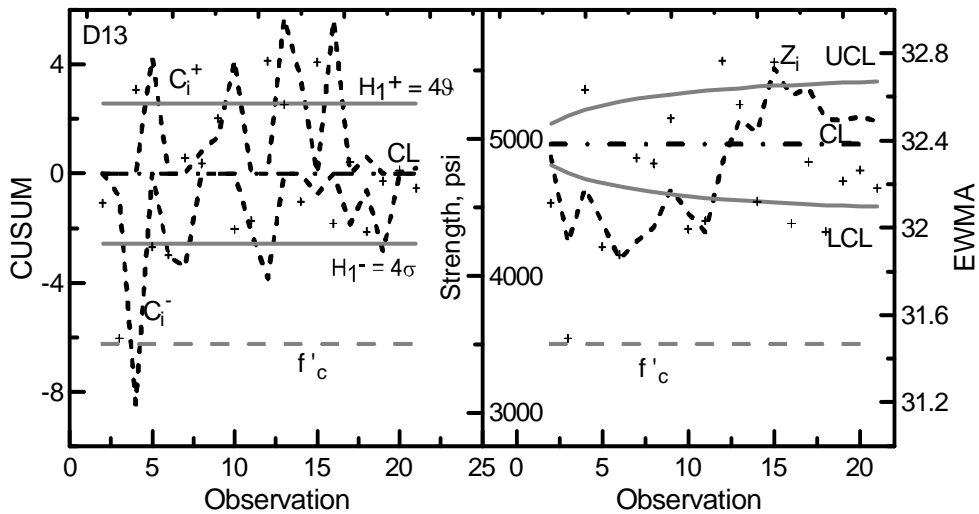


Figure 60. Plot of the Combined Chart for Project D13 (Subgroup Size=2) When $f'_c = 3,500$ psi (N=20).

Scenario 4

In Scenario 4, the process is out of control and there is at least one point below f'_c . Figure 61 illustrates the combined charts for project F4 with $f'_c = 4,500$ psi. Four observations fall below H ($H = -4\sigma_{\bar{x}} = -5.01$) on the CUSUM chart, and nine points fall below the LCL ($L = 3$ and $\lambda = 0.05$) on the EWMA chart. In addition, there are two points below f'_c . In this situation, the process is unstable (out of control) and incapable, representing a poor process. It is important to investigate the process and reduce variation to bring the process back into statistical control and make it capable.

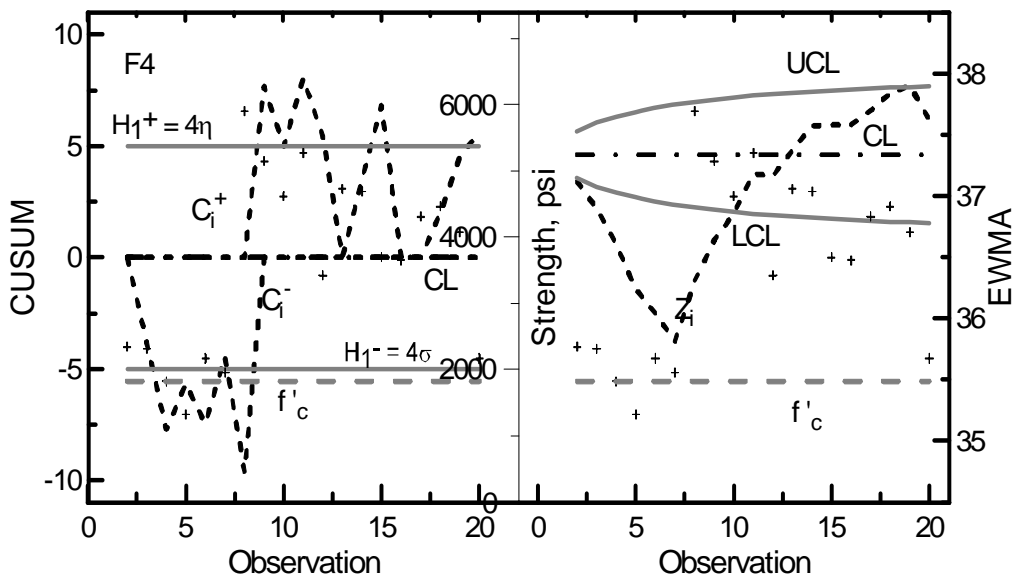


Figure 61. Plot of the Combined Chart for Project F4 (Subgroup Size=2) When $f'_c = 4,500$ psi (N=19).

FURTHER COMPARISONS OF THE CUSUM-RUN AND EWMA-RUN CHARTS

Table 40 summarizes the performance of the CUSUM-run and EWMA-run charts for the detection of the out-of-control signals. The criterion of comparison between the two charts was the accuracy of signaling an out-of-control process when there are data below the f'_c . The CUSUM scheme appeared to be robust over the range of h from 4 to 5. The suggested limits for the CUSUM are $h = 4$ and $k = 0.05$, since smaller values of h resulted in considerably smaller out-of-control ARL values. The EWMA chart was sensitive to changes in the weight, λ , since for all values of λ the EWMA chart was able to identify the same processes as out of control in each of the four scenarios. Based on the small out-of-control ARL values, the EWMA chart with $L = 3$ and $\lambda=0.1$ is recommended to detect small shifts (1.5σ or less) in comparison to $L=3$ and $\lambda=0.05$.

Of 23 cases, 14 cases (Scenarios 1 and 4) were identified correctly as out of control by the combined CUSUM-run charts. The EWMA-run chart identified only 12 cases. For Scenario 2, the CUSUM chart identified only one project (D12) as out of control, and the EWMA chart identified two projects (D12 and E23) as out of control. To avoid this pitfall, the values of h (for CUSUM) or L (for EWMA) in the combined chart should be reduced. Tightening the limits on either the CUSUM or EWMA charts generally will increase the sensitivity and the false alarm signal. For the 23 cases consisting of more than 1,000 data points, it was observed that there are 23 points below the f'_c .

Table 40. Test Case Summary Classification.

Combined Control Chart	EWMA		CUSUM	
	$L = 3$ and $\lambda = 0.05$	$L = 3$ and $\lambda = 0.1$	$h = 4$ and $k = 0.5$	$h = 5$ and $k = 0.5$
$x_i > f'_c$ In-control Process	B13, A11, and C21	B13, A11, and C21	B13, B21, C21, and E22	B13, B21, C21, and E22
$x_i < f'_c$ In-control Process	D12 and E23	D12 and E23	D12	D12
$x_i > f'_c$ Out-of-control Process	A13, A23, B21, C12, C22, D13, E13, E21, and E22	A13, A23, B21, C12, C22, D13, E13, E21, and E22	A11, A13, A23, C12, C22, D13, E13, and E21	A11, A13, A23, C12, C22, D13, E13, and E21
$x_i < f'_c$ Out-of-control Process	B22, C11, C13, D11, F1, F2, F3, F4, and F5	B22, C11, C13, D11, F1, F2, F3, F4, and F5	B22, C11, C13, D11, E23, F1, F2, F3, F4, and F5	B22, C11, C13, D11, E23, F1, F2, F3, F4, and F5
Number of Points below the Lower Limit	212	209	129	100

x_i = individual data value

The CUSUM-run chart also detects out-of-control observations more effectively than the EWMA-run chart for an in-control process. The CUSUM-run scheme detects 129 out-of-control points, whereas the EWMA-run chart detects 209 out-of-control points. It clearly shows that there are too many out-of-control signals found by both combined charts. However, some of these signals may be false alarms that may lead to misinterpreting the results. The ARL performance analyses in Table 35 provide useful information in determining whether the alarm is false or real.

The use of individual CUSUM charts may aid in determining the overall stability of a process, thus helping improve production processes by identifying an assignable cause. The scheme also can monitor the quality of the compressive strength. However, the CUSUM chart alone might not be enough to explain overall process performance. As seen in Scenario 2, applying the individual CUSUM chart did not detect an undesirable property (i.e., capability). On the other hand, the combined chart for project D12, for example, provides no out-of-control signal based on the CUSUM side. By combining a run chart to the existing CUSUM chart obviously identifies the one sample that falls beyond f'_c . The use of the run chart also assists in monitoring the process variation over the given period of time and examines process capability. The concrete process is considered capable as long as the strength result is greater than f'_c . The run chart can be used to represent the consumer's decision. If the process maintains high capability, it will achieve high performance. A high-performance process can result in fewer defects and lower production costs.

The CUSUM-run chart is a good choice for monitoring small shifts in the process mean. As has been shown, the CUSUM-run chart simultaneously monitors both consistency and capability. The CUSUM-run chart also aids in determining whether the process is operating under normal conditions if the CUSUM side signals out-of-control. For example, the combined chart for project D13 clearly has detected many out-of-control signals, so it is easy to understand that the process is not operating under normal conditions. The run chart shows that no point falls below f'_c . It is possible that the process mean is moving downward, even if it still results in an acceptable level of concrete strength (greater than the f'_c). The decision-maker should consider the ARL performance in order to make a decision after the CUSUM side signals out-of-control. If the alarm is real, the process can be examined and the assignable cause removed as soon as possible. Thus, the CUSUM scheme can be used with the run chart to increase the accuracy of small shift detection.

PAY FACTOR CRITERIA

It is necessary to detect shifts in the average compressive strength soon after a shift has occurred. This allows for early corrective actions to circumvent broader and more severe negative consequences. For example, eliminating the assignable cause and bringing the process back to normal operating conditions can prevent the production of more unqualified concrete. If the producer does not detect the unqualified concrete, then the consumer cannot use it, and the producer will be charged a penalty. The amount of the penalty depends on the variation between the actual strength and f'_c . There are several approaches to calculate the pay factor, including the FHWA guidelines, the currently enforced ADOT guidelines, the recently proposed ADOT guidelines, and the California Department of Transportation (Caltrans) guidelines (U.S. DOT, 1989). A previous study conducted by the authors of this report addressed the importance of pay factor calculations and cost associated with the variability of compressive strength test data (Laungrungrong, Mobasher & Montgomery, 2008).

CONCLUSIONS

The CUSUM-run and EWMA-run charts that were applied to the historical data in this study indicate that there often is a much higher level of compressive strength than the minimum specified strength. In most cases, the difference between the two amounts could be considered excessive and unnecessary given the amount of variability in the strength at 28 days. The amount of cement needed to obtain the strength levels observed in the test cases would result from a significant (and itself excessive) use of energy in the cement production process. When the decision-maker has a clear understanding of the differences between a natural variability for a process and an uncommon variability due to some assignable cause, it can reduce the over-design of the concrete mixture significantly.

The combined control charts described in this report can aid in identifying when a process is producing concrete with such high strength levels that the amount of cement being used could be reduced while maintaining at least the minimum specified strength. If the producer had used control charts on some of the processes that resulted in the test cases used in this study, unusually high or low strength levels may have been identified early enough in the process that corrective action might have been taken, resulting in fewer rejected lots and less excessive amounts of cement used. For example, consider sample C21 as displayed in Figure 62 and described in Table 36. Based on the summary statistics, the average compressive strength (5,207 psi) is almost 9 standard deviations higher than the minimum specified level (3,000 psi). In this case, the amount of cement in the mixture and the energy used could have been reduced while still meeting the minimum specified level.

The QC and monitoring approaches presented in this chapter can play a significant role in attaining these goals. In fact, if QC methods such as SPC, monitoring (such as the CUSUM and EWMA), and the design of experiments (DOE) are not implemented and used more regularly, it will be much more difficult to attain (and maintain) the stated goal of reduction in CO₂ emissions. The natural variability in the production, delivery, and construction systems must be well understood before efforts and regulations for sustainability will be effective on a consistent basis. Identifying natural (common) variability and assignable cause variability (and being able to separate the two) is imperative and can be done only by using statistically based methods such as SPC and DOE. Thus, there is a need for further study and investigation on the type of control charts and implementation to achieve the desired goals.

The researchers propose the combination of two control charts to evaluate the compressive strength of concrete. Several scenarios and test cases were examined to illustrate the proposed methodology. Two different ready-mix plants from five different concrete suppliers were selected for this study. For each plant, three different mix specifications were used, and the design histories of concrete supplied from these plants were studied. This report also presents and discusses the interpretation of out-of-control signals and methods to remedy each problem. The guidelines will assist the consumer and producer in understanding the overall behavior of data sampling.

REFERENCES

- ACI Committee 318. 2005. "Building Code Requirements for Structural Concrete." *ACI Manual of Concrete Practice*. Detroit: American Concrete Institute.
- Aïtcin, P. C. 1998. *High-performance Concrete*. London: Taylor & Francis.
- American Coal Ash Association. 2003. *Fly Ash Facts for Highway Engineers*. Publication FHWA-IF-03-019. Washington, D. C.: Federal Highway Administration.
- American Concrete Institute. 2001. *Guide to Durable Concrete*. Publication ACI 201.2R-01. Farmington Hills, Michigan: American Concrete Institute.
- American Concrete Institute. 2005. *ACI Manual of Concrete Practice*. Farmington Hills, Michigan: ACI.
- American Concrete Institute. 2008. *Building Code Requirements for Structural Concrete and Commentary*. ACI 318-08. Farmington Hills, Michigan: American Concrete Institute.
- American Concrete Institute Committee 214. 2002. *Evaluation of Strength Test Results of Concrete*. Publication ACI 214R-02. Farmington Hills, Michigan: American Concrete Institute.
- American Concrete Institute Committee 544. 1996. *State-of-the-Art Report on Fiber Reinforced Concrete*. Publication ACI 544.1R-96. Farmington Hills, Michigan: American Concrete Institute.
- Ariño, A. M., and B. Mobasher. 1999. "Effect of Copper Slag on the Strength and Toughness of Cementitious Mixtures." *ACI Materials Journal* 96(1): 68-73.
- ASTM International. 1999a. "Standard Tests Method for Obtaining Average Residual Strength of Fiber-Reinforced Concrete." ASTM C1399. Philadelphia: ASTM.
- ASTM International. 1999b. "Test Method for Flexural Performance of Fiber-Reinforced Concrete (Using Beam With Third-Point Loading)." ASTM C1609: Philadelphia: ASTM.
- ASTM International. 2008. *Standard Test Method for Determining the Potential Alkali-Silica Reactivity of Combinations of Cementitious Materials and Aggregate (Accelerated Mortar-Bar Method)*. ASTM C1567. Philadelphia: ASTM.
- Barros, J. A. O., V. M. C. F. Cunha, A.F. Ribero, and J.A.B. Antunes. 2005. "Post-cracking Behaviour of Steel Fibre Reinforced Concrete." *Materials and Structures* 38(1): 47-56.
- Basheer, P. A. M. 1993. "A Brief Review of Methods for Measuring the Permeation Properties of Concrete In Situ." *Proceedings of the Institution of Civil Engineers, Structures and Buildings*. 99(1): 74-83.

- Bentur, A., S. Igarashi, and K. Kovler. 2001. "Prevention of Autogenous Shrinkage in High Strength Concrete by Internal Curing Using Wet Lightweight Aggregates." *Cement and Concrete Research* 31(11): 1587-1591.
- Bentur, A., and S. Mindess. 1990. *Fiber Reinforced Cementitious Composites*. London: Elsevier.
- Bentz, D. P. 2002. *Influence of Curing Conditions on Water Loss and Hydration in Cement Pastes with and without Fly Ash Substitution*. National Institute of Standards and Technology Internal Report 6886. Gaithersburg, Maryland: NIST.
- Bentz, D. P. 2007. "Internal Curing of High-Performance Blended Cement Mortars." *ACI Materials Journal* 104(4): 408-414.
- Bentz, D. P., and E. J. Garboczi, E. J. 1991. "Simulation Studies of the Effects of Mineral Admixtures on the Cement Paste-Aggregate Interfacial Zone." *ACI Materials Journal* 88(5): 518-529.
- Bentz, D.P., Geiker, M.R., Hansen, K.K. 2001. "Shrinkage-reducing Admixtures and Early-age Desiccation in Cement Pastes and Mortars." *Cement and Concrete Research* 31(7): 1075-1085..
- Bentz, D. P., and W. J. Weiss. 2008. "REACT: Reducing Early-age Cracking Today." *Concrete Plant International* 3: 56-62.
- Brown, B. V. 1984. "Monitoring Concrete by the Cusum System." Midrand, South Africa: Cement and Concrete Institute.
- CEMBUREAU (the European Cement Association), 2013. *The Cement Sector: A Strategic Contributor to Europe's Future*. Brussels, Belgium: Boston Consulting Group, report to CEMBUREAU.
- Chen, K. S., W. P. Sung, and M. H. Shih. 2005. "Reliable Evaluation Method of Quality Control for Compressive Strength of Concrete." *Journal of Zhejiang University Science A*(8): 836-843.
- Chuang T. J., and Y. W. Mai. 1989. "Flexural Behavior of Strain-softening Solids." *International Journal of Solids and Structures*. 25(12): 1427-1443.
- Collins, F., and J. G. Sanjayan. 1999. "Strength and Shrinkage Properties of Alkali-Activated Slag Concrete Containing Porous Coarse Aggregate." *Cement and Concrete Research* 29(4): 607-610.
- The Concrete Society. 1988. *Permeability Testing of Site Concrete – A Review of Methods and Experience*. Technical Report No. 31. London, England: The Concrete Society.
- Crowder, S. V. 1987. "A Simple Method for Studying Run-length Distributions of Exponentially Weighted Moving Average Charts." *Technometrics* 29(4): 401-407.

Cusson, D., and T. Hoogeveen. 2008. "Internal Curing of High-performance Concrete with Pre-soaked Fine Lightweight Aggregate for Prevention of Autogenous Shrinkage Cracking." *Cement and Concrete Research* 38(6): 757-765.

Damtoft, J. S., J. Lukasik, D. Herfort, D. Sorrentino, and E. M. Gartner, E. M. 2008. "Sustainable Development and Climate Change Initiatives." *Cement and Concrete Research* 38: 115-127.

Day, K. W. 2006. *Concrete Mix Design, Quality Control and Specification*. New York, New York: Spon Press.

Delatte, N., E. Mack, and J. Cleary. 2007. *Evaluation of High Absorptive Materials to Improve Internal Curing of Low Permeability Concrete*. Publication FHWA/OH-2007/06. Cleveland: Ohio Department of Transportation.

Dhir, R. K., P. C. Hewlett, and T. D. Dyer. 1996, "Influence of Microstructure on the Physical Properties of Self-Curing Concrete." *ACI Materials Journal* 93(5): 465-471.

Dhir, R. K., P. C. Hewlett, J. S. Lota, and T. D. Dyer. 1994. "An Investigation into the Feasibility of Formulating 'Self-Cure' Concrete." *Materials and Structures* 27(10): 606-615.

Feigenbaum, A. V. 1991. *Total Quality Control*. New York, New York: McGraw- Hill.

Franzén, T. 1992. "Shotcrete for Underground Support - a State of the art report with focus on steel fibre reinforcement. In *Rock Support in Mining and Underground Construction* (proceedings of the Interational Symposium on Rock Support), eds. P. K. Kaiser and D. R. McCreath, 91-104. Rotterdam: Balkema.

George, M. L. 2002. *Lean Six Sigma: Combining Six Sigma Quality with Lean Speed*. New York, New York: McGraw-Hill.

Gopalaratnam, V.S. 1995. "On the Characterization of Flexural Toughness in Fiber Reinforced Concretes." *Cement and Concrete Composites* 17(3): 239-254.

Gopalaratnam, V. S., and R. Gettu. 1995. "On the Characterization of Flexural Toughness in Fiber Reinforced Concretes." *Cement and Concrete Composites* 17(3): 239-254.

Gopalaratnam, V. S., S. P. Shah, G. B. Batson, M. E. Criswell, V. Ramakrishnan, and M. Wecharatana. 1991. "Fracture Toughness of Fiber Reinforced Concrete." *ACI Materials Journal* 88(4): 339-353.

Hammer, T. A. 1992. "High Strength LWA Concrete with Silica Fume – Effect of Water Content in the LWA on Mechanical Properties." Supplementary Papers, 4th CANMET/ACI International Conference on Fly Ash, Silica Fume, Slag and Natural Pozzolans in Concrete. Istanbul, Turkey: 314-330.

- Hammer, T. A., O. Bjontegaard, and E. J. Sellevold. 2004. "Internal Curing – Role of Absorbed Water in Aggregates." In *High Performance Structural Lightweight Concrete*, ed. J. P. Ries and T. A. Holm. Special Publication 218. Farmington Hills, Michigan: ACI., pp. 131-142.
- Hawkins, D. M. 1992. "A Fast Accurate Approximation for Average Run Lengths of CUSUM Control Charts." *Journal of Quality Technology* 24(1): 37-43.
- Hawkins, D. M. 1993. "Cumulative Sum Control Charting: An Underutilized SPC Tool." *Quality Engineering* 5(3): 463-477.
- Hawkins, D. M., and D. H. Olwell. 1998. *Cumulative Sum Charts and Charting for Quality Improvement*. New York, New York: Springer.
- Henkensiefken, R., P. Briatka, D. P. Bentz, T. Nantung, and J. Weiss. 2010. "Plastic Shrinkage Cracking in Internally Cured Mixtures." *Concrete International* 32(2): 49-54.
- Jensen, O. M. 2005. "Autogenous Phenomena in Cement-based Materials." PhD dissertation. Copenhagen, Denmark: Aalborg University.
- Jensen, O. M., and P. F. Hansen. 2001. "Water-entrained Cement-based Materials I. Principles and Theoretical Background." *Cement and Concrete Research* 31(4): 647-654.
- Kalousek, G. L., L. C. Porter, and E. J. Benton. 1972. "Concrete for Long-Term Service in Sulfate Environment." *Cement and Concrete Research* 2: 79-89.
- Kitsutaka, Y., M. Tamura, A. Iihoshi, and K. Goto. 2002. "Early-Age Shrinkage Properties of High-Strength Lightweight Aerated Concrete." *Proceedings, International Workshop on Control of Cracking in Early-Age Concrete*. H. Mihashi and F. Wittman (eds.). Sendai, Japan, August 23-24: 213-218.
- Kohno, K., T. Okamoto, Y. Isikawa, T. Sibata, and H. Mori. 1999. "Effects of Artificial Lightweight Aggregate on Autogenous Shrinkage of Concrete." *Cement and Concrete Research* 29(4): 611-614.
- Kovler, K., and O. M. Jensen (eds.). 2007. *Internal Curing of Concrete—State-of-the-art Report of RILEM Technical Committee 196-ICC*. Publication rep041. Bagneux, France: RILEM.
- Laungrungrong, B., B. Mobasher, and D. Montgomery. 2008. *Development of Rational Pay Factors Based on Concrete Compressive Strength Data*. FHWA-AZ-08-608. Phoenix: Arizona Department of Transportation.
- Laungrungrong, B., B. Mobasher, D. C. Montgomery, and C. M. Borrer. 2010. "Hybrid Control Charts for Active Control and Monitoring of Concrete Strength." *ASCE Journal of Materials Engineering* 22(1): 77-87.
- Leaming, G. F. 1998. *The Economic Impact of the Arizona Copper Industry-1997*. Marana, Arizona: Western Economic Analysis Center.

- Leshchinsky, A. M. 1991. "Combined Methods of Determined Control Measures of Concrete Quality." *Materials and Structures* 24(3): 177-184.
- Lura, P., and K. van Breugel 2000. "Moisture Exchange as a Basic Phenomenon to Understand Volume Changes of Lightweight Aggregate Concrete at Early Age." *Proceedings, International RILEM Workshop on Shrinkage of Concrete*. V. Baroghel-Bouny and P. C. Aïtcin (eds.). Paris, France, October 16-17: 533-546.
- Lura, P., K. van Breugel, and I. Maruyama. 2002. "Autogenous and Drying Shrinkage of High-Strength Lightweight Aggregate Concrete at Early Ages – The Effect of Specimen Size." *Proceedings, International RILEM Conference on Early Age Cracking in Cementitious Systems*. K. Kovler and A. Bentur (eds.). Haifa, Israel, March 12-14: 335-342.
- Malhotra, V. M., and P. K. Mehta. 2005. *High-performance, High-volume Fly Ash Concrete: Materials, Mixture Proportioning, Properties, Construction Practice, and Case Histories*. 2nd Edition. Ottawa, Canada: Supplementary Cementing Materials for Sustainable Development, Inc.
- Mandel, J. 1969. "The Partitioning of Interaction in Analysis of Variance." *Journal of Research of the National Bureau of Standards* 73B(4): 309-327.
- Maricopa Association of Governments Standards. 2012. MAG Standards for Concrete Specifications. <http://www.azmag.gov/Committees/Committee.asp?CMSID=1055>.
- Mechtcherine, V., L. Dudziak, and J. Schulze. 2006. "Internal Curing by Super Absorbent Polymers (SAP) – Effects on Material Properties of Self-compacting Fibre-reinforced High Performance Concrete." *International RILEM Conference on Volume Changes of Hardening Concrete: Testing and Mitigation*, ed. O. M. Jensen, P. Lura, and K. Kovler, 87-96. Bagnex France: RILEM.
- Mehta, P. K. 2004. "High-Performance, High-Volume Fly Ash Concrete for Sustainable Development." In *Proceedings of the International Workshop on Sustainable Development & Concrete Technology, Beijing, China, May 20-21*, ed. Kejin Wang, 3-14.
- Mobasher, B. 2011. *Mechanics of Fiber and Textile Reinforced Cement Composites*. Boca Raton, Florida: CRC Press 473 pp
- Mobasher, B., and R. Devaguptapu. 1993. "Effect of Copper Slag on the Hydration Characteristics, Strength, and Fracture Properties of Concrete." Technical Report 93-1. Tempe: Arizona State University.
- Mobasher, B. and C. Y. Li. 1996. "Mechanical Properties of Hybrid Cement Based Composites." *ACI Materials Journal* 93(3): 284-293.
- Monteiro, P. J. K., and K. E. Kurtis. 2003. "Time to Failure for Concrete Exposed to Severe Sulfate Attack." *Cement and Concrete Research* 33: 987-993.

- Montgomery, D. C. 2008. *Introduction to Statistical Quality Control*. New York, New York: John Wiley & Sons.
- Nemegeer-Harelbeke, D. 1998. *Design Guidelines for Dramix Steel Fibre Reinforced Concrete*. Bekaert: Brussels.
- Nemkumar, B., and D. Ashish. 1999. "Measurement of Flexural Toughness of Fiber-Reinforced Concrete Using a Novel Technique - Part 1: Assessment and Calibration." *ACI Materials Journal* 96(6): 651-656.
- Nemkumar, B., and D. Ashish. 2000. "Measurement of Flexural Toughness of Fiber-Reinforced Concrete Using a Novel Technique - Part 2: Performance of Various Composites." *ACI Materials Journal* 97(1): 3-11.
- Nikam, V. S., D. D. Rane, and S. S. Deshmukh. 2005. "High Volume Fly Ash Concrete for Eco-Durable Pavement." *IABSE Reports* 89: 415-420.
- Page, E. S. 1954. "Continuous Inspection Schemes." *Biometrika* 41(1-2): 100-115.
- Parrott, L. J. 1995. "Influence of Cement Type and Curing on the Drying and Air Permeability of Cover Concrete," *Magazine of Concrete Research* 47(171): 103-111.
- Philleo, R. 1991. "Concrete Science and Reality." In *Materials Science of Concrete II*, J. P. Skalny and S. Mindess (eds.). Westerville, Ohio: American Ceramic Society, pp. 1-8
- Poon, C. S., L. Lam, S. C. Kou, Y. L. Wong, and R. Wong. 2001. "Rate of Pozzolanic Reaction of Metakaolin in High-Performance Cement Pastes." *Cement and Concrete Research* 31: 1301-1306.
- Portland Cement Association. 2009. *Report on Sustainable Manufacturing*. <http://www.cement.org/smreport09/>.
- RILEM Technical Committee 162-TDF. 2003. " σ - ϵ Design Method – Final Recommendation." *Materials and Structures* 36(8):560-567.
- Roberts, S. W. 1959. "Control Chart Tests based on Geometric Moving Averages." *Technometrics* 1(3): 239-250.
- Roy, D. M. 1999. "Alkali-Activated Cements: Opportunities and Challenges." *Cement and Concrete Research* 29: 249-254.
- Sabir, B. B., S. Wild, and J. M. Khatib. 1996. "On the Workability and Strength Development of Metakaolin Concrete." In *Concrete for Environmental Enhancement and Protection*, ed. R. K. Dhir and T. D. Dyer, 651-662. London: E&FN Spon.
- Schwesinger, P., and G. Sickert. 2002. "Reducing Shrinkage in HPC by Internal Curing by Using Pre-Soaked LWA." *Proceedings, International Workshop on Control of Cracking in Early-Age Concrete*. H. Mihashi and F. Wittman (eds.). Sendai, Japan, August 23-24: 333-338.

- Shattaf, N. R., A. M. Alshamsi, and R. N. Swamy. 2001. "Curing/Environment Effect on Pore Structure of Blended Cement Concrete." *Journal of Materials in Civil Engineering* 13(5): 380-388.
- Shekarchi, M., A. Bonakdar, M. Bakhshi, A. Mirdamadi, and B. Mobasher. 2009. "Transport Properties in Metakaolin Blended Concrete." *Construction and Building Materials* 24(11): 2217-2223.
- Siegmund, D. 1985. *Sequential Analysis: Tests and Confidence Intervals*. New York, New York: Springer-Verlag.
- Soranakom, C., and B. Mobasher. 2007a. "Closed-form Moment-curvature Expressions for Homogenized Fiber Reinforced Concrete." *ACI Materials Journal* 104(4): 351-359.
- Soranakom, C., and B. Mobasher. 2007b. "Closed Form Solutions for Flexural Response of Fiber Reinforced Concrete Beams." *ASCE Journal of Engineering Mechanics* 133(8): 933-941.
- Soranakom, C., and B. Mobasher. 2008. "Correlation of Tensile and Flexural Responses of Strain Softening and Strain Hardening Cement Composites." *Cement and Concrete Composites* 30(6): 465-477.
- Soranakom, C., and B. Mobasher. 2010. "Flexural Analysis and Design of Strain Softening Fiber-Reinforced Concrete." In *Antoine E. Naaman Symposium- Four Decades of Progress in Prestressed Concrete, FRC, and Thin Laminate Composites*, ed. Gustavo J. Parra-Montesinos & Perumalsamy Balaguru, 173-187. Special Publication SP-272. Farmington Hills, Michigan: American Concrete Institute.
- Soranakom, C., M. Bakhshi, and B. Mobasher. 2008. "Role of Alkali Resistant Glass Fibers in Suppression of Restrained Shrinkage Cracking of Concrete Materials." In *Proceedings of the 15th International Glass Fibre Reinforced Concrete Association Congress*, Prague, Czech Republic, April 20-23.
- Soroka, I. 1968. "An Application of Statistical Procedures to Quality Control of Concrete." *Materials and Structures* 1(5): 437-441.
- Sprinkel, M. M. 2004. *Performance Specification for High Performance Concrete Overlays on Bridges*. Publication VTRC 05-R2. Charlottesville: Virginia Transportation Research Council. P. 26
- Stanish, K. D., Hooton, R. D., & Thomas, M. D. A. (2000). Testing the chloride penetration resistance of concrete: a literature review. FHWA Contract DTFH61-97-R-00022 "Prediction of Chloride Penetration in Concrete". Department of Civil Engineering, University of Toronto.
- Stephens, M. A. (1974). EDF Statistics for Goodness of Fit and Some Comparisons, *Journal of the American Statistical Association*, 69, pp. 730-737.
- Sykora, V. 1995. "Amendment of Appendix X2 in ASTM C 917 Evaluation of Cement Uniformity from a Single Source." *Cement, Concrete and Aggregates* 17(2): 190-192.

- Takada, K., K. van Breugel, E. A. B. Koenders, and N. Kaptijn. 1998. "Experimental Evaluation of Autogenous Shrinkage of Lightweight Aggregate Concrete." *Proceedings, International Workshop on Autogenous Shrinkage of Concrete*. Hiroshima, Japan, June 13-14: 221-230.
- Thomas, M. D. A., B. Fournier, and K. J. Folliard. 2008. *Report on Determining the Reactivity of Concrete Aggregates and Selecting Appropriate Measures for Preventing Deleterious Expansion in New Concrete Construction*. Publication FHWA-HIF-09-001. Washington, D. C.: Federal Highway Administration.
- Tixier, R., R. Devaguptapu, and B. Mobasher. 1997. "The Effect of Copper Slag on the Hydration and Mechanical Properties of Blended Cementitious Mixtures." *Cement and Concrete Research* 27(10): 1569-1580.
- Triandafilou, L. N., C. S. Napier Jr., and R. F. Maruri. 2007. "National High Performance Concrete Follow-up Survey Results." http://www.virginiadot.org/business/resources/Materials/Virginia_Concrete_Presentations/1B-Triandafilou-HPC_Survey_Results.pdf as of 5/4/2013
- Tuthill, L. H. 1936. "Resistance of Cement to the Corrosive Action of Sodium Sulfate Solutions." *Journal Proceedings* 33(11): 83-103.
- U.S. Department of Transportation, Federal Highway Administration and Federal Lands Highway. 1989. *Standard Specifications for Construction of Roads and Bridges on Federal Highway Projects*. FHWA Technical Advisory T5080.12. Washington, D. C.: FHWA. <http://flh.fhwa.dot.gov/resources/pse/specs/> as of 1/20/2013
- Van Breugel, K., H. Outwerk, and J. De Vries. 2000. "Effect of Mixture Composition and Size Effect on Shrinkage of High Strength Concrete." *Proceedings, International RILEM Workshop on Shrinkage of Concrete*. V. Baroghel-Bouny and P. C. Aïtcin (eds.). Paris, France, October 16-17: 161-177.
- Van Dam, T. J., K. R. Peterson, L. L. Sutter, A. Panguluri, J. Sytsma, N. Buch, R. Kowli, and P. Desraj. 2005. *Guidelines for Early-Opening-to-Traffic Portland Cement Concrete for Pavement Rehabilitation*. National Cooperative Highway Research Program (NCHRP) Report 540. Washington, D. C.: Transportation Research Board.
- Vandewalle, M. 1993. *Dramix: Tunnelling the World*. 3rd edition. Bekaert: Zwevegem, Belgium.
- Vanikar, S. N., and L. N. Triandafilou. 2005. *Implementation of High-Performance Concrete Bridge Technology in the USA*. Special Publication 228. Farmington Hills, Michigan: American Concrete Institute.
- Vaysburd, A. M. 1996. "Durability of Lightweight Concrete Bridges in Severe Environments." *Concrete International* 18(7): 33-38.
- Weber, S., and H. Reinhardt. 1995. "A Blend of Aggregates to Support Curing of Concrete." *Proceedings, International Symposium on Structural Lightweight Aggregate Concrete*. T. A. Hammer and F. Fluje (eds.). Sandefjord, Norway: 662-671.

- Weber, S., and H. Reinhardt. 1997. "A New Generation of High Performance Concrete: Concrete with Autogenous Curing." *Advanced Cement Based Materials* 6(2): 59-68.
- Wee, T. H., H. R. Lu, and S. Swaddiwudhipong. 2000. "Tensile Strain Capacity of Concrete under Various States of Stress." *Magazine of Concrete Research* 52(3): 185-193.
- Woodall, W. H. 1985. "The Statistical Design of Quality Control Charts." *The Statistician* 34(2): 155-160.
- Woodall, W. H., and B. M. Adams. 1993. "The Statistical Design of CUSUM Charts." *Quality Engineering* 5(4): 559-570.
- Yunovich, M., N.G. Thompson, and Y. P. Virmani. 2004. "Corrosion of Highway Bridges: Economic Impact and Life-Cycle Cost Analysis." 2004 Concrete Bridge Conference: Building a New Generation of Bridges, May 17-18, Charlotte, North Carolina.
- Zhutovsky, S., K. Kovler, and A. Bentur. 2002. "Efficiency of Lightweight Aggregates for Internal Curing of High Strength Concrete to Eliminate Autogenous Shrinkage." *Materials and Structures* 35(2): 97-101.

